#1

Figures for SAND 94-1174, "Assessment of the CONTAIN Direct Containment Heating (DCH) Model: Analyses of DCH Integral Experiments," Sandia National Laboratories, DRAFT dated November 10, 1996.

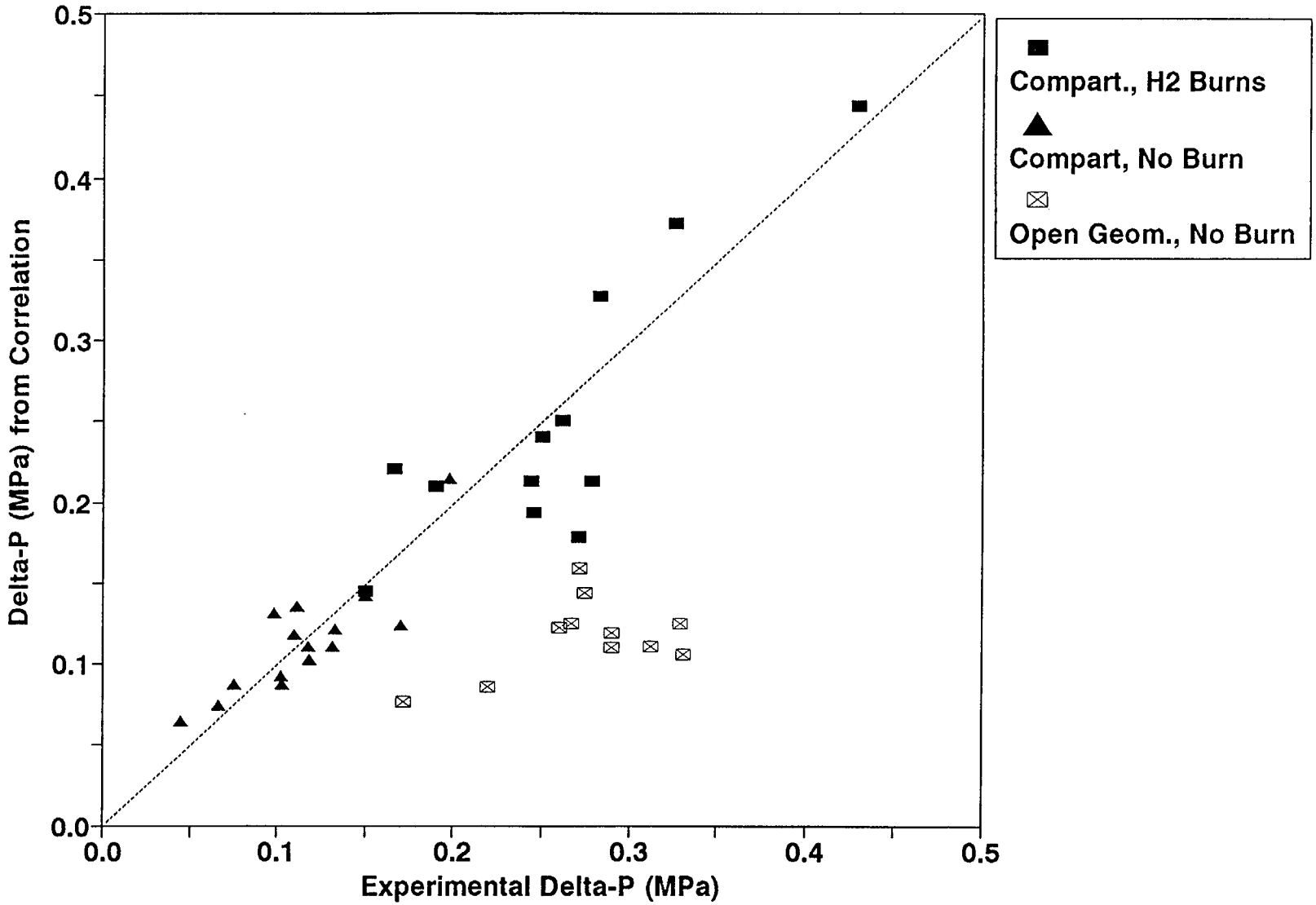

Figure 2.2-1. Correlation of experimental DCH loads based upon the total steam in the accumulator, illustrating some of the differences between open-geometry and compartmentalized cases.

(a)

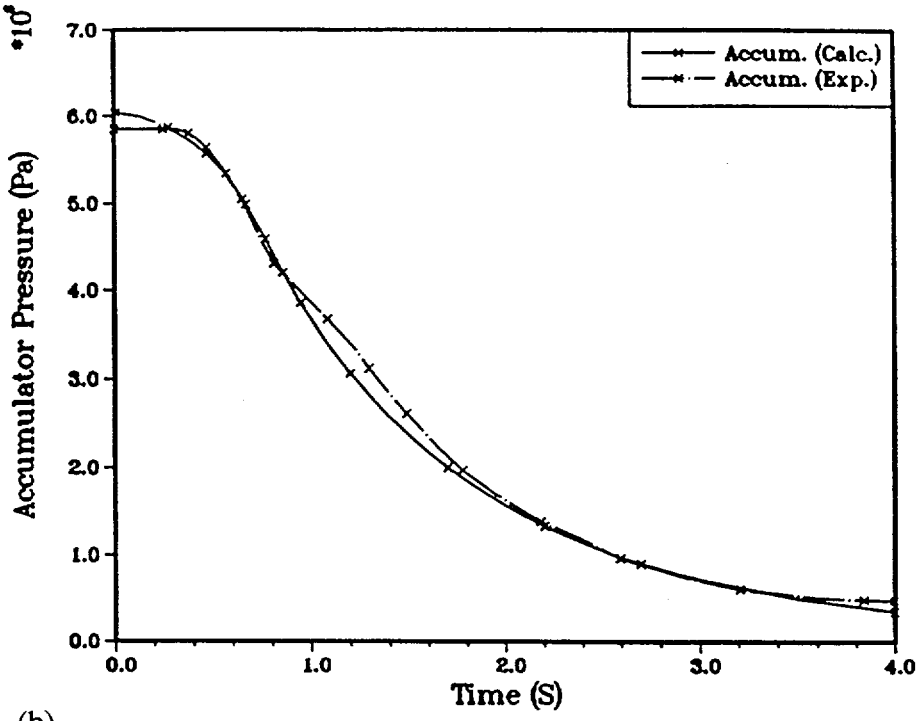

(b)

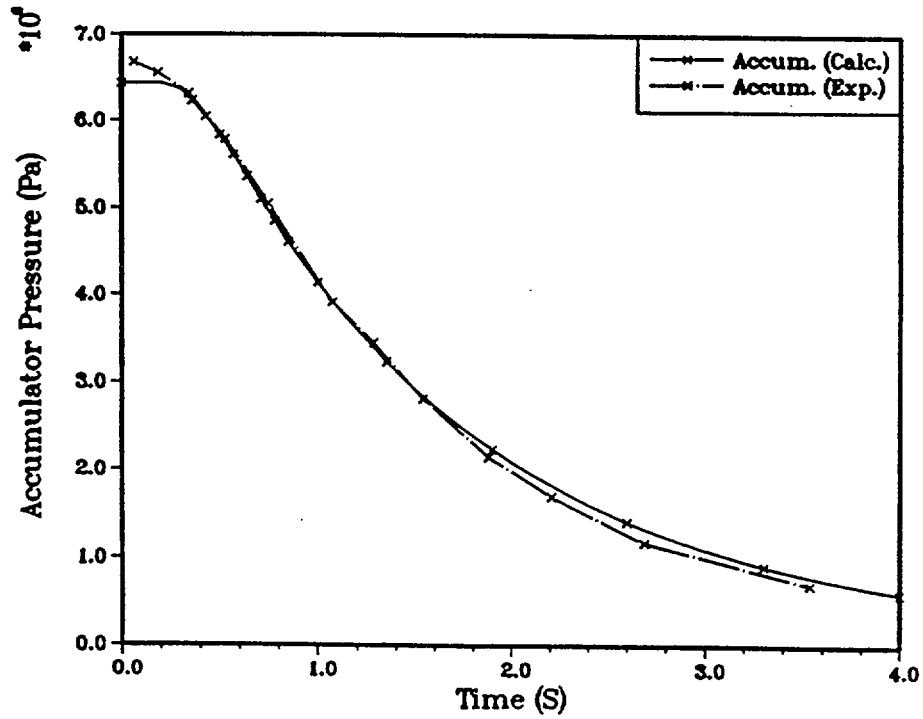

Figure 3.2-1. Comparison between the experimental blowdown curves and the calculated curves used for the standard input prescription for analysis of the IET experiments. (a) SNL/IET-3, (b) SNL/IET-6.

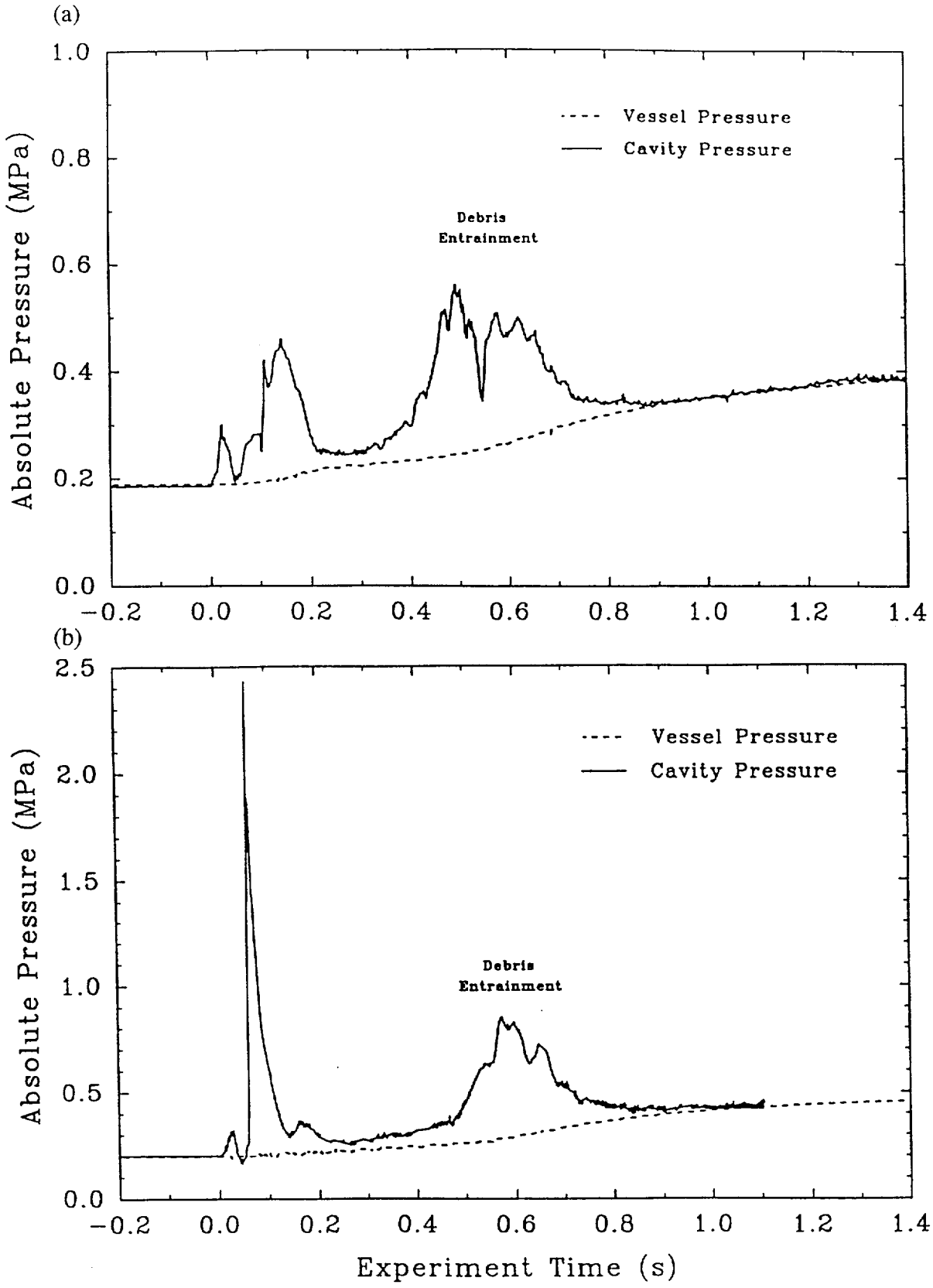

Figure 3.2-2. Experimental pressure-time histories for the cavity and for the Surtsey vessel in (a) the SNL/IET-3 experiment, and (b) SNL/IET-6.

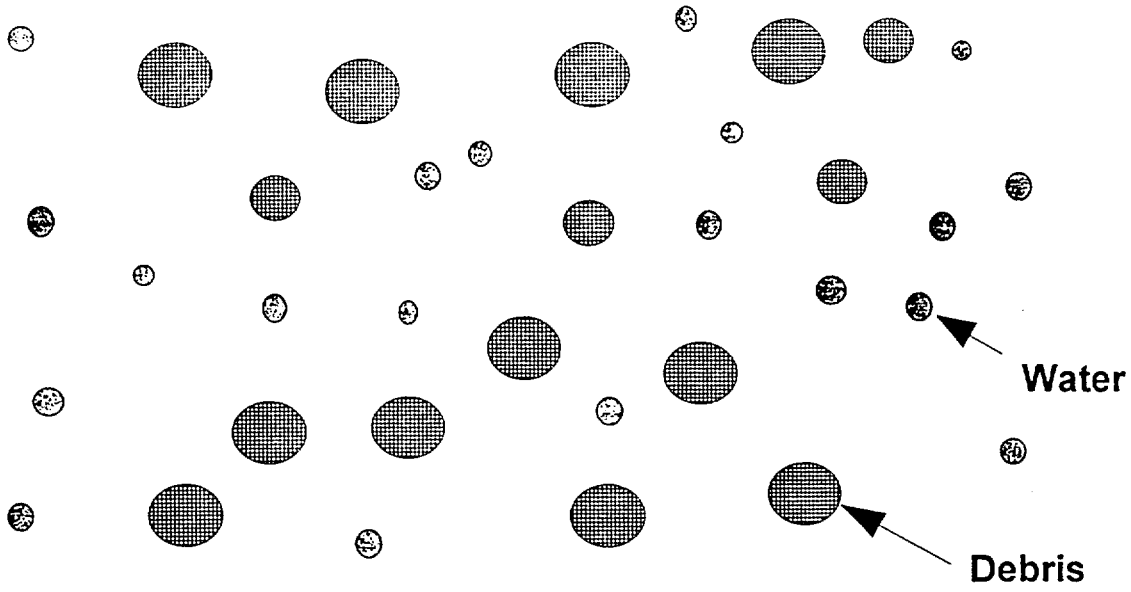

Figure 3.2-3. Dispersed debris and liquid water fields corresponding to the CONTAIN treatment.

(a) schematic corresponding to Figure 3.2-3

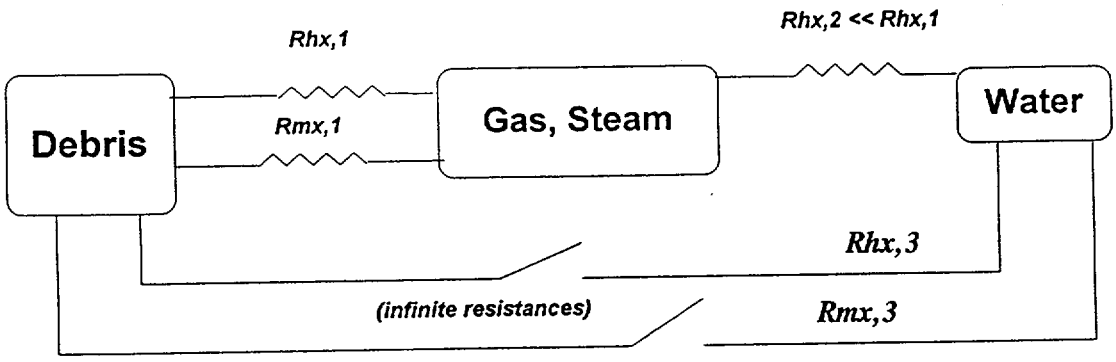

(b) schematic for FCI with direct debris-water contact

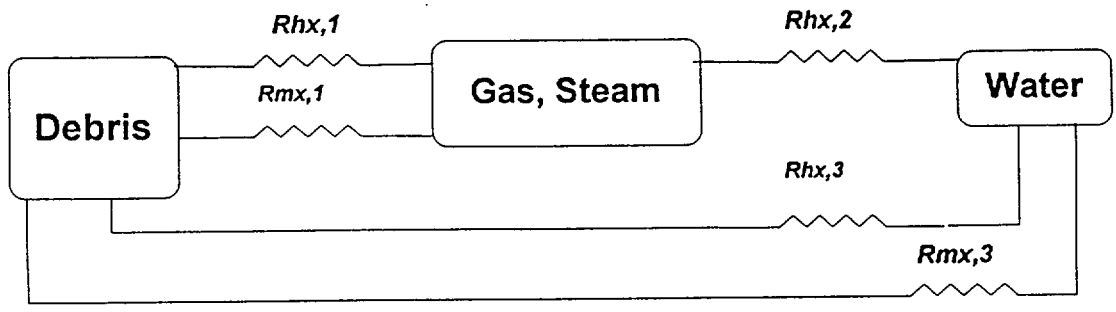

Figure 3.2-4. Heat and mass transfer schematics for debris-water interactions.

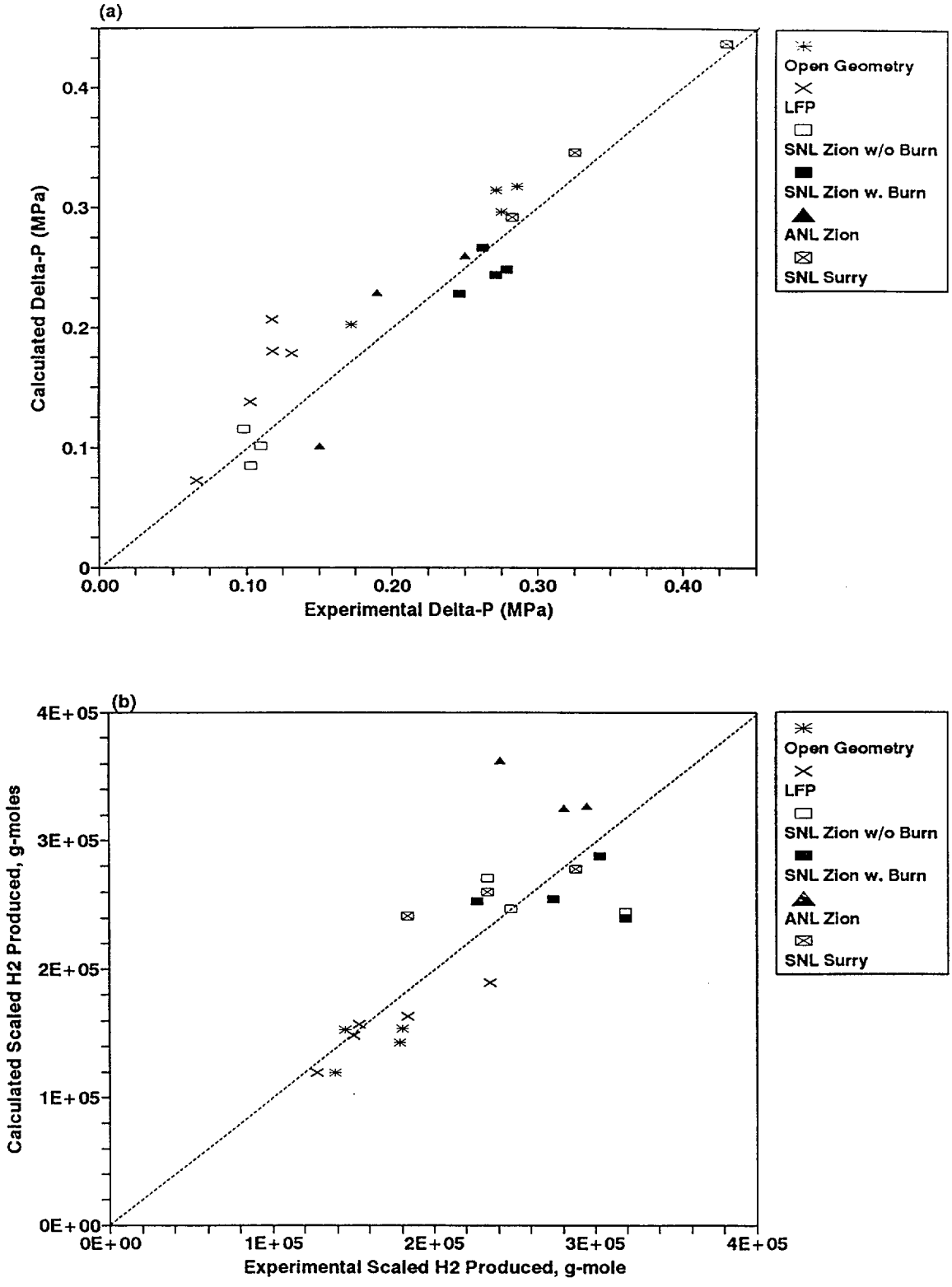

Figure 4.1-1. CONTAIN predictions versus experimental results for (a) ΔP and (b) scaled H_2 production for the standard input prescription (Case 1).

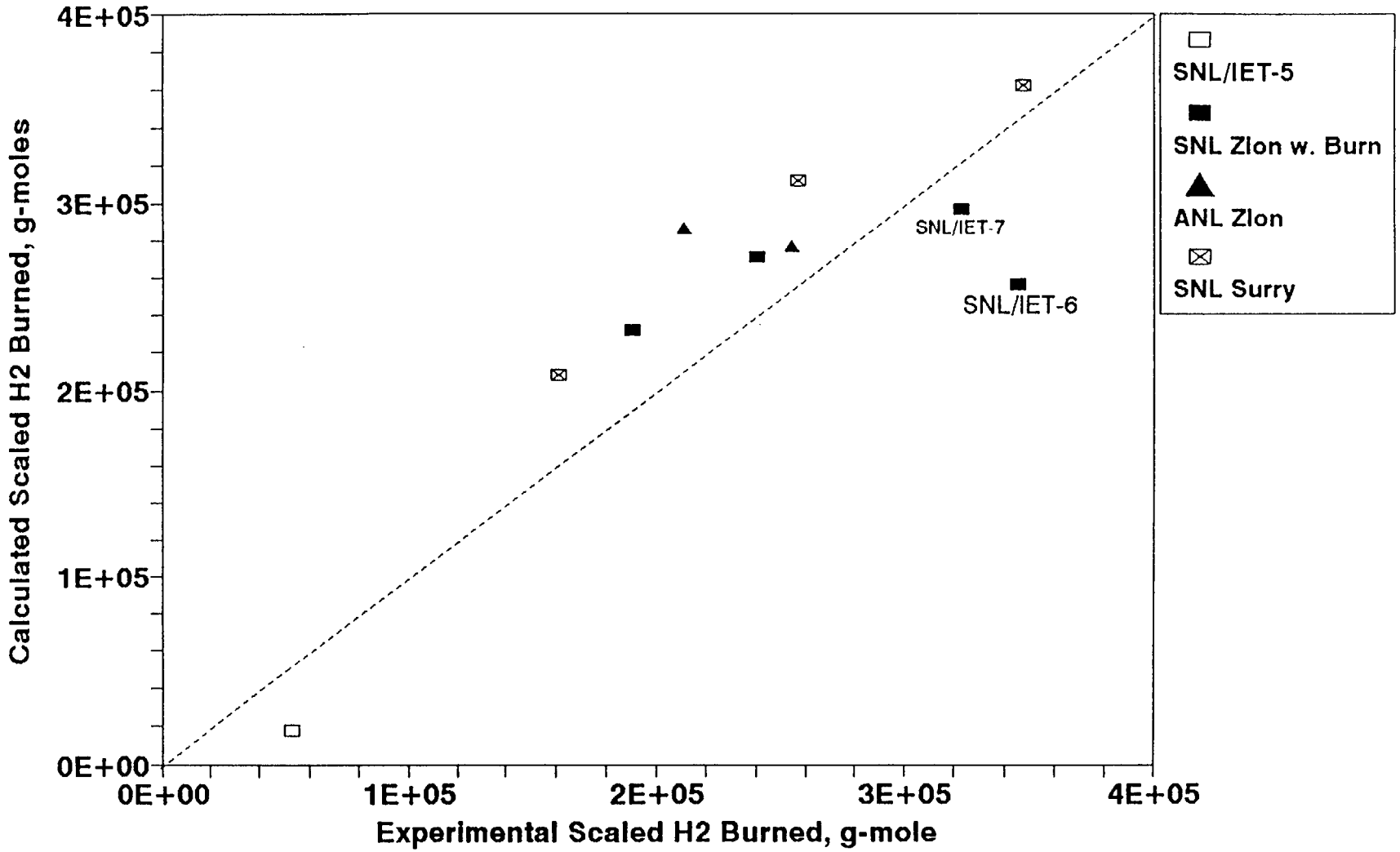

Figure 4.1-2. CONTAIN predictions versus experimental results for scaled H_2 combustion for the standard input prescription.

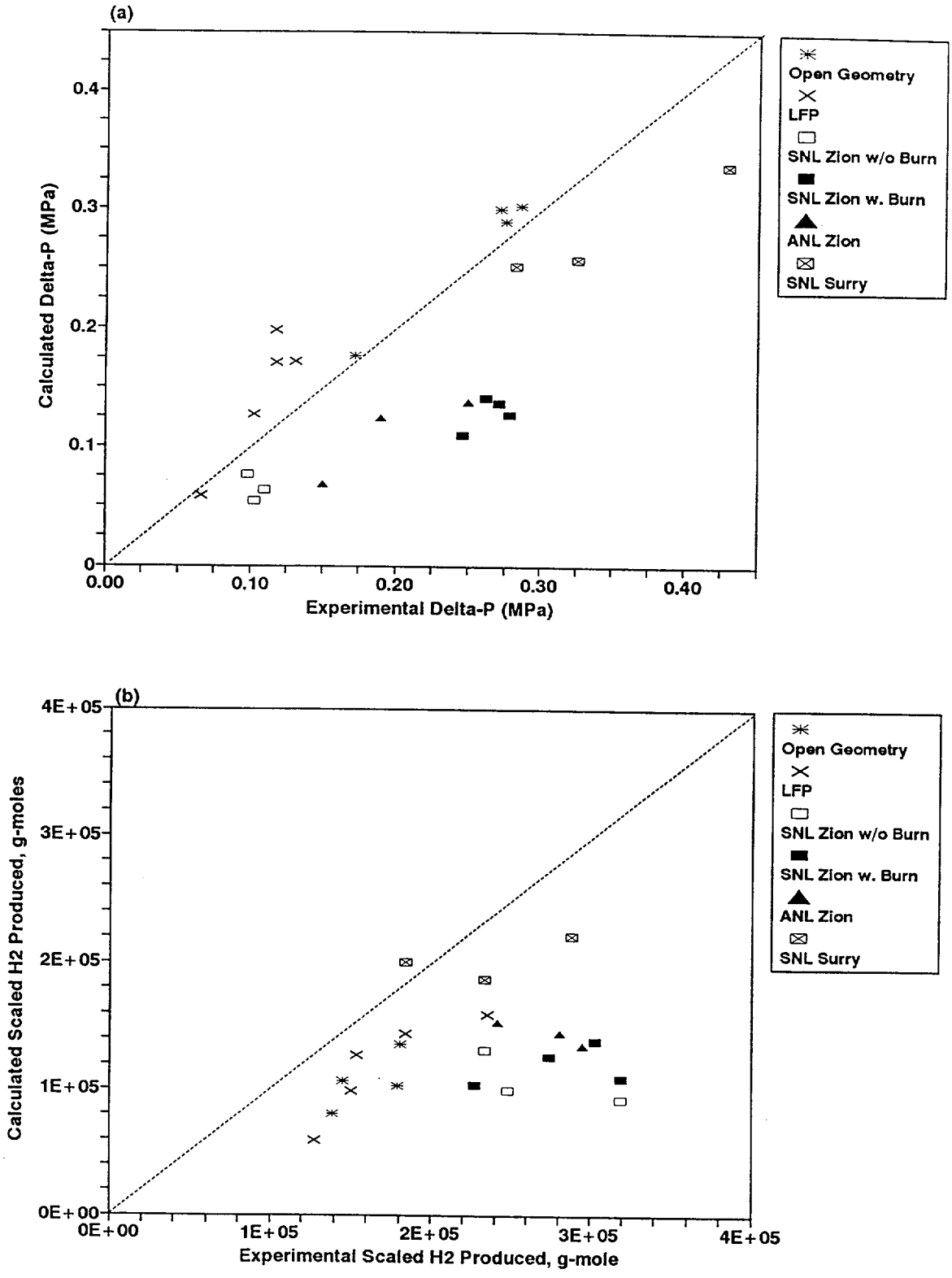

Figure 4.2-1. CONTAIN predictions versus experimental results for (a) ΔP and (b) scaled H_2 production for Case 3 (no nonairborne debris interactions).

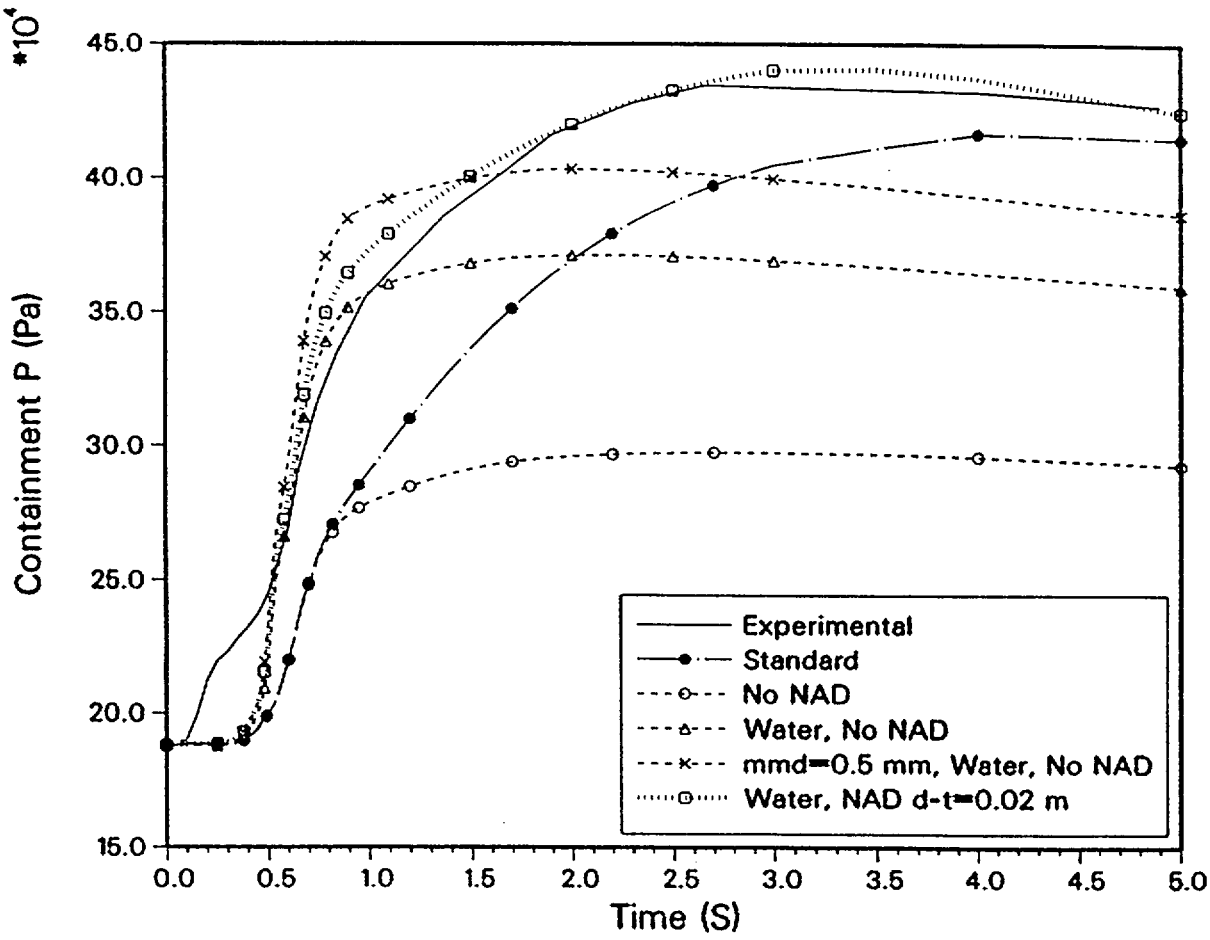

Figure 4.2-2. Comparison of experimental and calculated pressure-time histories for the SNL/IET-3 experiment.

Debris-Water Interactions in Open Containment Geometries. The WC-1 and WC-2 experiments were performed in an open containment geometry and were very similar except that WC-1 had a dry cavity while WC-2 had 11.76 kg of water in the cavity. Experimental results showed very little difference in ΔP while WC-2 yielded about 25% more hydrogen. Previous analyses [All92a] indicated that debris-water interactions were inefficient in this experiment and CONTAIN results summarized in Section 6.4.2 support this conclusion. The CONTAIN analyses predict no increase in ΔP due to the water in WC-2, whatever the efficiency of the cavity interaction. It appears, therefore, that the effects of water in compartmentalized geometries generally cannot be inferred from the results of experiments performed in open containment geometries; see Sections 6.4.2 and 6.4.4 for details.

4.2.3 Re-examination of the Case 3 Interpretations

Traditionally, DCH modeling has emphasized (often exclusively) the interactions between airborne debris and the containment atmosphere and/or blowdown steam, which are just the

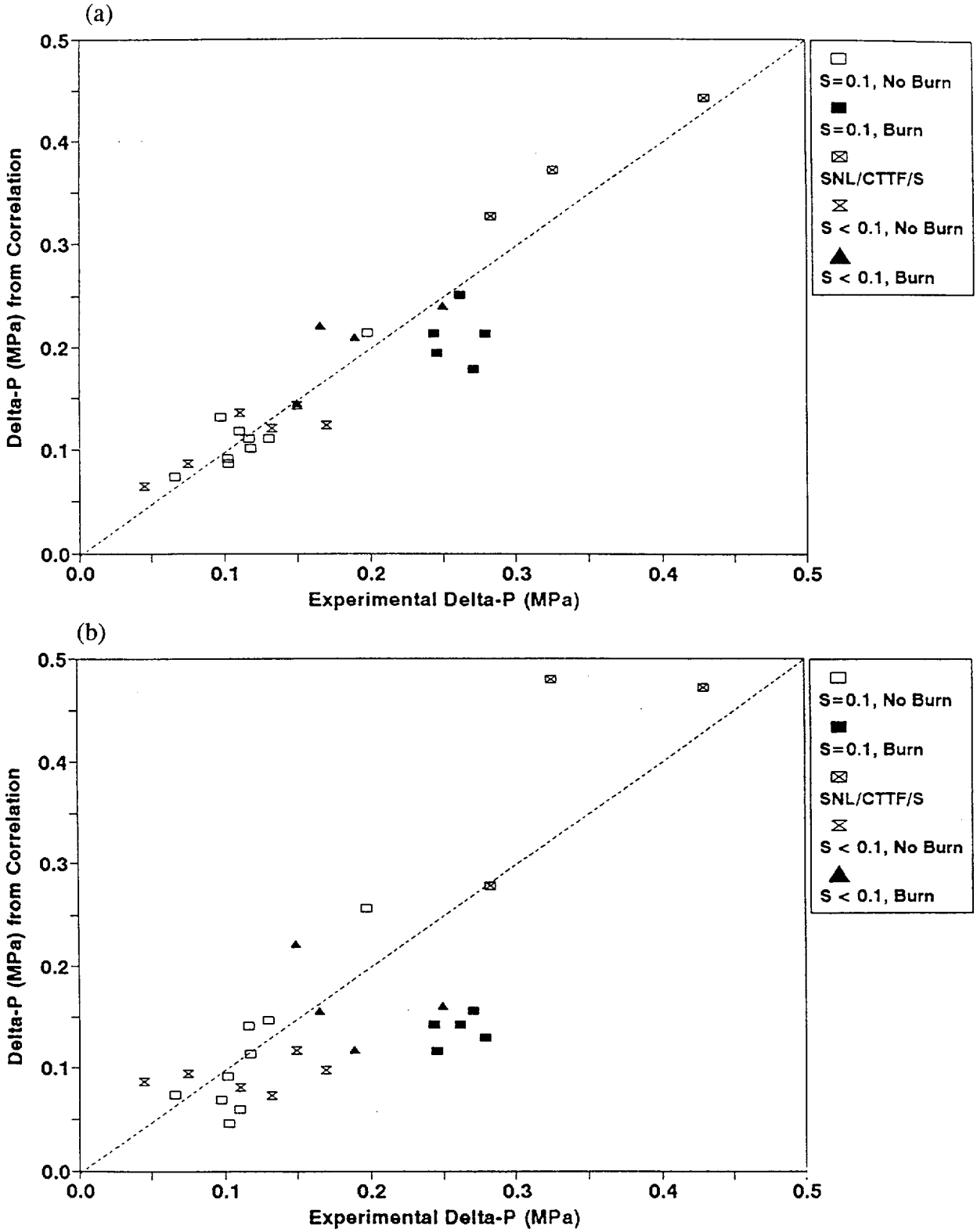

Figure 4.2-3. Comparison of (a) the total steam correlation for experimental DCH loads with (b) the coherent steam correlation. (Compartmentalized cases only.)

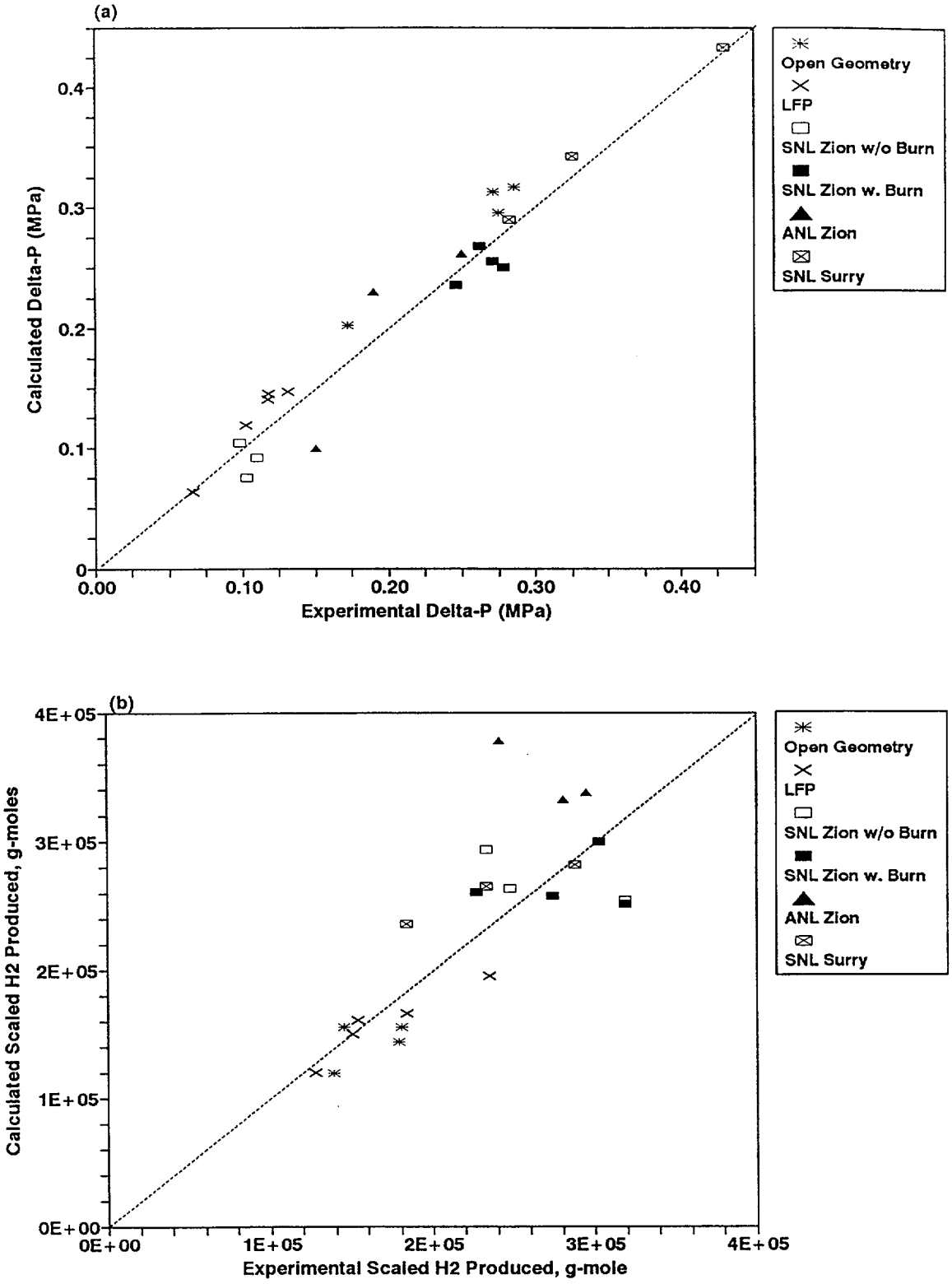

Figure 4.3-1. CONTAIN predictions versus experimental results for (a) ΔP and (b) scaled H_2 production for Case 4 (slip = 5 in the subcompartments).

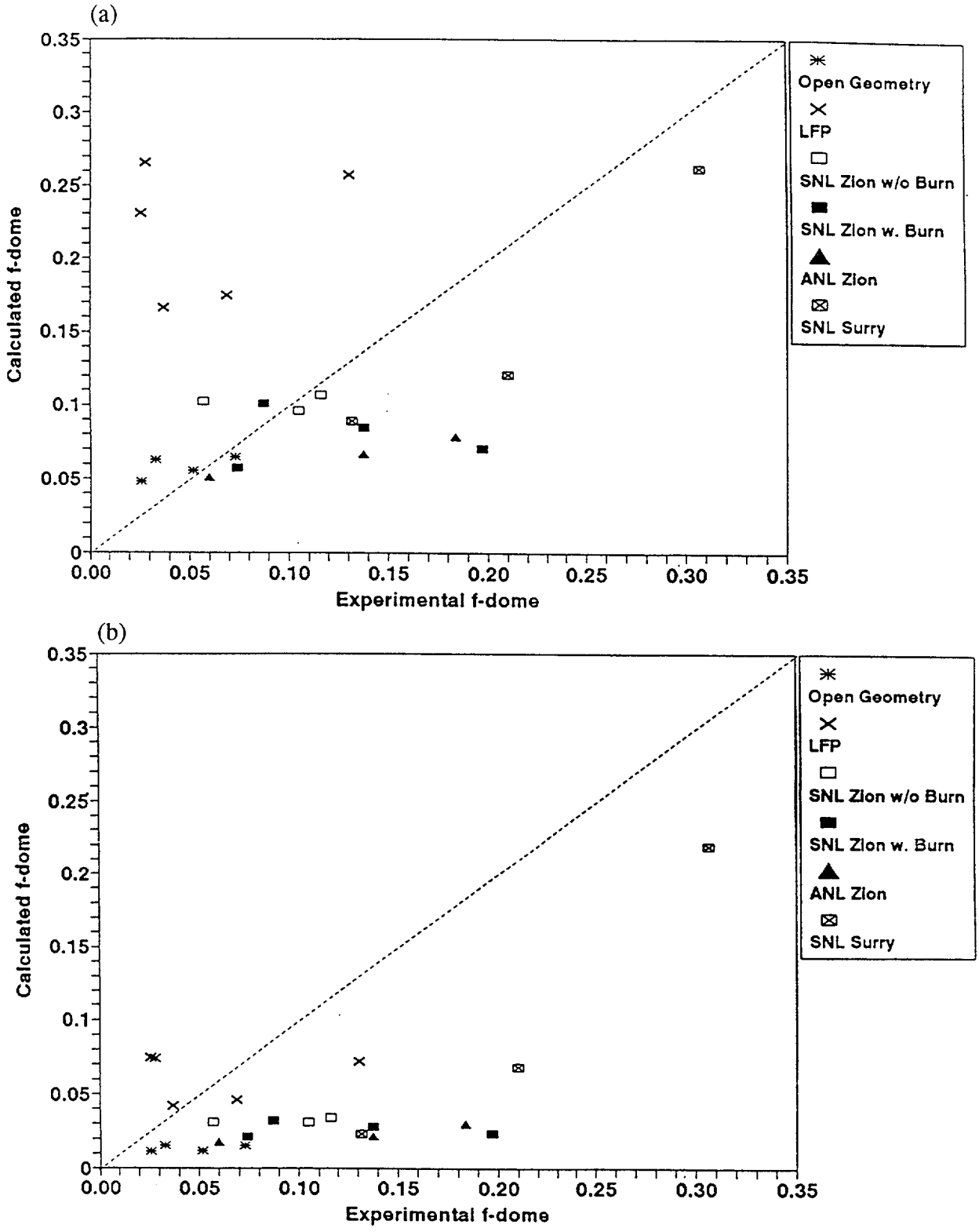

Figure 4.3-2. CONTAIN predictions versus experimental results for fraction of debris transported beyond the subcompartments (f_{dome}) in (a) Case 1 and (b) Case 4.

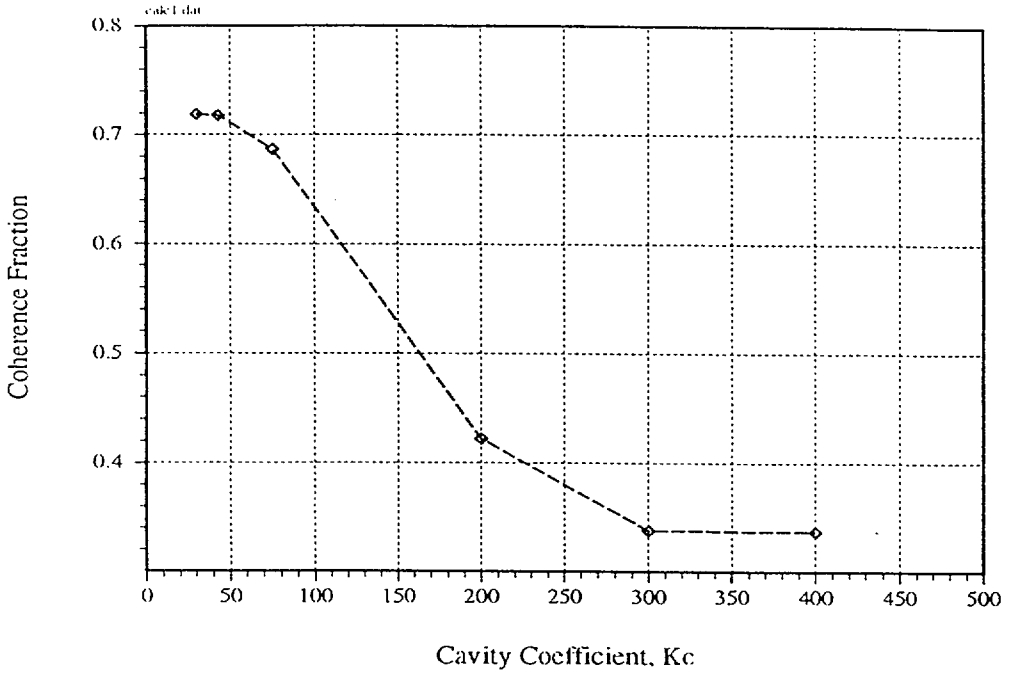

Figure 5.3-1. Coherent steam fraction as a function of the cavity coefficient, K_c, for the Whalley-Hewitt model.

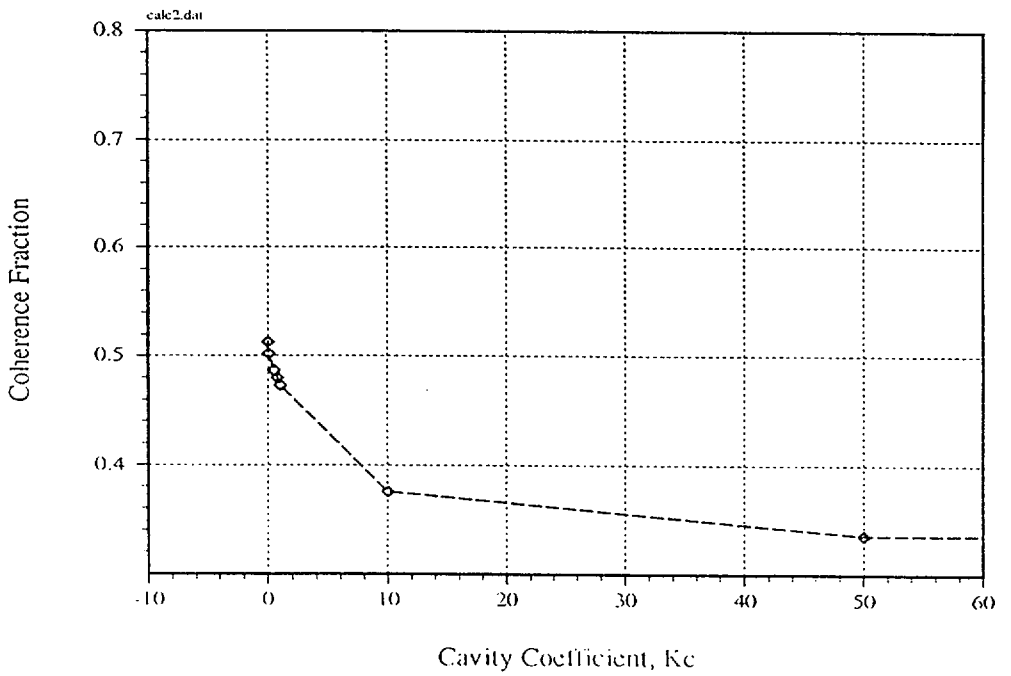

Figure 5.3-2. Coherent steam fraction as a function of the cavity coefficient, K_c, for the Levy model.

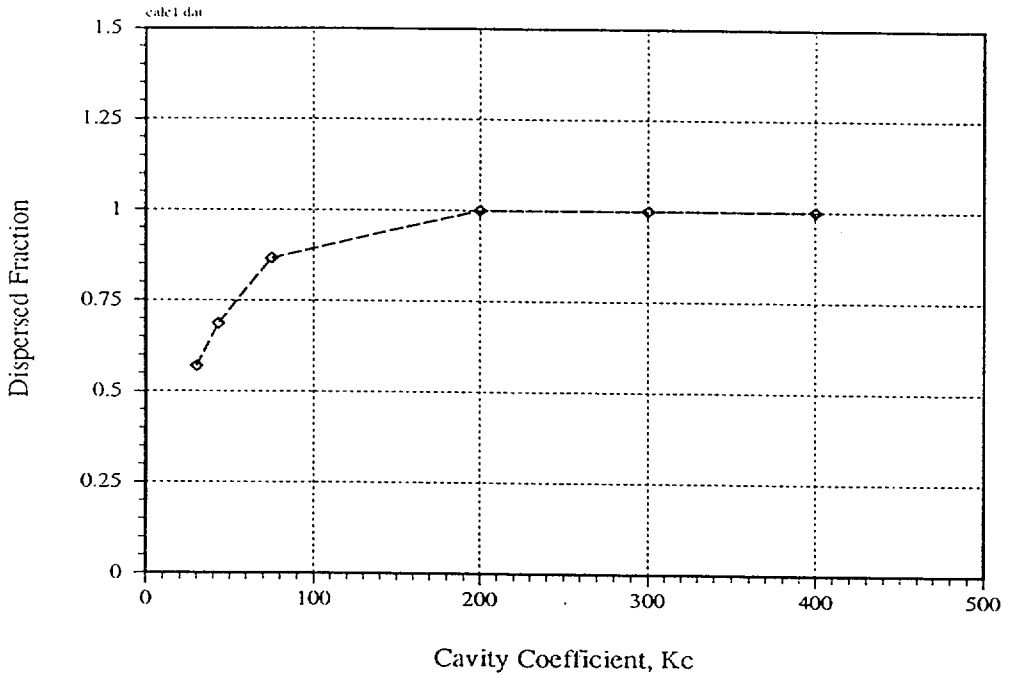

Figure 5.3-3. Dispersed fraction as a function of K_c for the Whalley-Hewitt model.

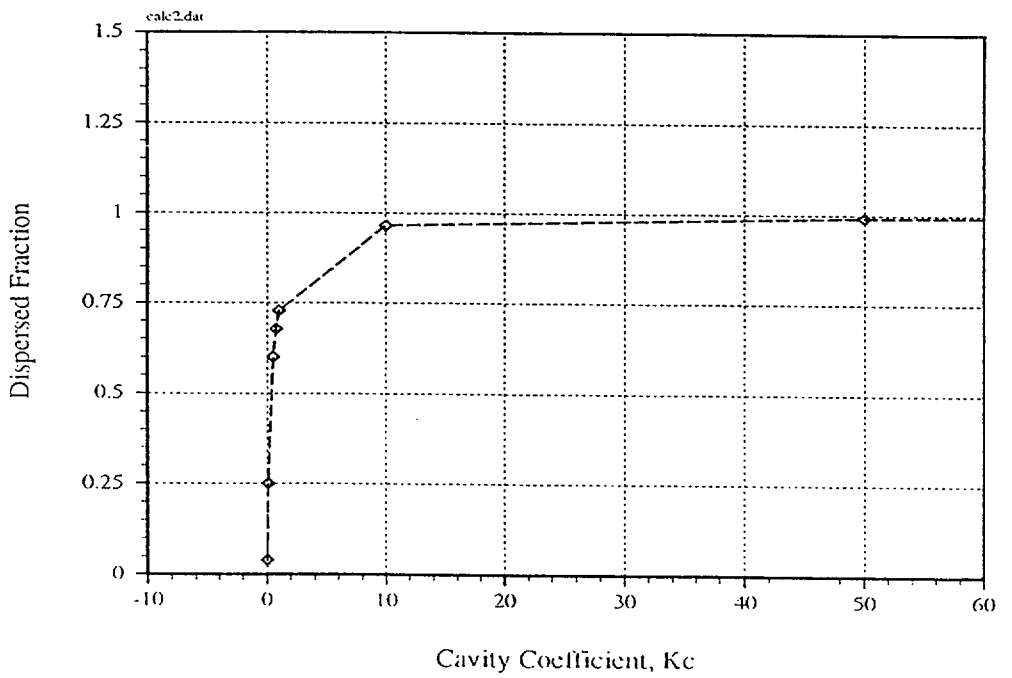

Figure 5.3-4. Dispersed fraction as a function of K_c for the Levy model.

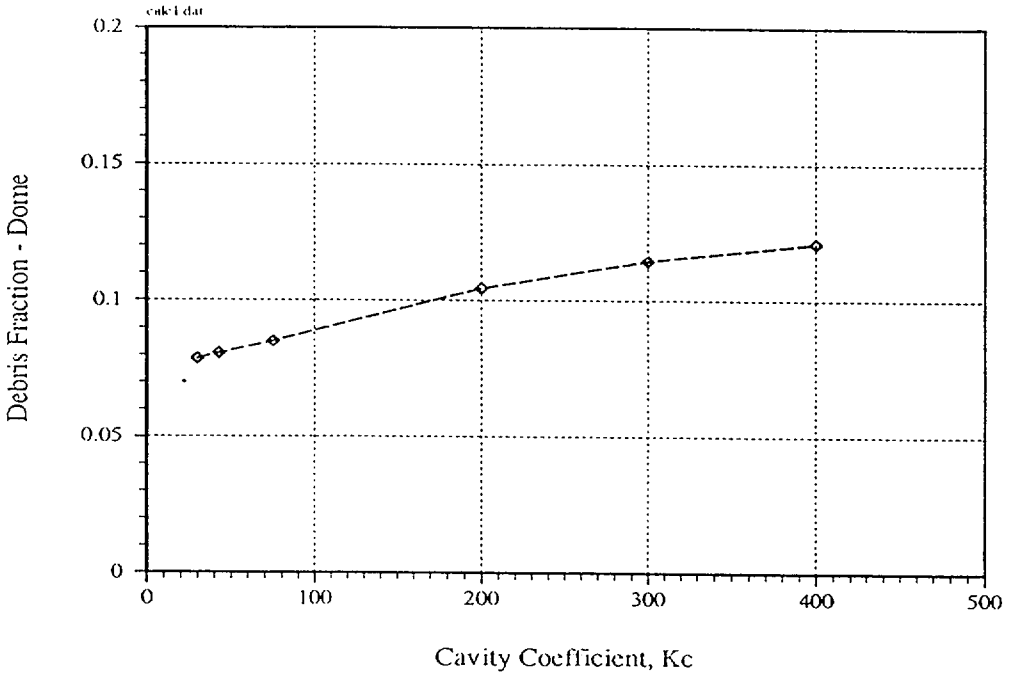

Figure 5.3-5. Dome transport fraction as a function of K_c for the Whalley-Hewitt model.

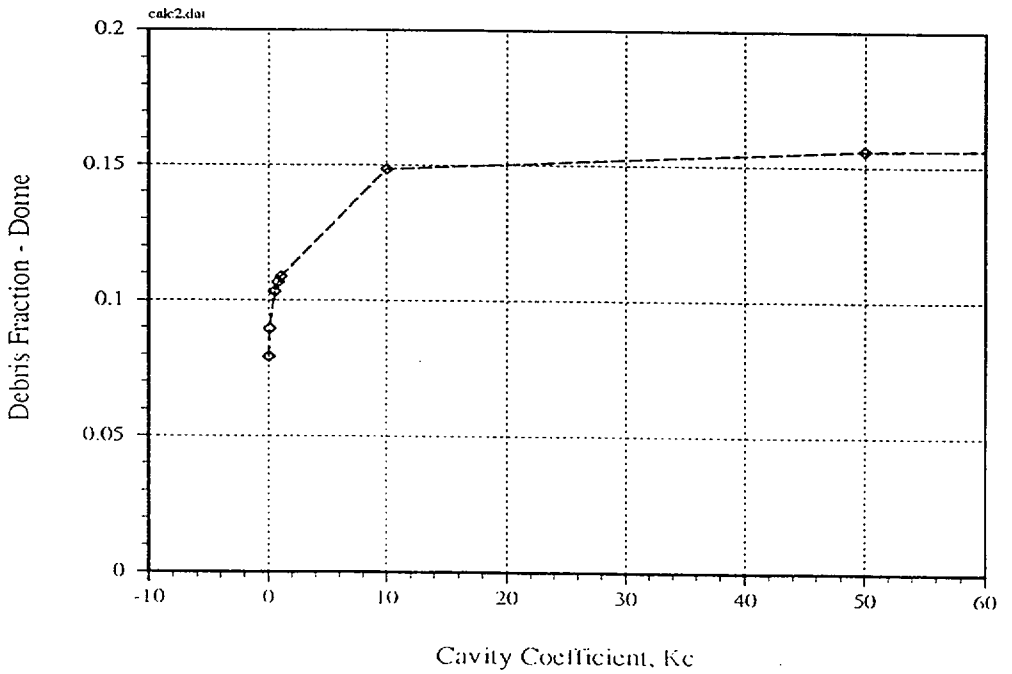

Figure 5.3-6. Dome transport fraction as a function of K_c for the Levy model.

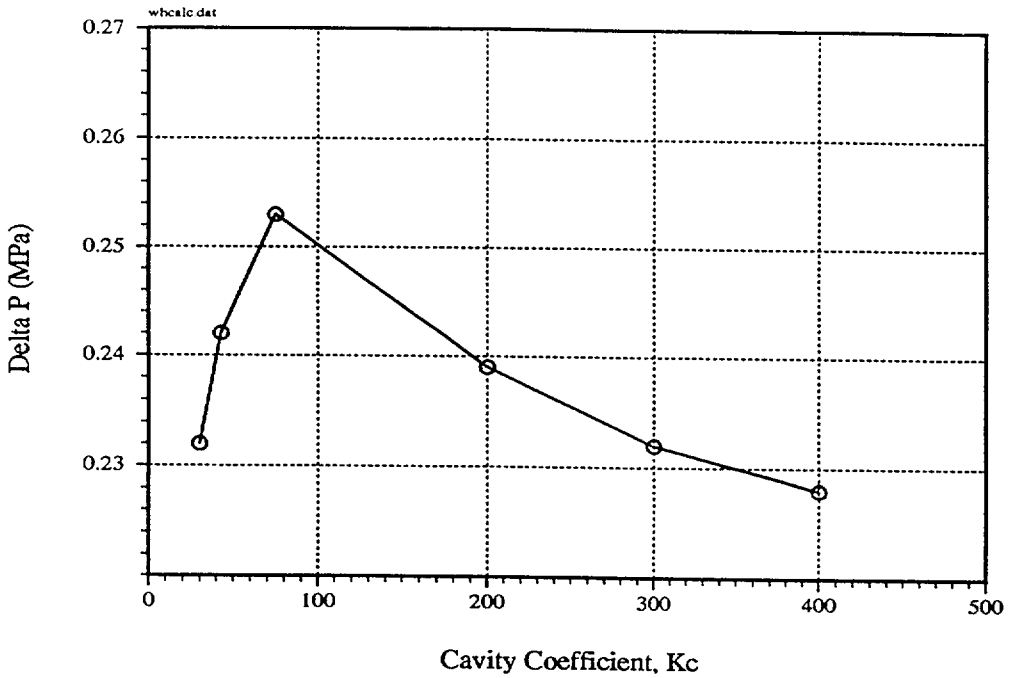

Figure 5.3-7. ΔP as a function of K_c for the Whalley-Hewitt model.

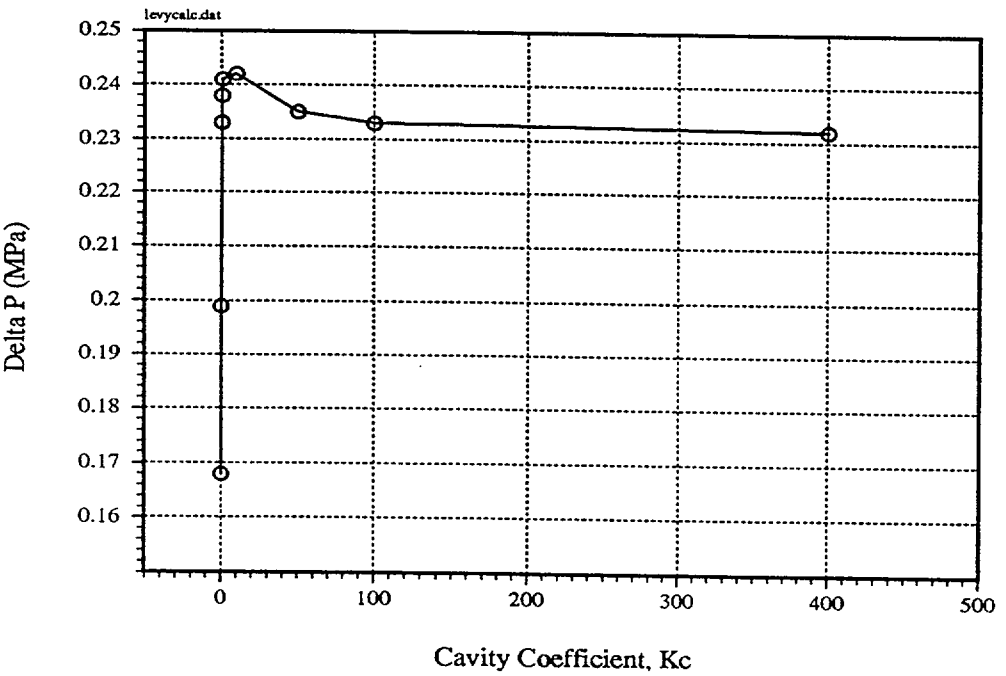

Figure 5.3-8. ΔP as a function of K_c for the Levy model.

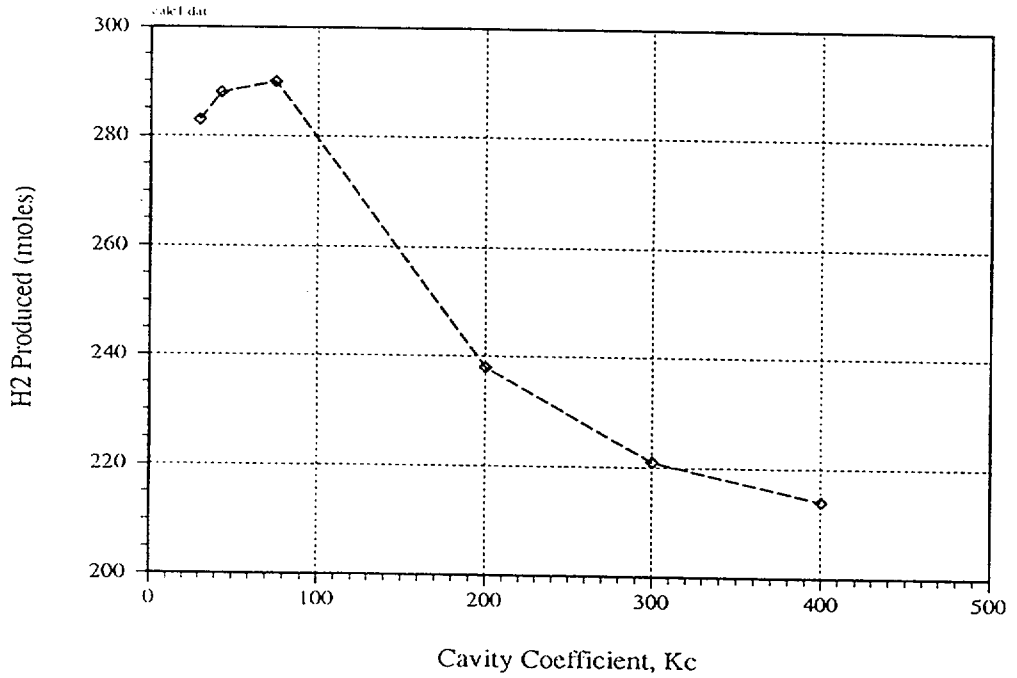

Figure 5.3-9. Hydrogen produced as a function of K_c for the Whalley-Hewitt model.

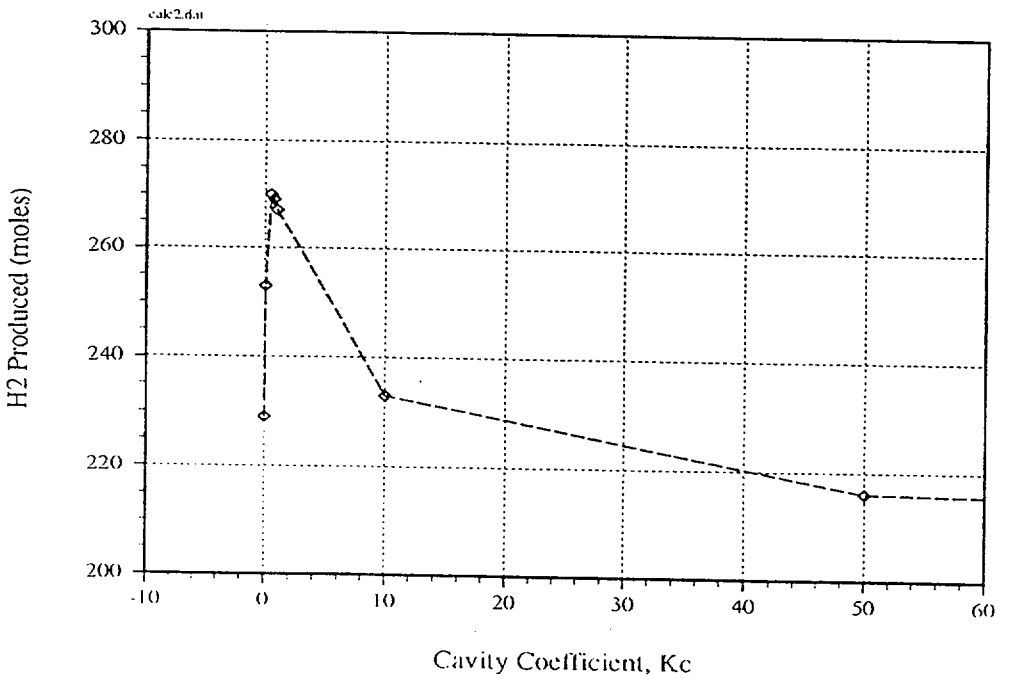

Figure 5.3-10. Hydrogen produced as a function of K_c for the Levy model.

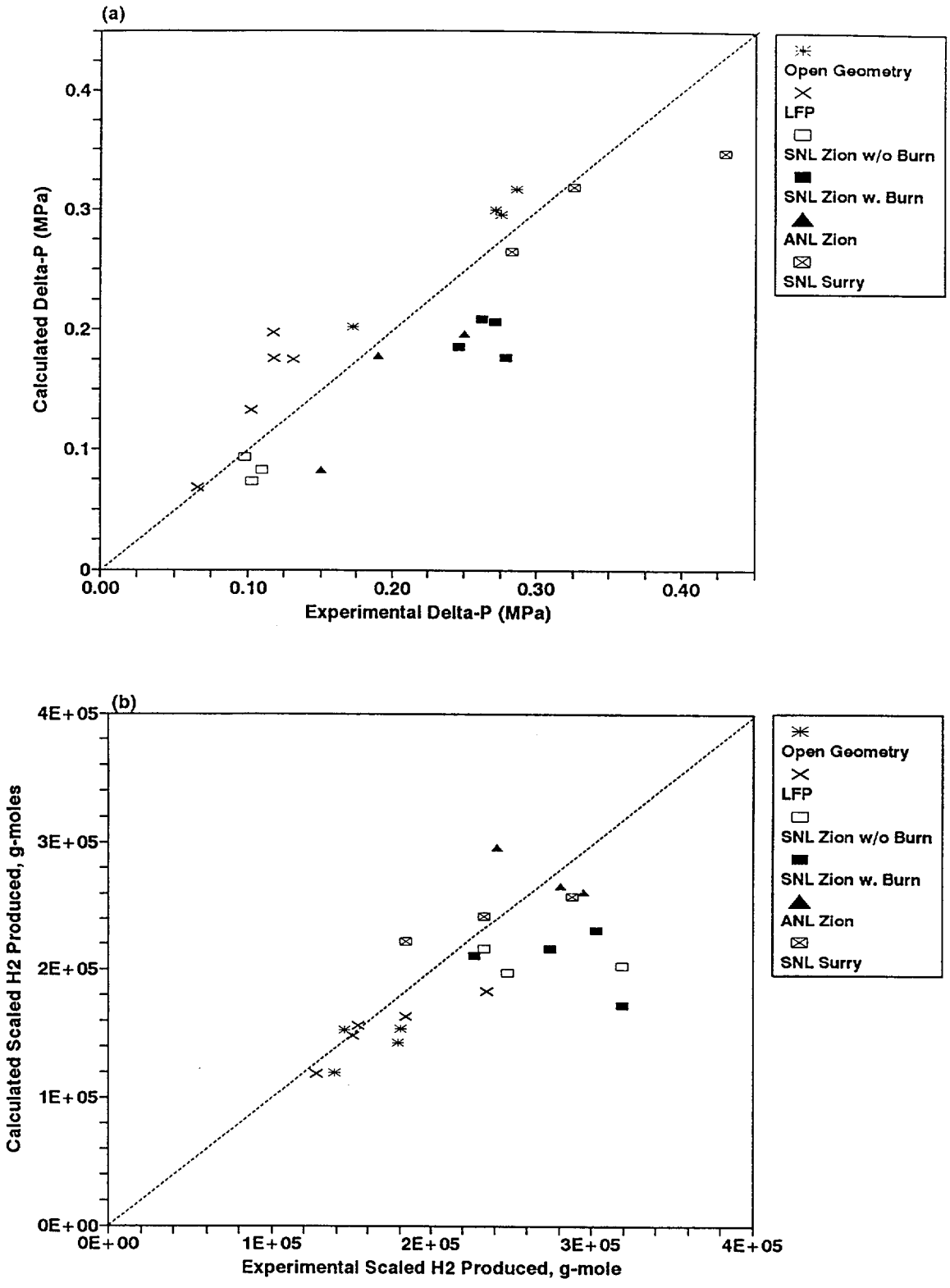

Figure 6.3-1. CONTAIN predictions versus experimental results for (a) ΔP and (b) scaled H_2 production with NAD modeled in the cavity only.

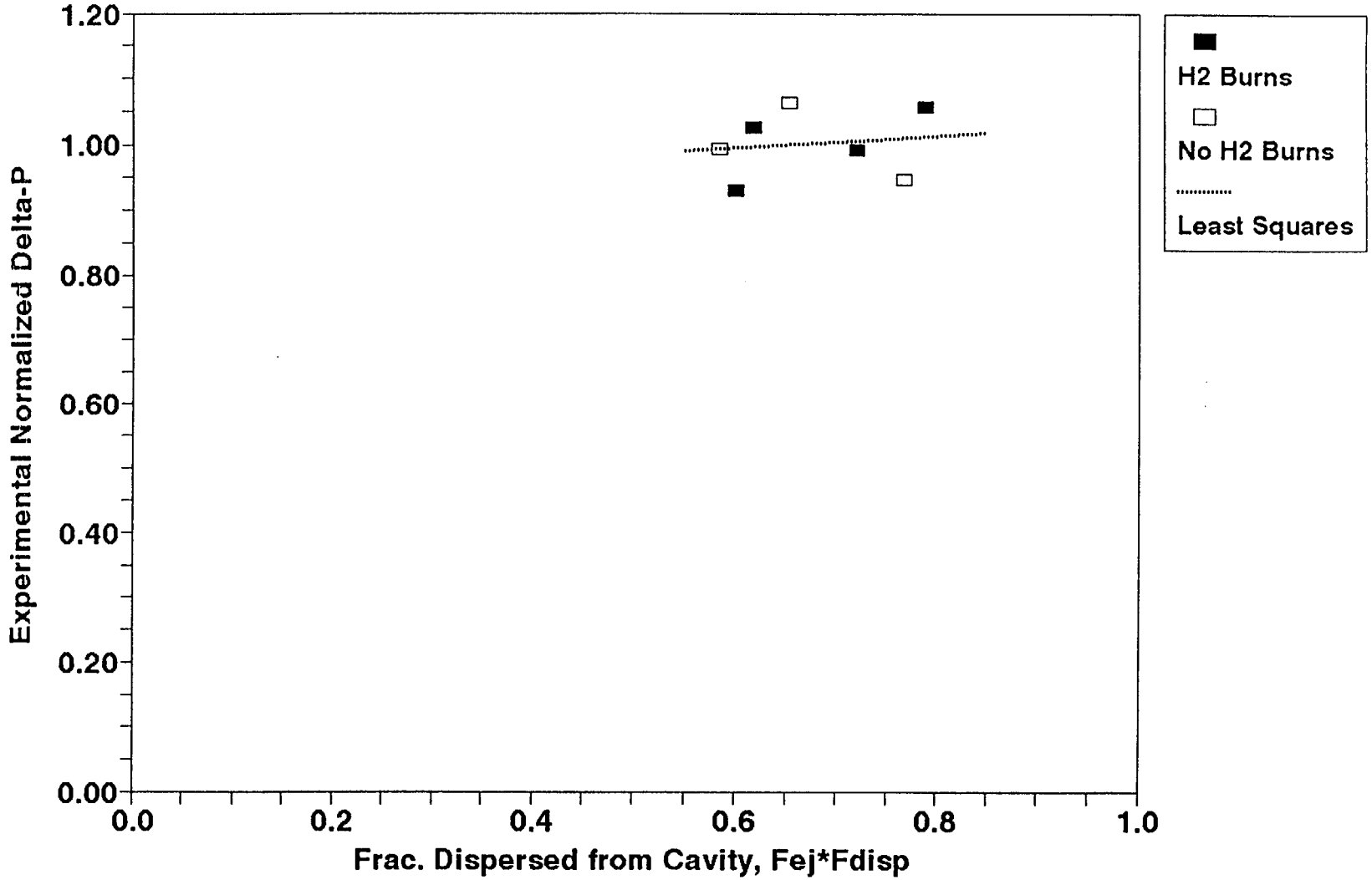

Figure 6.3-2. Normalized experimental ΔP values plotted against debris fractions dispersed from the cavity for the SNL/IET Zion experiments.

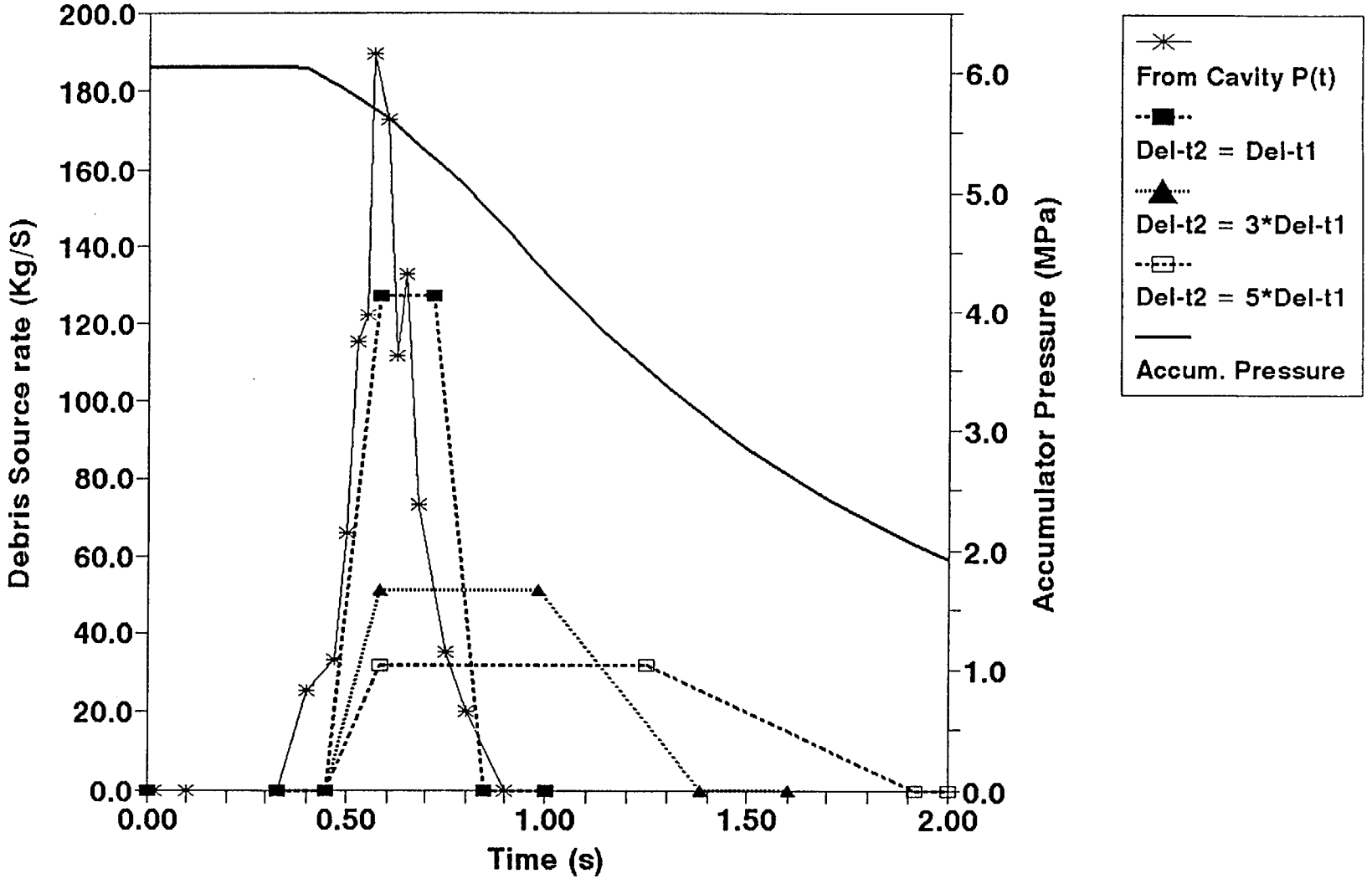

Figure 6.3-3 Debris source time dependencies (left axis) and accumulator blowdown history (right axis) used in the coherence sensitivity study based upon the SNL/IET-6 experiment.

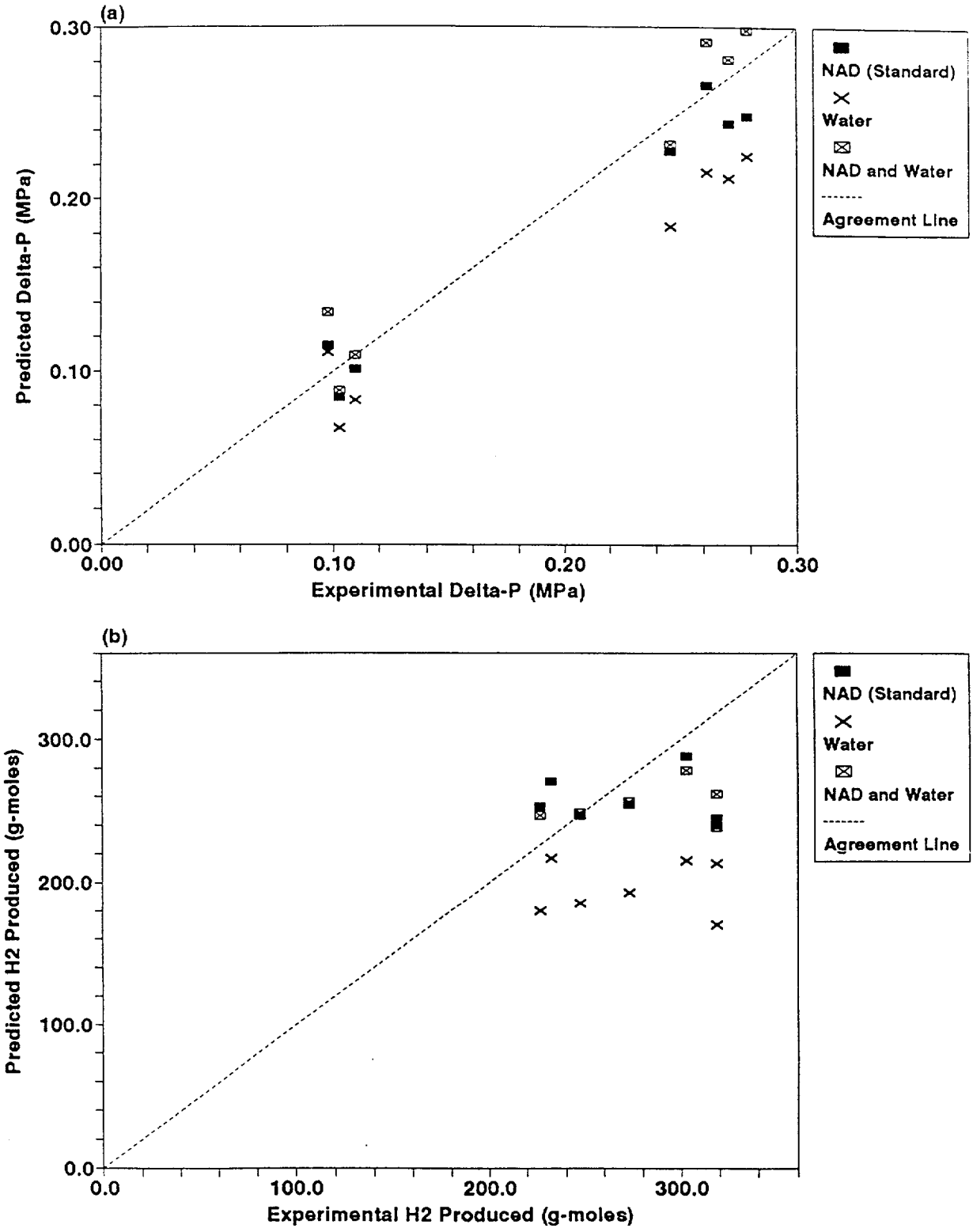

Figure 6.4-1. CONTAIN predictions versus SNL/IET Zion experimental results for (a) ΔP and (b) hydrogen production, for alternative assumptions concerning contributions of nonairborne debris interactions and/or debris-water interactions.

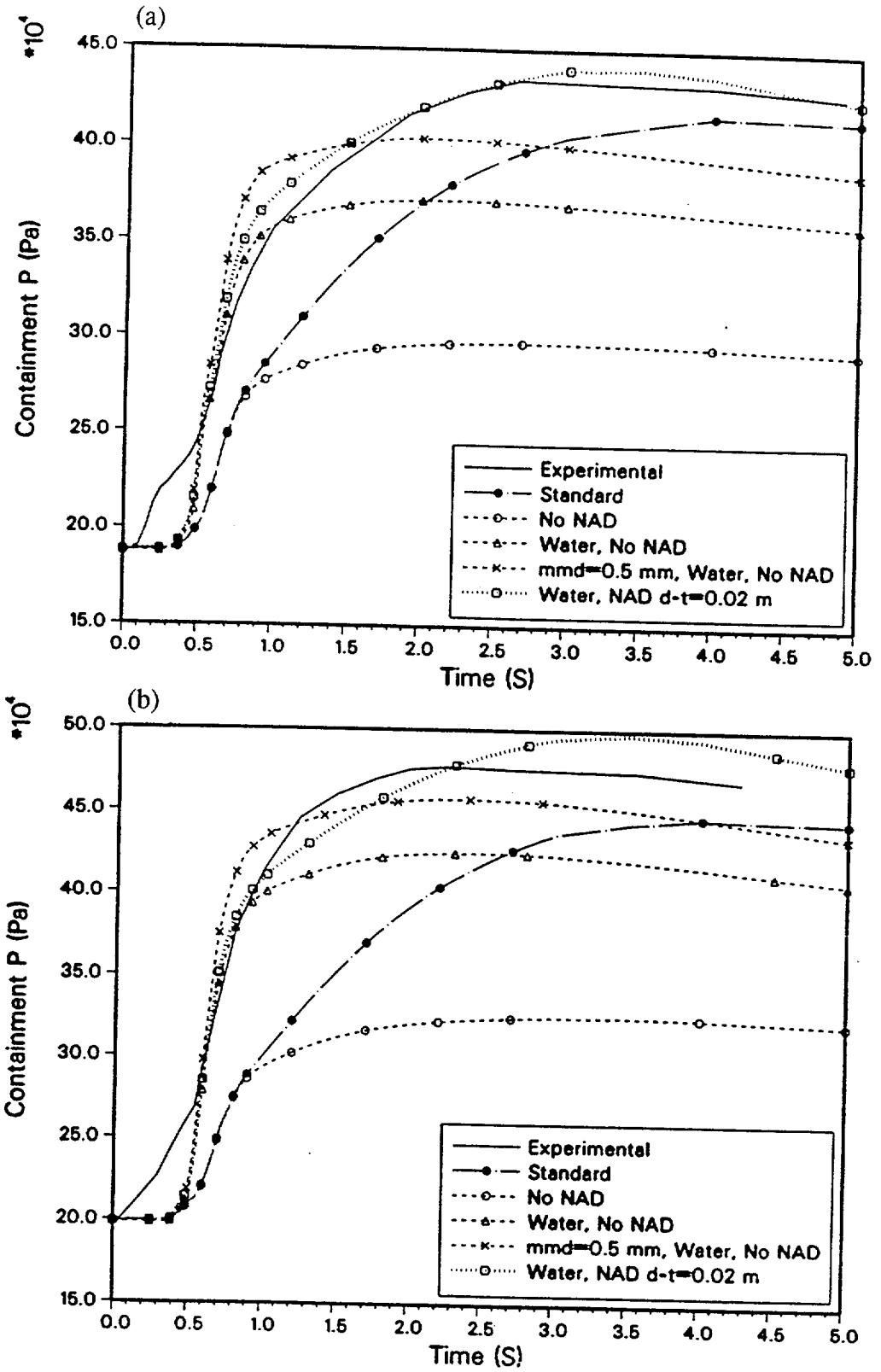

Figure 6.5-1. Experimental and calculated dome pressure-time histories for (a) SNL/IET-3 and (b) SNL/IET-6, for alternative assumptions concerning nonairborne debris and/or debris-water interactions.

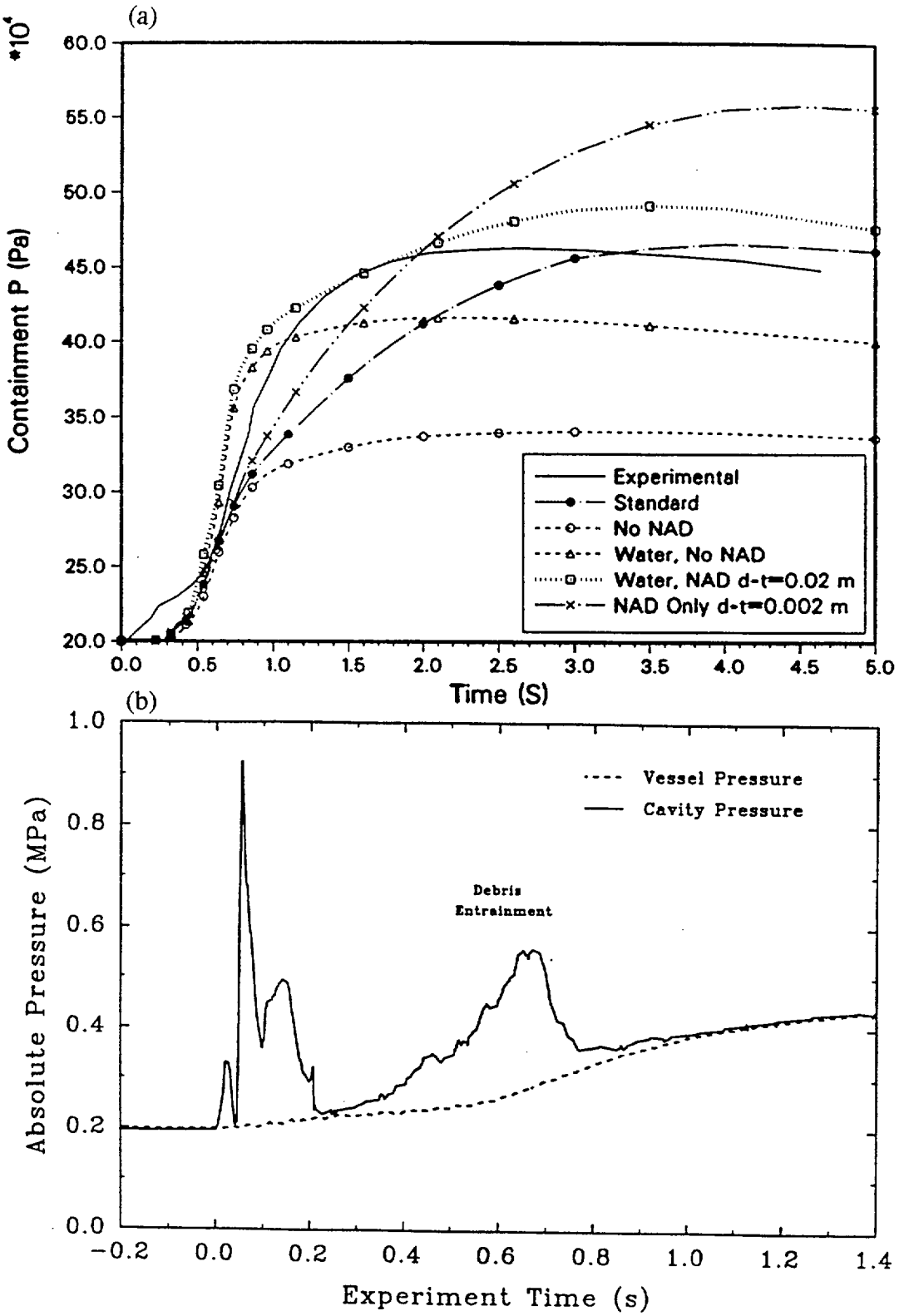

Figure 6.5-2. (a) Experimental and calculated dome pressure-time histories and (b) experimental cavity pressurization histories for the SNL/IET-4 experiment.

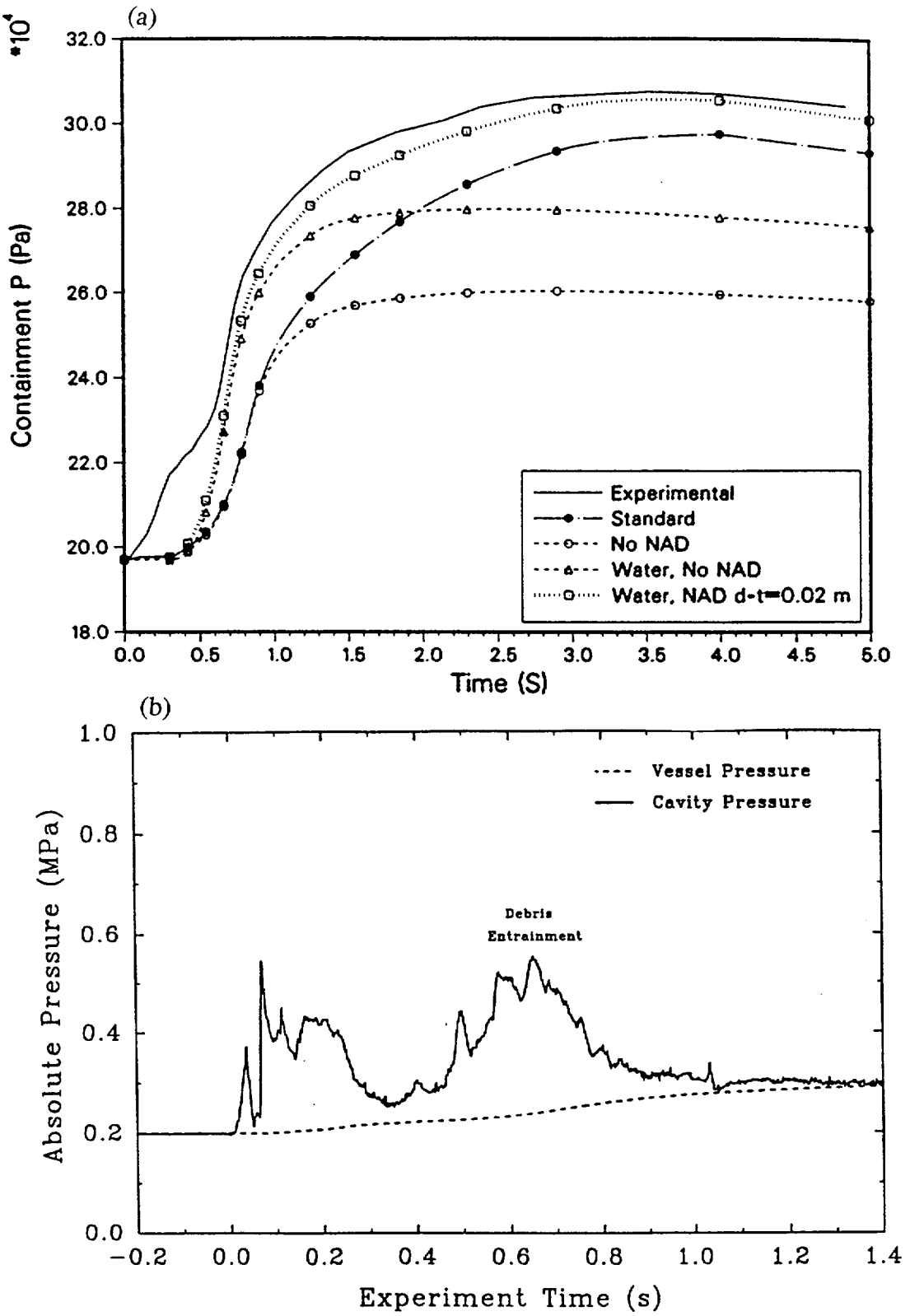

Figure 6.5-3. (a) Experimental and calculated dome pressure-time histories and (b) experimental cavity pressurization histories for the SNL/IET-1R experiment.

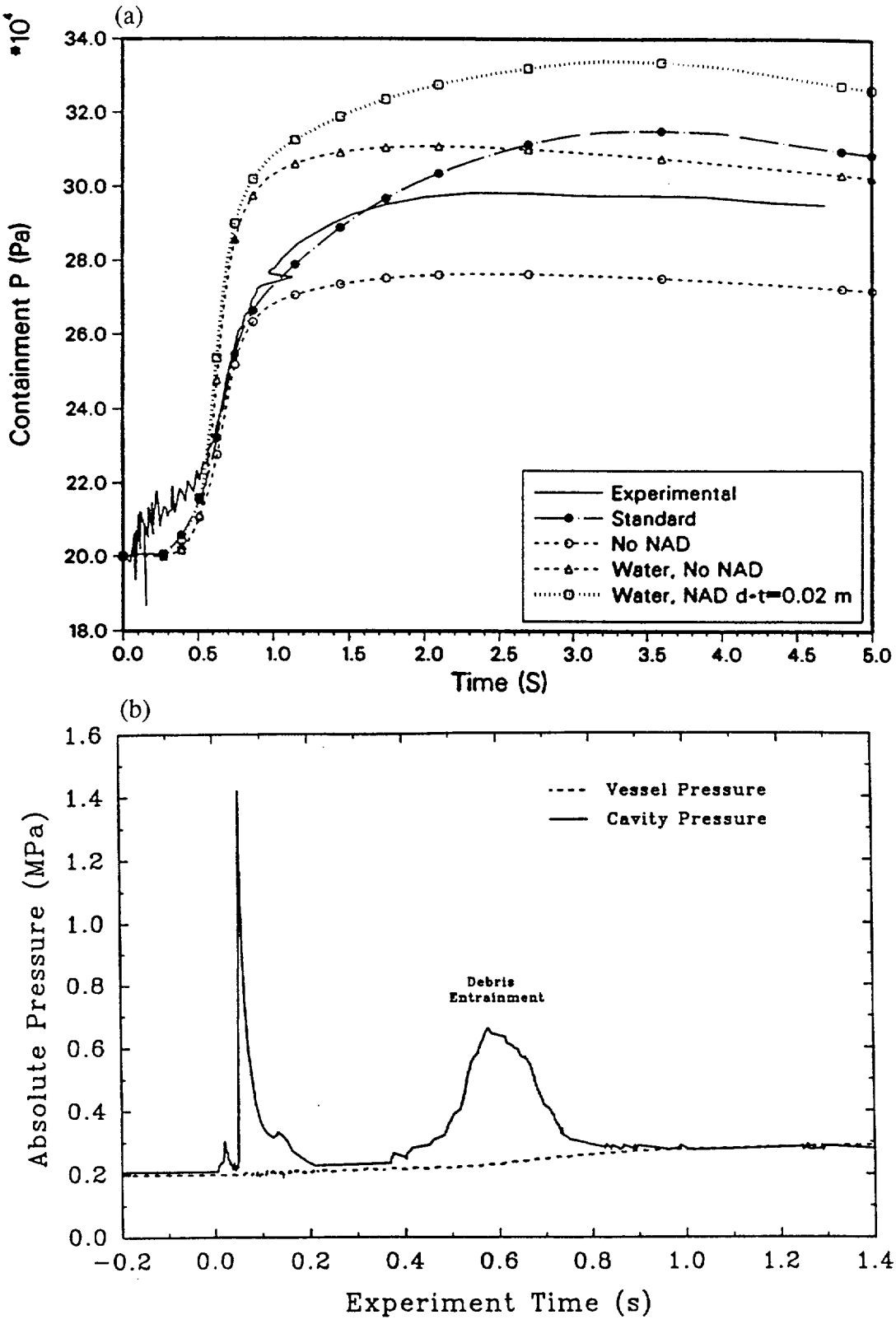

Figure 6.5-4. (a) Experimental and calculated dome pressure-time histories and (b) experimental cavity pressurization histories for the SNL/IET-1 experiment.

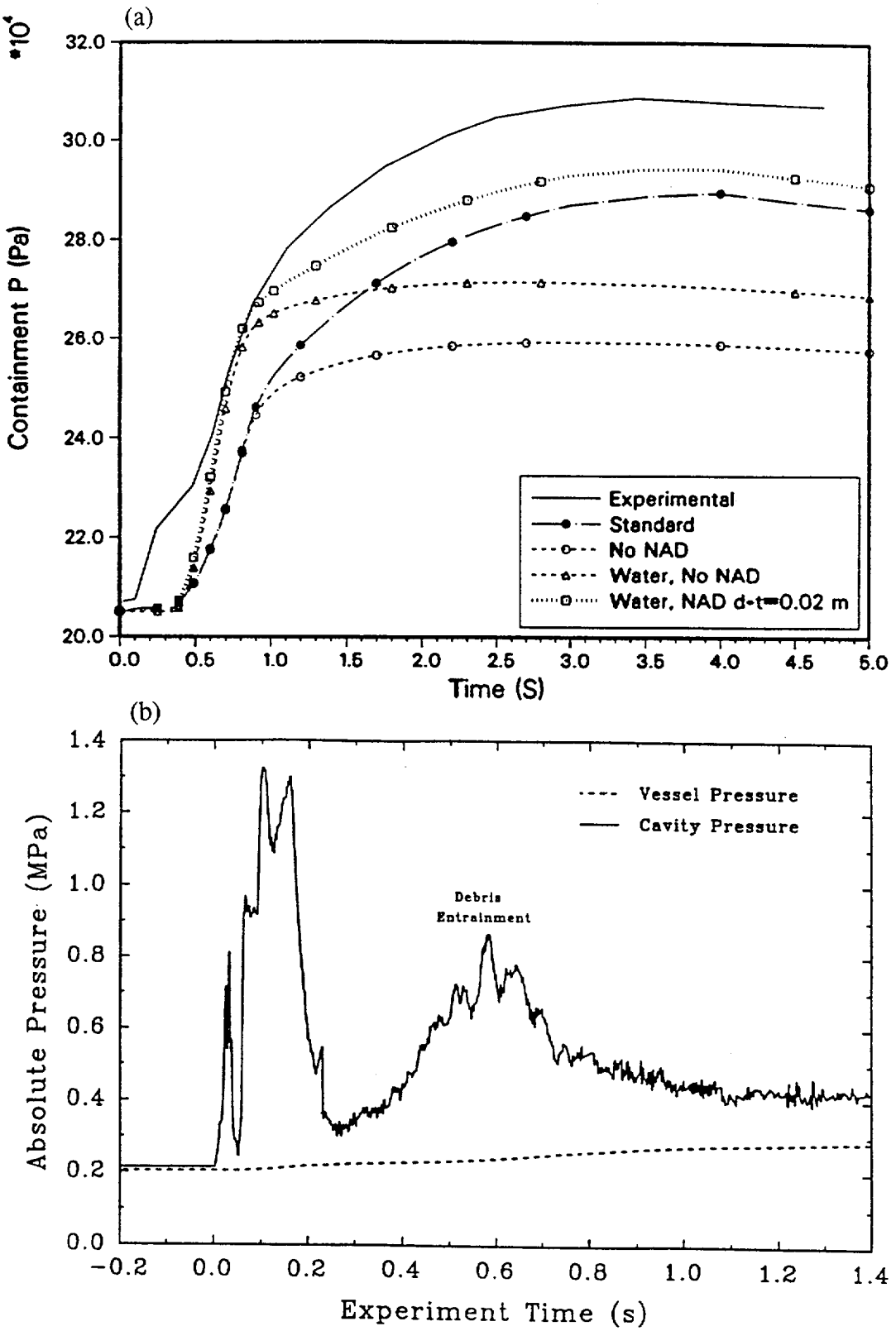

Figure 6.5-5. (a) Experimental and calculated dome pressure-time histories and (b) experimental cavity pressurization histories for the SNL/IET-5 experiment.

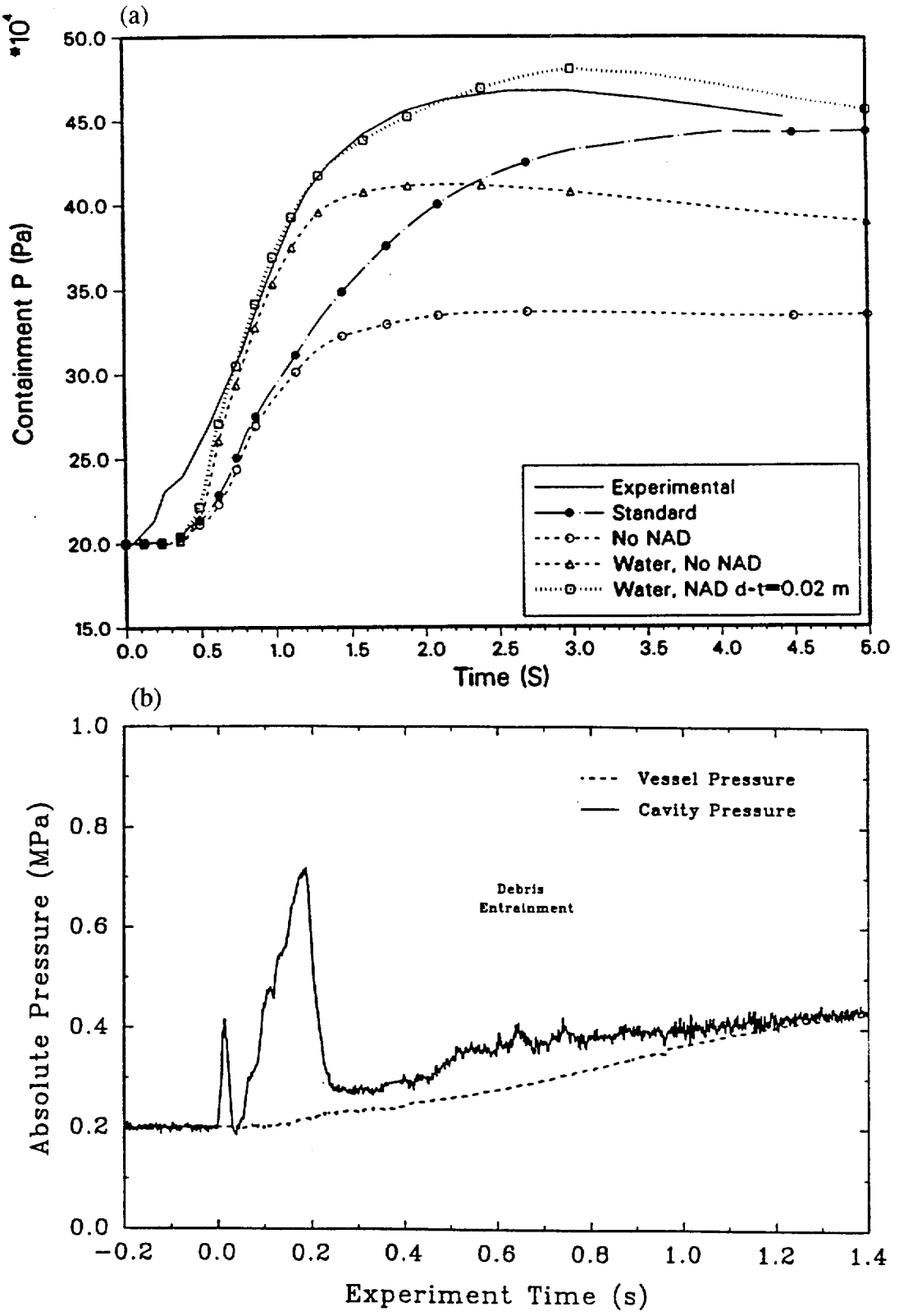

Figure 6.5-6. (a) Experimental and calculated dome pressure-time histories and (b) experimental cavity pressurization histories for the SNL/IET-7 experiment.

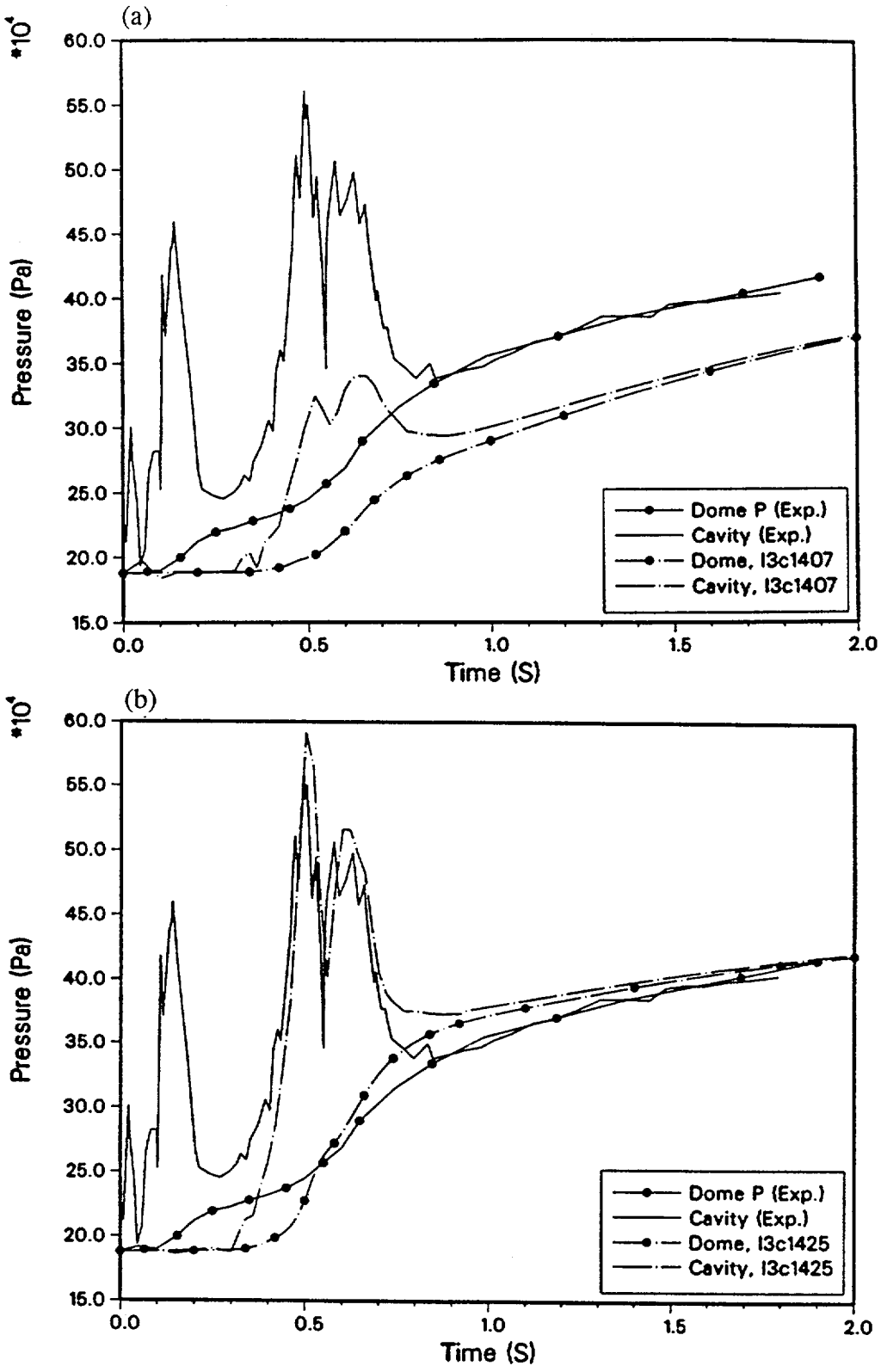

Figure 6.5-7. SNL/IET-3 experimental and calculated cavity pressurization histories, with calculations for (a) the standard input prescription and (b) case with co-dispersed water and nonairborne debris with d_t 0.02 m.

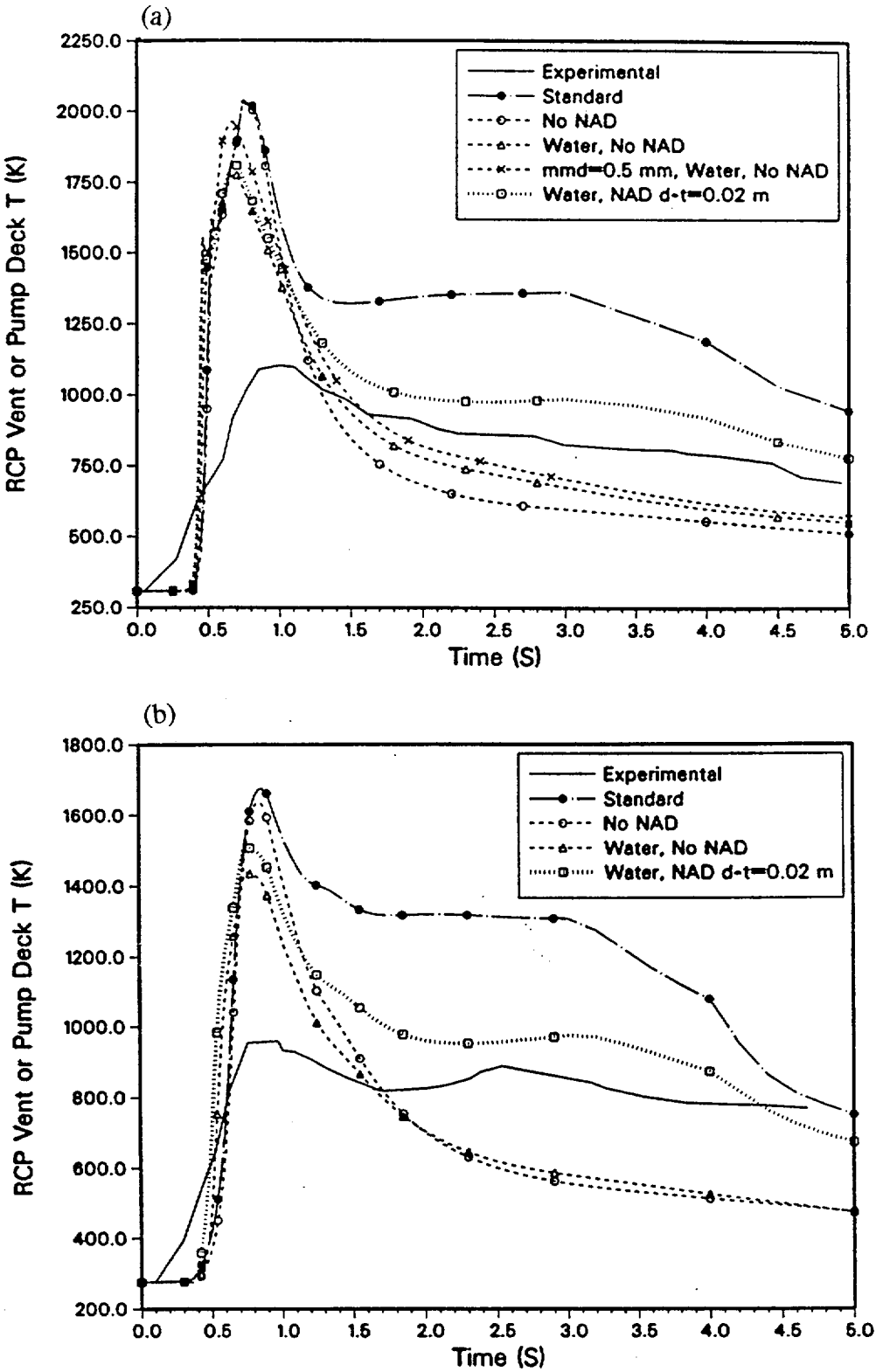

Figure 6.5-8. Comparison of temperature-time histories calculated for the pump deck cell with the experimental temperature-time history at the RCP 1A vent for (a) the SNL/IET-6 and (b) SNL/IET-1R experiments.

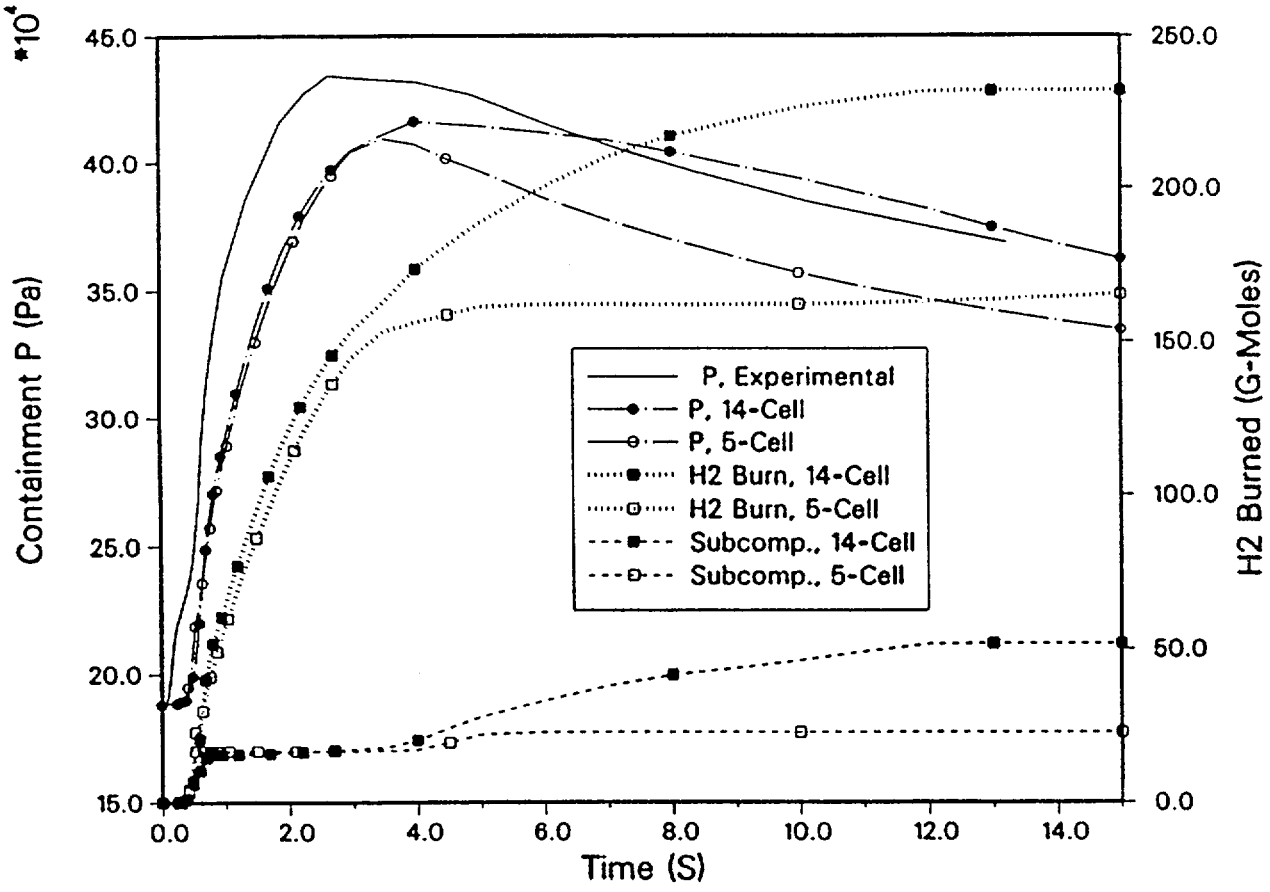

Figure 6.6-1. SNL/IET-3 experimental and calculated pressure-time histories and calculated cumulative hydrogen combustion, comparing calculations for 5-cell and 14-cell decks.

especially since it cannot even begin until the blowdown is almost complete. It is also a process that will not accelerate rapidly as the severity of a DCH event increases.

One cannot accept this explanation as proven, but the results obtained with the 14-cell deck are certainly suggestive. However, the pressure-time histories for these cases, as in Figure 6.6-1, also exhibited a delay in the onset of pressure decay that was not in complete agreement with experiment. Partly for this reason, the proposed explanation for the observed results is considered tentative. Although this late hydrogen combustion, if real, is irrelevant to the calculated ΔP, its explanation is not irrelevant to the interpretation of the experiment and this interpretation can have important implications for ΔP in other DCH scenarios. If the partial combustion of pre-existing hydrogen is interpreted as representing the onset of kinetics-controlled bulk reaction, a much more energetic response might require only a

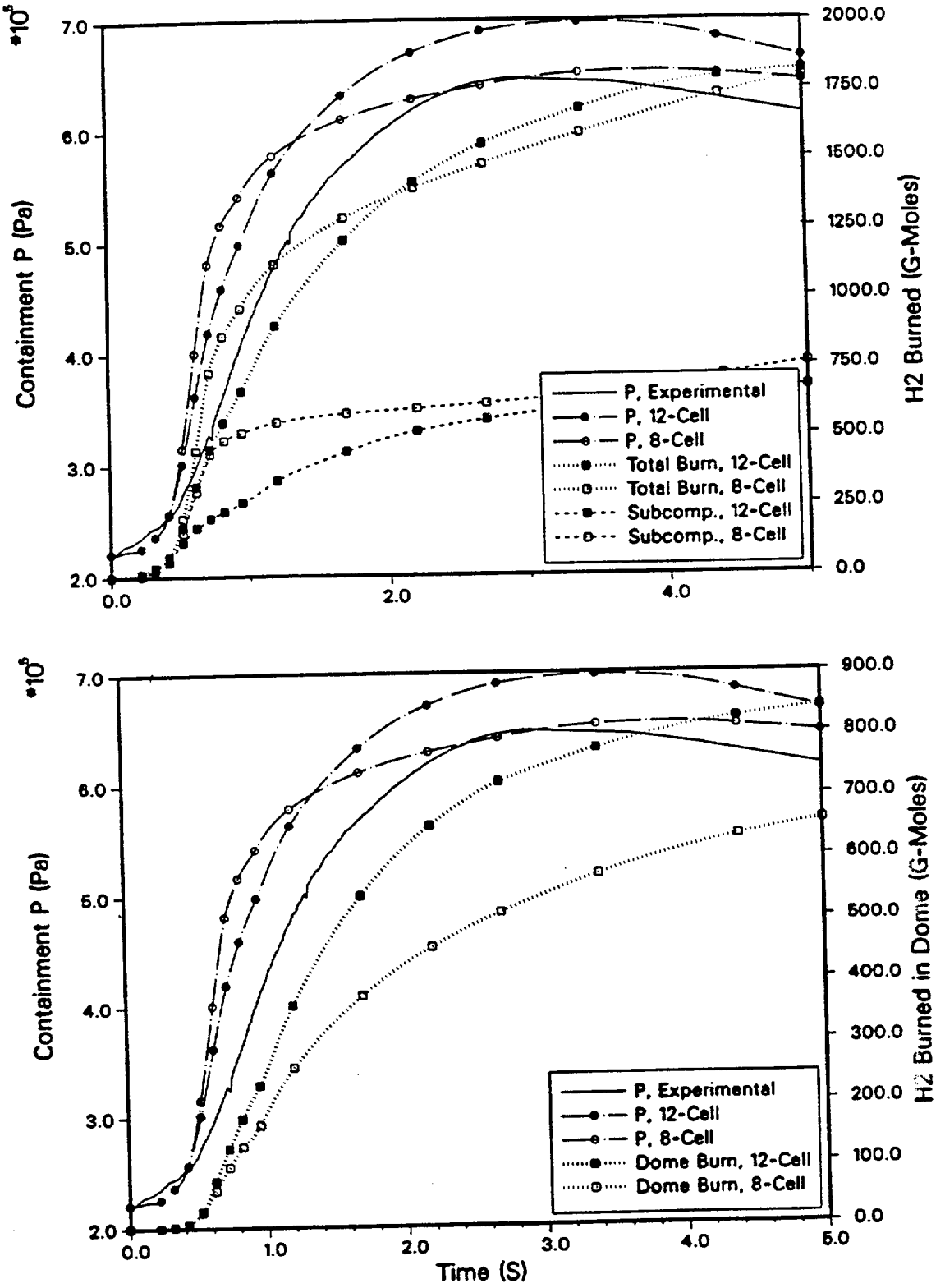

Figure 6.6-2. SNL/IET-11 experimental and calculated pressure-time histories and calculated hydrogen combustion histories, illustrating calculation sensitivity to nodalization.

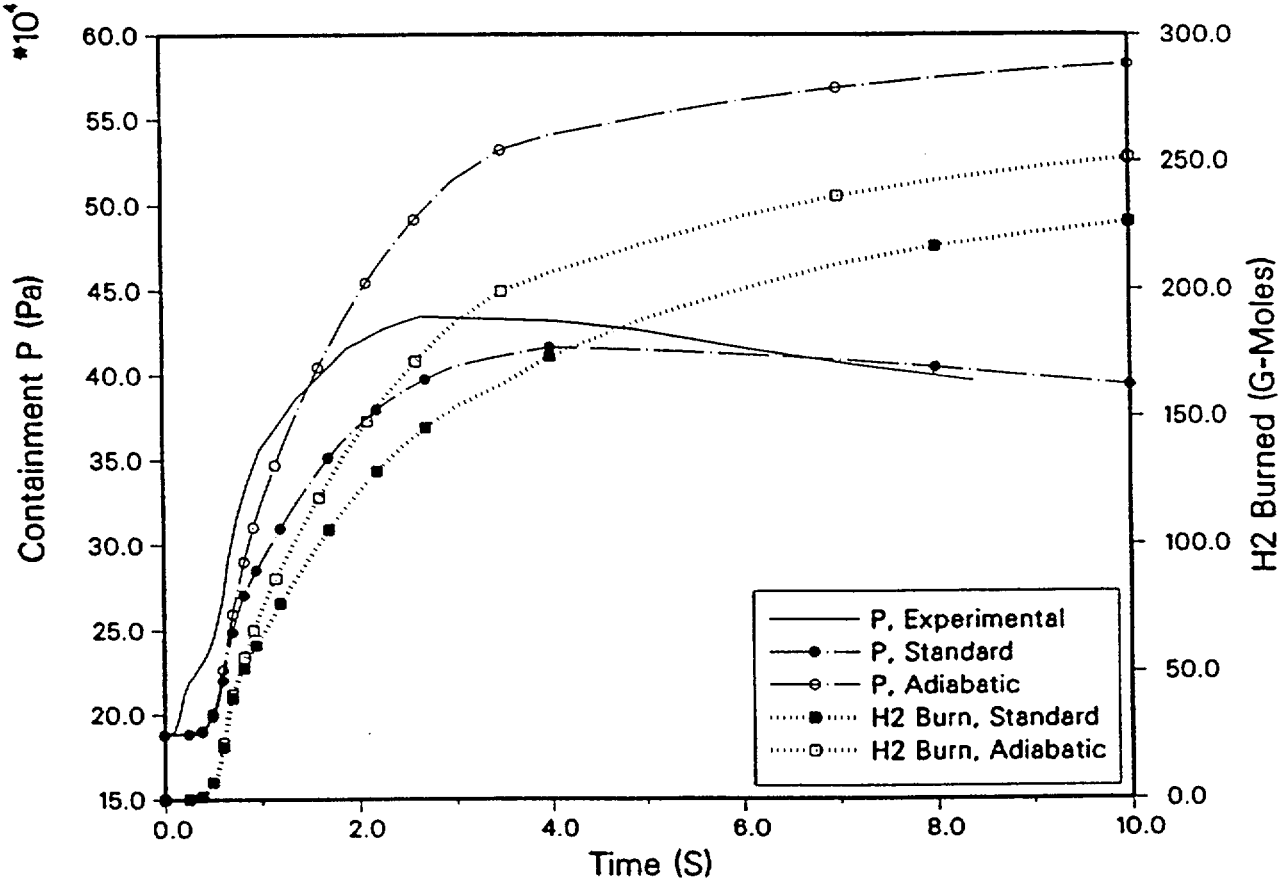

Figure 6.7-1. SNL/IET-3 experimental and calculated pressure-time histories, and calculated hydrogen combustion histories, illustrating mitigation by heat transfer and delayed hydrogen combustion in oxygen-starved subcompartments.

hydrogen could burn as soon as it is produced, the mitigation effects would no doubt be less; if it were not for the heat transfer effects, the delay in combustion would not matter. (There also may be some DCH-produced hydrogen that never does burn; hence the addition of "incomplete combustion" to the description.)

Unlike the situation with trapping, there is no experimental measurement against which one can directly check the calculated mitigation due to heat transfer, since no measurements of total heat transfer from atmosphere to structure during the event are available. Hence additional checking of the mitigation calculation seemed warranted. The first check involved performing some sensitivity studies on the heat transfer rates, and the second involved a simplified analytical calculation of the magnitude of the mitigation to be expected.

Figure 6.9-1 shows that the error in the blowdown, though not large, is larger than the degree of mismatch between the experimental and calculated blowdown curves that is normally achieved in this work. Since correcting the error had only a small effect, it follows that the degree of agreement between the experimental and calculated blowdown curves normally achieved is adequate to avoid significant error.

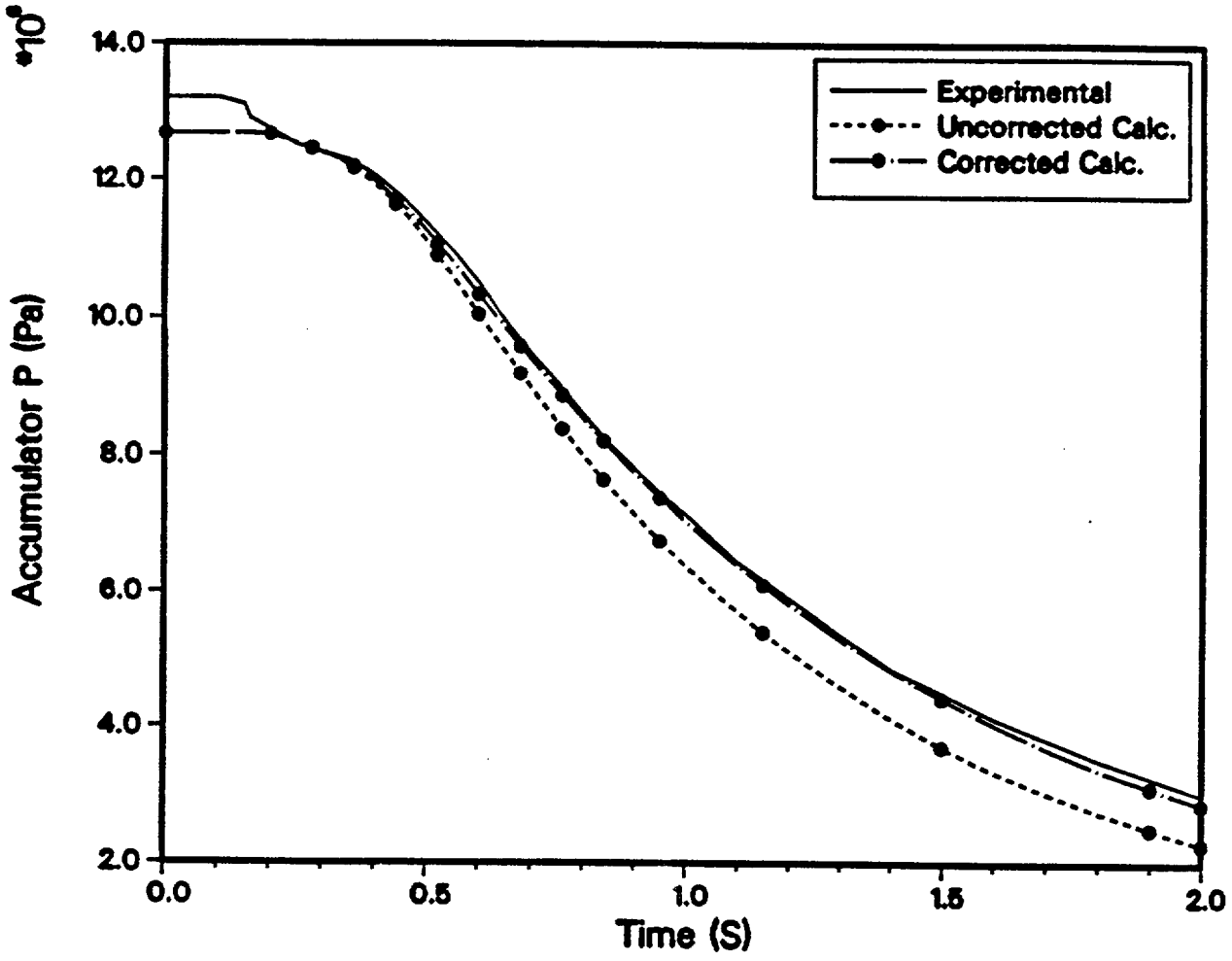

Figure 6.9-1. Calculated and experimental accumulator blowdown curves for SNL/IET-11, used to investigate sensitivity to errors in matching the experimental blowdown.

#2

APPENDICES for SAND 94-1174, "Assessment of the CONTAIN Direct Containment Heating (DCH) Model: Analyses of DCH Integral Experiments," Sandia National Laboratories, DRAFT dated November 10, 1996.

Appendix A

Experimental Configurations and CONTAIN Nodalizations

This Appendix provides some information on the experimental configurations in addition to what was presented in Section 2.1 of the main report, and summarizes the nodalization used in the CONTAIN analyses of these experiments. Experiments which were not analyzed with CONTAIN are not discussed here. The experimental reports cited in Section 2.1 may be consulted for additional details on the experiments. Except for the CONTAIN nodalization diagrams, the figures in this Appendix are taken from the experimental reports.

A.1 SNL Limited Flight Path (SNL/LFP) Experiments

The LFP experiments were conducted in the Surtsey facility at SNL. The facility is pictured in Figure A.1-1. The Surtsey free volume is about 103 m^3, when not reduced by internal structure. The steam accumulator and melt generator are included in the figure, below and to the left of the Surtsey vessel itself. The high pressure steam expelled the melt into the 1/10-scale model of the Surry reactor cavity, which is connected to the Surtsey vessel via a vertical chute. The cutaway opening in the Surtsey vessel shows the concrete slab used to limit the flight path at the nominal 2 meter position. Dashed lines also indicate the nominal 1 meter and 8 meter positions of the concrete slab.

The steam accumulator, melt generator, and reactor cavity are all located outside the Surtsey vessel itself. The same is true of all the experiments performed in Surtsey that will be considered here.

The concrete slab configuration is shown in more detail to the left of the main figure. There is a downward facing metal lip that limits horizontal flight after the debris strikes the underside of the slab. There is, however, ample space for gas to flow around the periphery of the slab and into the upper part of Surtsey.

When the slab is at the nominal 1 m or 2 m position, most of the Surtsey volume is above the slab and the containment geometry is characterized as being compartmentalized. In one experiment (LFP-8A), the slab was at the nominal 8 m level. About 75% of the total volume is then below the slab, and this experiment is categorized as being an open-geometry experiment.

The CONTAIN nodalization used to analyze the SNL/LFP tests is diagrammed in Figure A.1-2. A relatively simple 5-cell representation was used. Cells 1 and 2 represented the steam accumulator and the melt generator, respectively. Separate cells were used to model the accumulator and the melt generator because the flow resistance of the pipe connecting them was not negligible when the melt generator orifice was relatively large, and failure to model this resistance would result in too rapid a blowdown in some of the experiments.

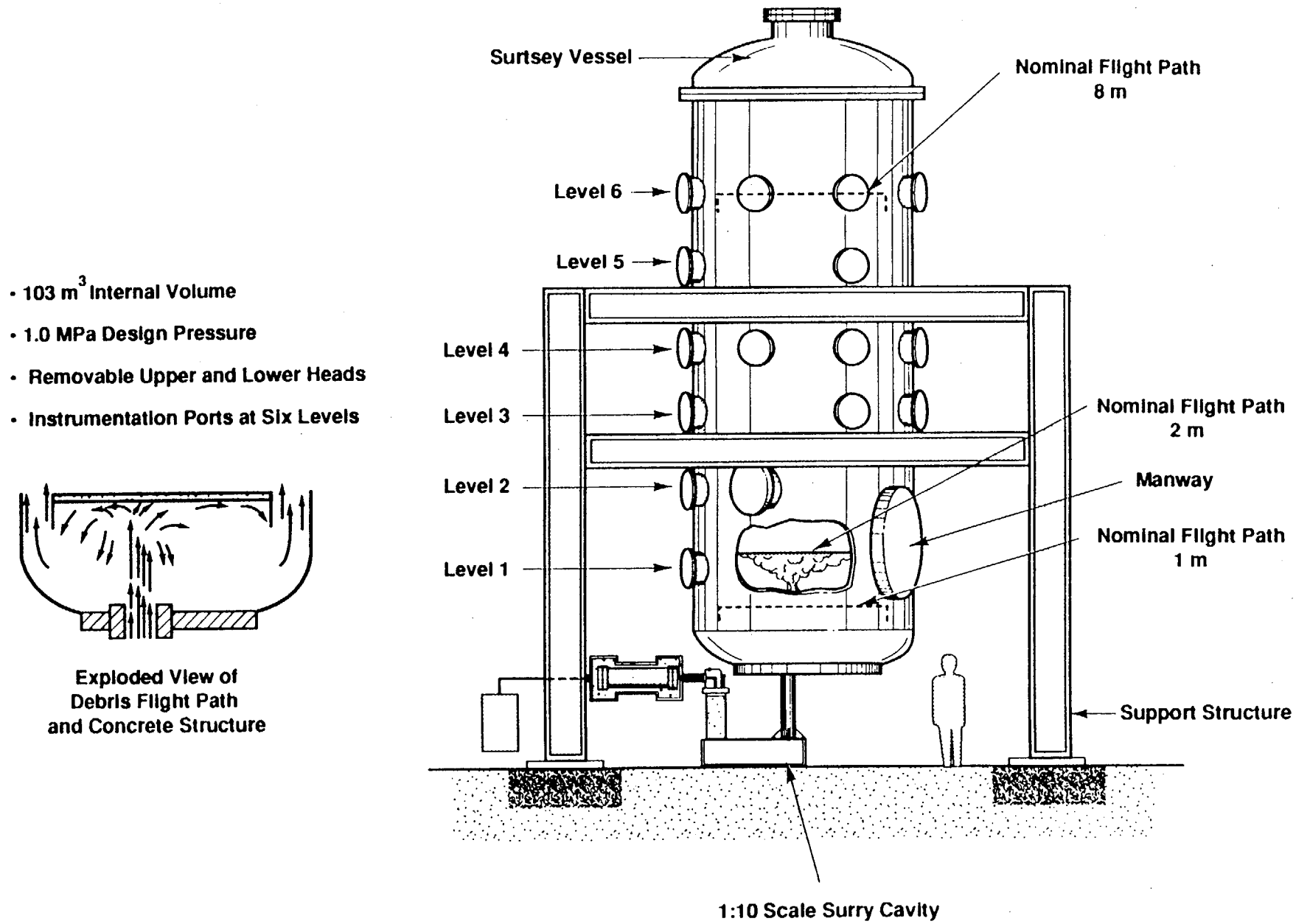

Figure A.1-1. Experimental configuration used in the SNL/LFP experiments showing the steam accumulator, melt generator, cavity, and Surtsey vessel, including the concrete slab that limited the flight path.

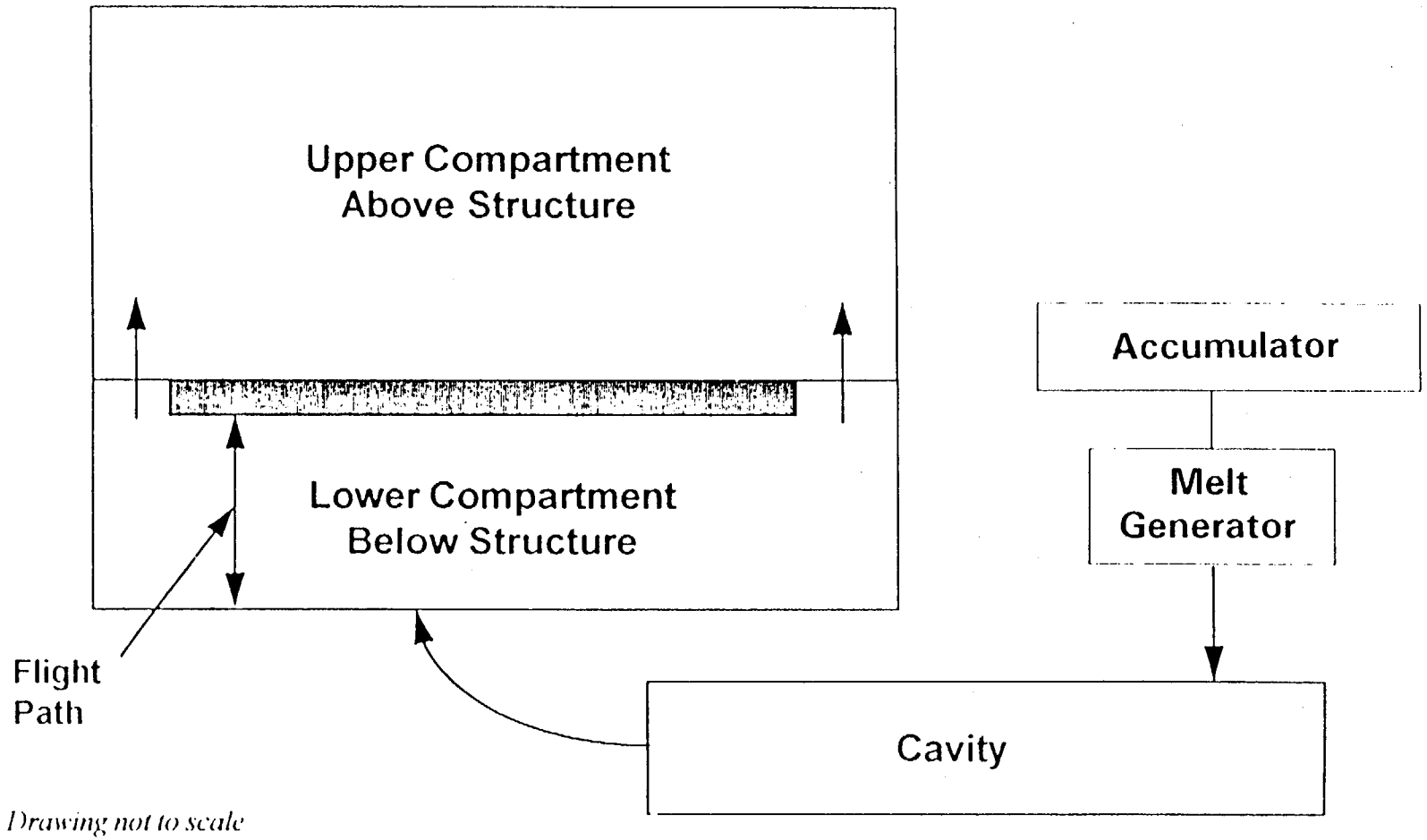

Figure A.1-2. CONTAIN nodalization for the analysis of the SNL/LFP and SNL/WC experiments.

Cell 3 represented the cavity cell, Cell 4 represented that part of the Surtsey volume which was below the concrete slab, and Cell 5 represented the volume which was above the slab. This same configuration was used for all the LFP experiments, with the volumes and structure areas of Cells 4 and 5 being adjusted to reflect the position of the slab in any given experiment.

A.2 SNL Wet Cavity (SNL/WC) Experiments

The experimental configuration for the WC experiments was similar to that of the LFP series except that a 1/10-scale model of the Zion cavity was used instead of the Surry cavity. The accumulator, melt generator, and cavity configuration and the connection to Surtsey are illustrated in Figure A.2-1. The cavity is joined at the floor with a sloping chute, with no vertical ledge or other obstruction to prevent debris flowing along the floor from entering the chute. This configuration is thought to favor relatively easy dispersal of debris from the cavity. Note that, in the experiment, there is a bend in the chute, with the upper part being vertical. In the Zion NPP, the chute continues at an angle until it enters the basement of the containment building; there is no vertical section.

In all three of the WC experiments, the concrete slab was at the nominal 8 m position, as in LFP-8A. All three of the experiments are therefore categorized as being "open-geometry" experiments.

The nodalization used to represent these experiments in the CONTAIN code was essentially the same as was used to represent the LFP experiments.

A.3 SNL Integral Effects Tests, Zion Geometry (SNL/IET Zion)

These experiments were performed in the Surtsey facility at 1/10-scale. In addition to using a scaled model of the Zion cavity, scale models of the Zion lower containment compartments and structures were included. Figure A.3-1 presents a cross section of the experimental configuration which includes the chute connecting the cavity to Surtsey, although the cavity itself is not included in the figure. Figure A.3-2 provides an isometric cutaway view of the experimental configuration. The circled numbers on both figures mark the locations of various instruments used to take data in the experiment; see Reference All94b for details. In the description below, these numbers are used to reference various locations.

In the SNL/IET experiments, the chute continues at an angle all the way to the containment basement as it does in the Zion NPP; there is no vertical section as in the WC experiments. However, the length of the chute is about 2.7 times as great as would correspond to a 1/10-scale model of the actual Zion NPP. This overscaling was imposed by the geometrical constraint that the chute had to extend from the cavity located outside Surtsey to the false floor in Surtsey, which represents the Zion containment basement floor. This

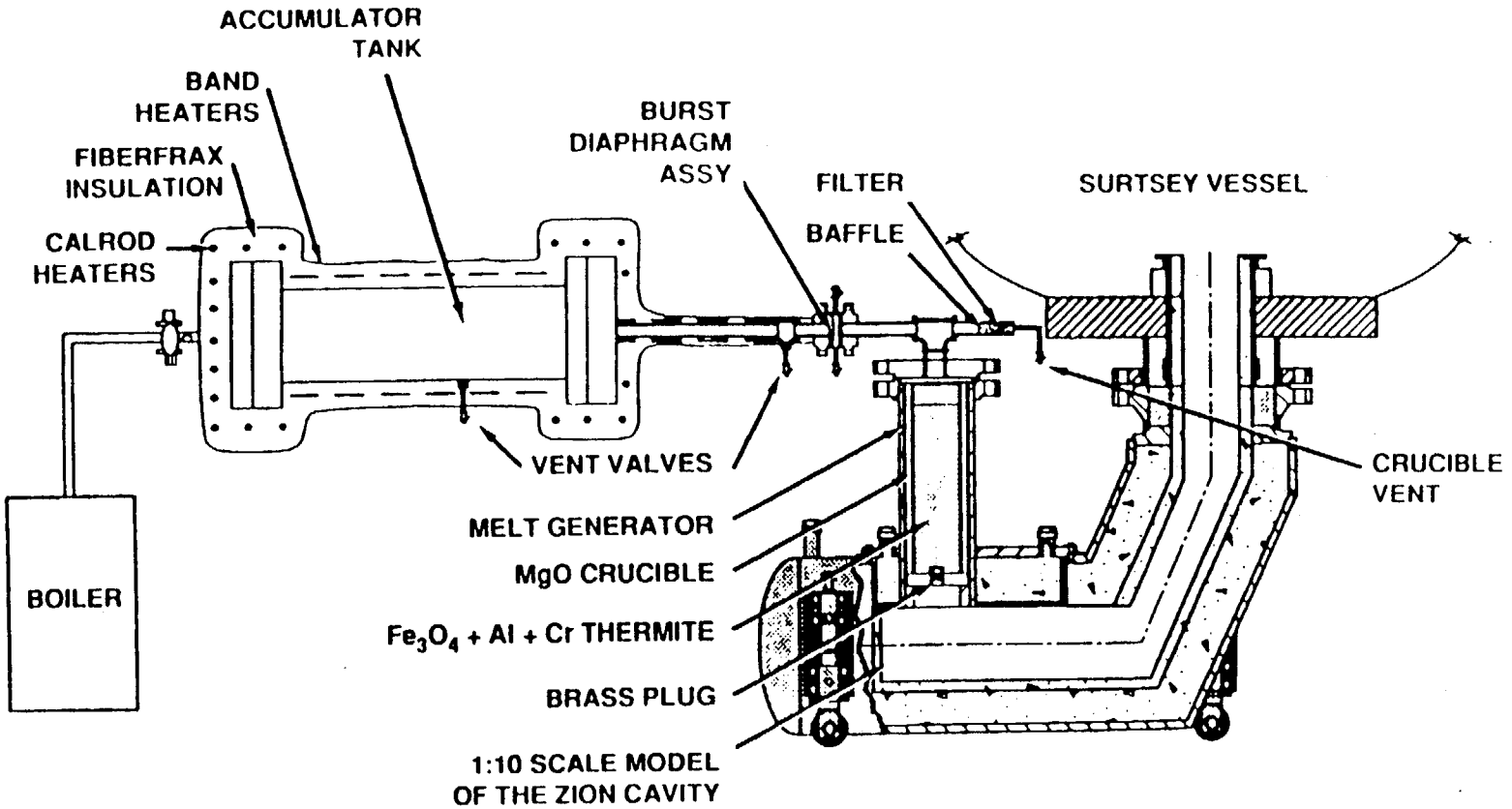

Figure A.2-1. Experimental apparatus for melt generation and the scaled Zion cavity used in the SNL/WC experiments.

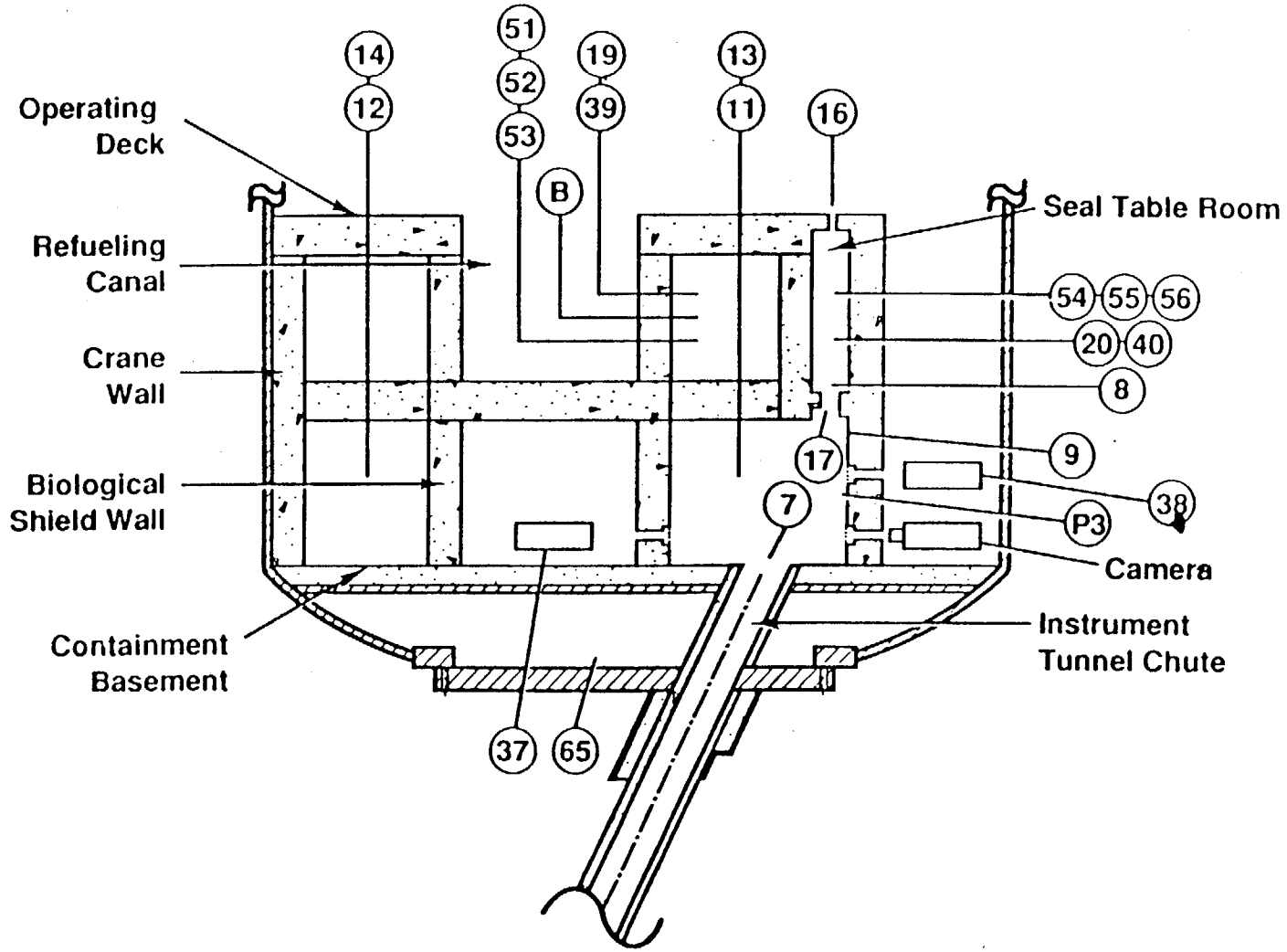

Figure A.3-1. Vertical cross section through the subcompartment structures inside the Surtsey vessel used in the SNL/IET Zion experiments.

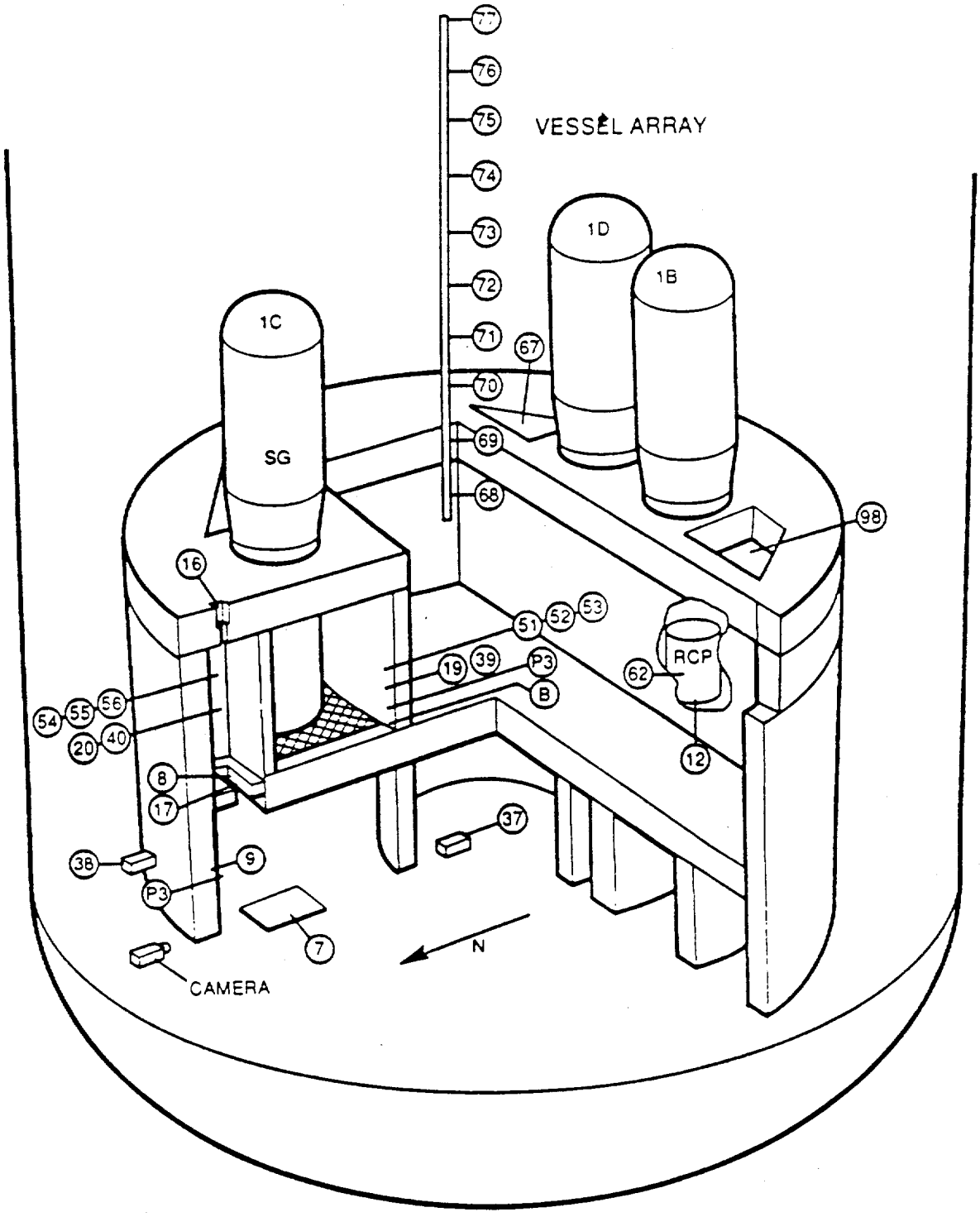

Figure A.3-2. Isometric view of the SNL/IET Zion subcompartment structures.

false floor added to the length of the chute required. The false floor was needed because the actual bottom of Surtsey is rounded and could not have accommodated the scaled Zion structures.

The space inside the biological shield wall is not connected to the remainder of Surtsey and is thus not part of the free volume of the experiment. The same is true of the volume below the false floor.

The 14-cell CONTAIN nodalization used to analyze these experiments is diagrammed in Figure A.3-3. Cells 1 and 2 represent the accumulator and melt generator, respectively, and Cell 3 is the reactor cavity. The chute is modeled separately (Cell 4). The part of the basement where the chute enters is Cell 5 (location 7 in Figures A.3-1 and A.3-2, "Basement B" in Figure A.3-3). Cell 6 (Basement C) would be located adjacent to Cell 5 in front of the plane of the paper in Figure A.3-1, and clockwise from Cell 5 in Figure A.3-2. Cell 7 (Basement A) was located adjacent to Cell 5 in the opposite direction from Cell 6; i.e., behind the plane of the paper in Figure A.3-1 and in the counterclockwise direction in Figure A.3-2. The remainder of the basement, including all the far side from the chute exit, was made up by Cell 9 (Basement D).

There are no well-defined partitions marking the boundaries of the four cells making up the basement. The areas of the flow paths connecting these cells are almost as large as the mean cross sectional areas of the cells themselves. The principal purpose of subdividing the basement in this fashion was in order to conform to the rule suggested in Section 7.2 that, in the vicinity of the chute exit, the cell dimensions should be the same order of magnitude as the unobstructed flight paths of debris. The region of the basement farther from the cavity exit was lumped together as a single volume (Cell 9), which includes over 50% of the total basement volume, in the expectation that this region would not play a large role in the debris transport process.

The seal table room (Cell 10 in the CONTAIN deck) is the small compartment above location 17 in Figure A.3-1, just inside the crane wall. The entrance of the seal table room is approximately in line with the chute and, in the experiment, substantial debris enters the seal table room due to its momentum. Some of this debris carries on through the small opening in the top of the seal table room into the dome. This momentum-driven transport is a process the CONTAIN code cannot model.

The remainder of the subcompartment volume between the elevation of the refueling canal floor and the operating floor elevation is the pump deck level. Cell 11 represents the part on the same side of the refueling canal as the chute exit ("near side"), and the far side is Cell 12. There are a total of four vent spaces through the operating floor from the pump deck level to the dome, two on the far side (locations 67 and 98 in Figure A.3-2) and two on the near side. These vents are above the reactor coolant pumps (RCPs) and are referred to as the RCP vent spaces.

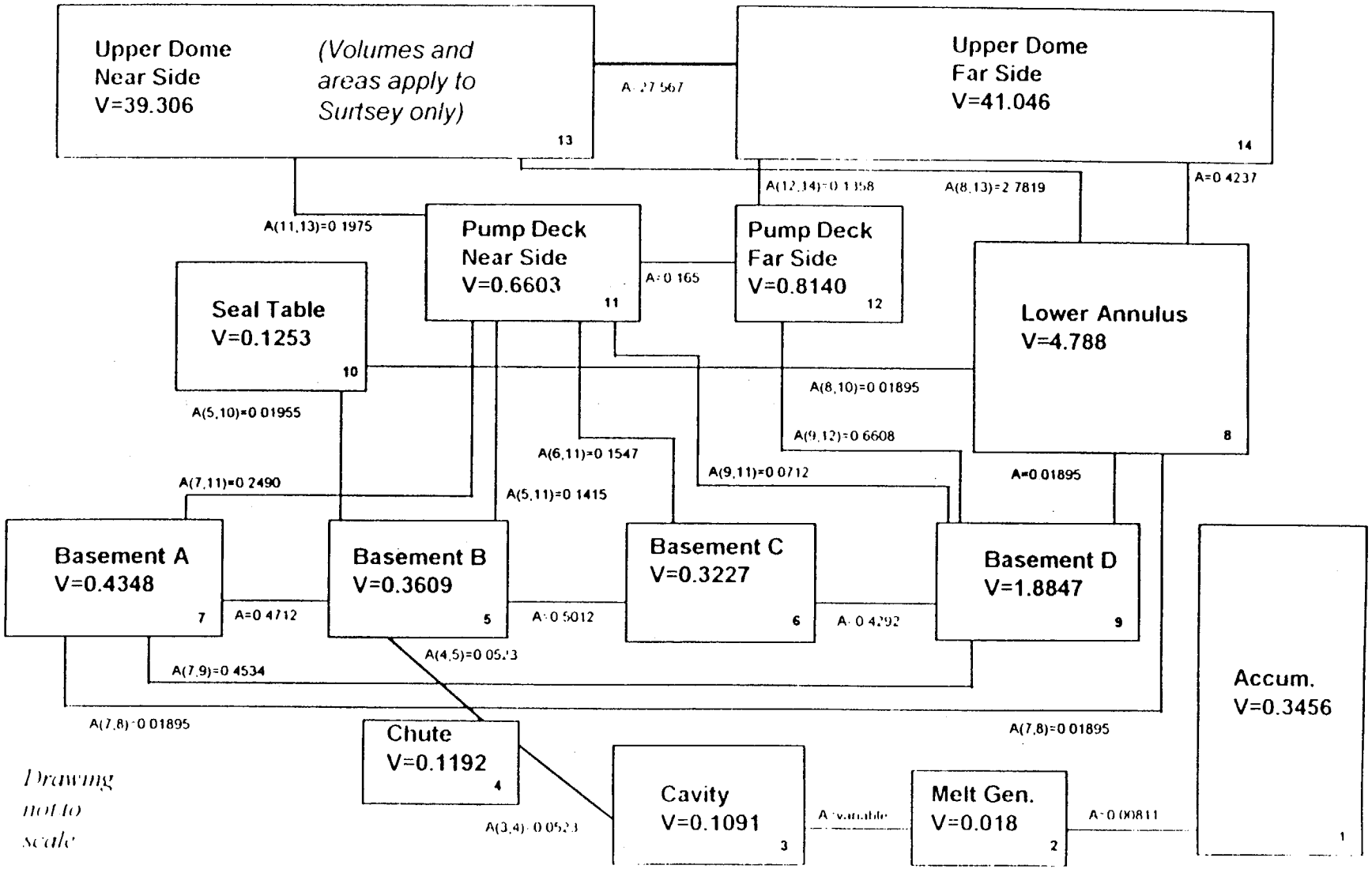

Figure A.3-3. CONTAIN 14-Cell nodalization of the SNL/IET Zion experimental configuration.

The region outside the subcompartments is represented by Cells 8, 13, and 14. Cell 8 is the region between the crane wall and the Surtsey shell ("Lower Annulus" in Figure A.3-3). Cells 13 and 14 divide the main dome volume, with Cell 13 representing the side nearer to the chute exit and Cell 14 representing the far side.

The main flow path from the chute exit to the dome is through the cells representing the near side of the basement, up through various openings into the pump deck level, and thence through the RCP vent spaces. There are also smaller flow paths through doors in the crane wall into the annulus. In the CONTAIN calculation, flows through the seal table room are small due to the small size of the openings and the inability of the code to model the momentum-driven transport processes.

The flow paths between the four basement cells were divided into an upper half and a lower half in order to permit a representation of countercurrent flows. The same was done for the flow path representing the interface between the two dome cells. These refinements would not have an important effect upon the maximum pressure calculated, but could have an effect upon the late-time hydrogen combustion behavior, after the accumulator blowdown is complete.

The various flow path areas, structure areas, and cell volumes used in the 14-cell SNL/IET Zion deck were derived from detailed drawings of the experimental configuration. The representation of these features in the 14-cell deck is quite detailed. The deck itself (specifically, for the standard input prescription analysis of the SNL/IET-6 experiment) is reproduced in Reference Was94.

5-Cell Deck. In early phases of this study, a limited amount of use was made of a 5-cell representation of the SNL/IET experiments. It was derived by collapsing the 14-cell deck. In the 5-cell representation, Cells 1 and 2 represented the accumulator and the melt generator as before, while the cavity and chute cells were combined into a single cell (Cell 3). Cell 4 represent the subcompartment volume and was defined by combining the structures and volumes of Cells 5-7 and 9-12 of the 14-cell deck. Cell 5 represented all volumes outside the subcompartments and was derived by combining Cells 8, 13, and 14 of the 14-cell deck. Two flow paths between the subcompartments and the dome were modeled. One represented the four RCP vent spaces and the other represented the doors in the crane wall.

A.4 ANL Integral Effects Tests, Zion Geometry (ANL/IET Zion)

The ANL/IET Zion experiments were performed in the COREXIT Facility at ANL. The test configuration was designed to provide a scaled counterpart to the SNL/IET Zion tests. The tests are commonly referred to as being 1/40-scale, although the actual linear scale factor is 0.0255. In the CONTAIN deck for analyzing these experiments, the representation for the cavity, chute, and all subcompartment cells was derived from the 14-cell SNL/IET Zion deck by applying the linear scale factor of 0.255 to all dimensions. The accumulator conditions were defined to provide the correct experimental pressure, temperature, and

number of moles of blowdown steam for each experiment. Separate cells were not used for the accumulator and the melt generator because the hole size was relatively small in these experiments and the flow resistance between the accumulator and the melt generator had little effect. The cells representing the main dome volume differed somewhat from being scaled replicas of the Surtsey dome cells, since the COREXIT facility has a higher aspect ratio than does Surtsey and the CONTAIN representation was modified to reflect this difference.

A.5 SNL Integral Effects Tests, Surry Geometry (SNL/IET Surry)

Figures A.5-1 and A.5-2 provide, respectively, a vertical cross section and a cutaway isometric view of the CTTF Surry geometry test configuration. Circled numbers in Figure A.5-2 mark instrument locations and they are used in the following discussion to reference specific locations. Figure A.5-3 diagrams the 8-cell CONTAIN nodalization that was used in the large majority of the analyses of these experiments.

The melt generator and accumulator were located inside the CTTF facility and the location of the melt generator was in the proper position to represent the RPV. Hence the annular gap and the reflective insulation surrounding the vessel could be modeled, and this was done in the IET-11 experiment. The annular gap around the melt generator was completely closed off in IET-10, and was partially blocked in IET-9.

In the CONTAIN representation, Cells 1 and 2 represent the accumulator and the melt generator, respectively. In early exploratory analyses for IET-9, the cavity and instrument tunnel were represented by separate cells, but these were combined into a single cell (Cell 4) and Cell 3 is a dummy cell in the representation actually used in this work. Cell 5 is the residual heat removal (RHR) platform and Cell 6 represents the seal table room. Cell 7 represents the basement region of the containment, Cell 8 represents the annulus between the crane wall and the CTTF shell, and Cell 9 is the open volume of the containment dome.

In the CONTAIN analysis, the main flow path was from the cavity to the RHR platform and thence to both the annulus and the basement. Most flow to the dome would therefore be from either the annulus cell or the basement cell. Note that, in Figures A.5-1 and A.3-2, the part of the crane wall annulus directly above the openings from the RHR platform is blocked by an extension of the seal table room floor structure, called the seal table room ledge, that extends out to the CTTF shell. Hence, debris and gas exiting the RHR platform and striking the CTTF shell cannot move directly upward to the dome. In CONTAIN, the only effect of this ledge that can be represented is its effect upon the total flow path area from the annulus to the dome. This effect is trivial, because the ledge subtends only a very small fraction of the azimuthal extent of the annulus (Figure A.5-2). Since the ledge directs the momentum of debris and gas horizontally (or downward), the ledge may have a more important influence in reality, due to momentum-controlled effects that CONTAIN cannot model.

Because the flow enters the annulus at the RHR platform level, and because the flow cannot go directly upward at this point, the gravitational fall height, Lgft, to be used for the

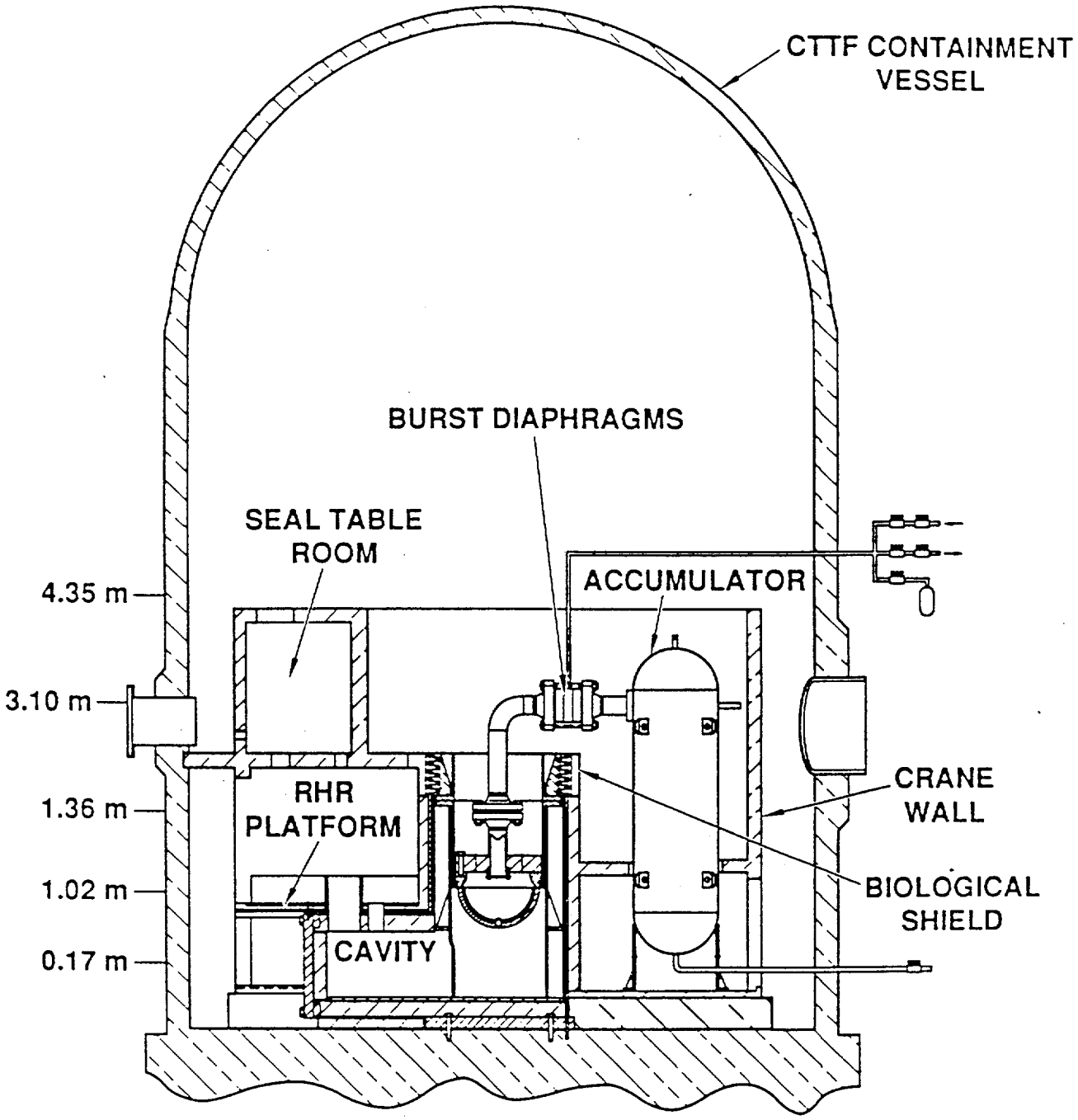

Figure A.5-1. Vertical cross section of the experimental configuration used in the SNL/IET Surry experiments performed in the CTTF.

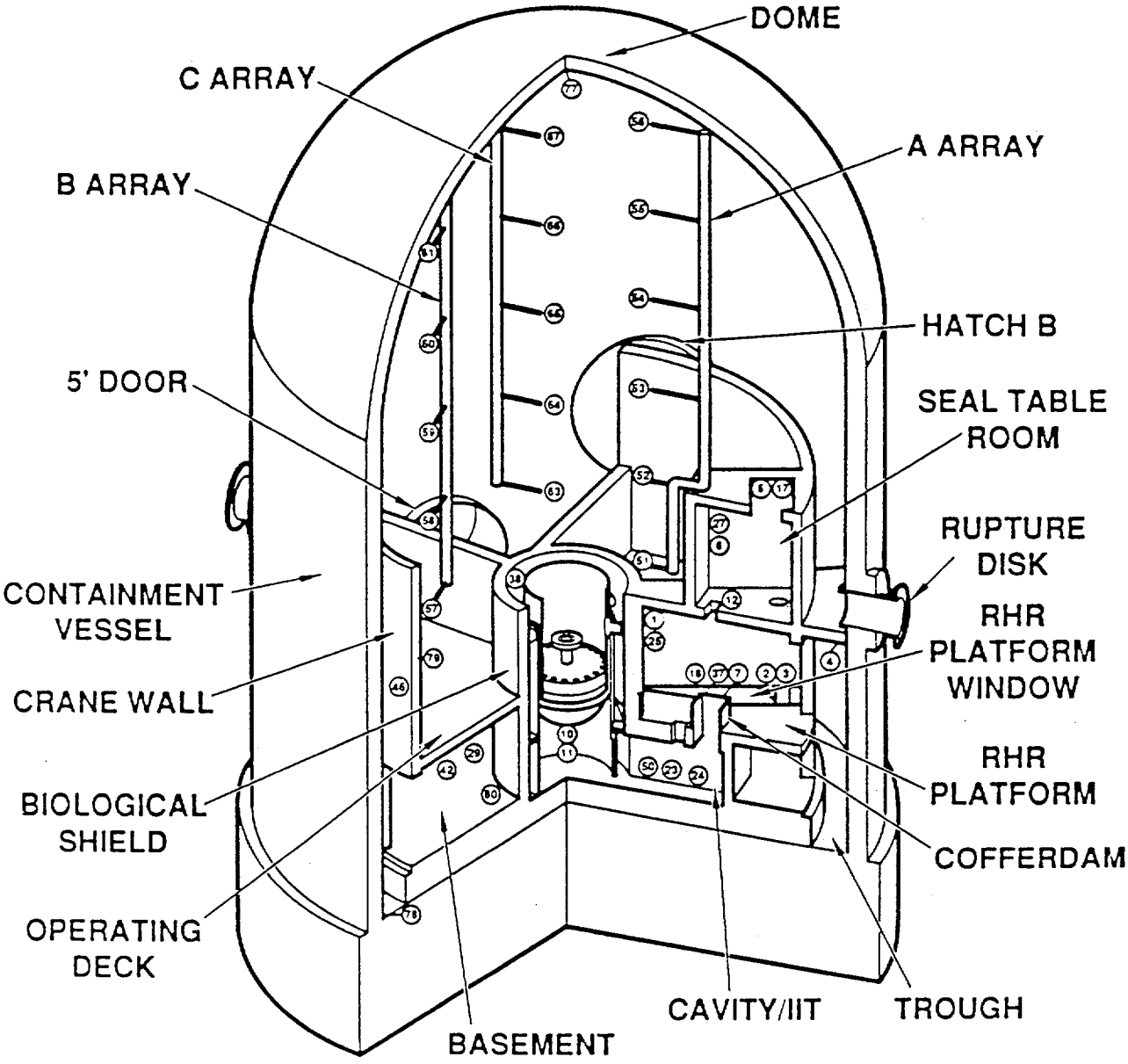

Figure A.5-2. Isometric view of the experimental configuration used in the SNL/IET Surry experiments performed in the CTTF.

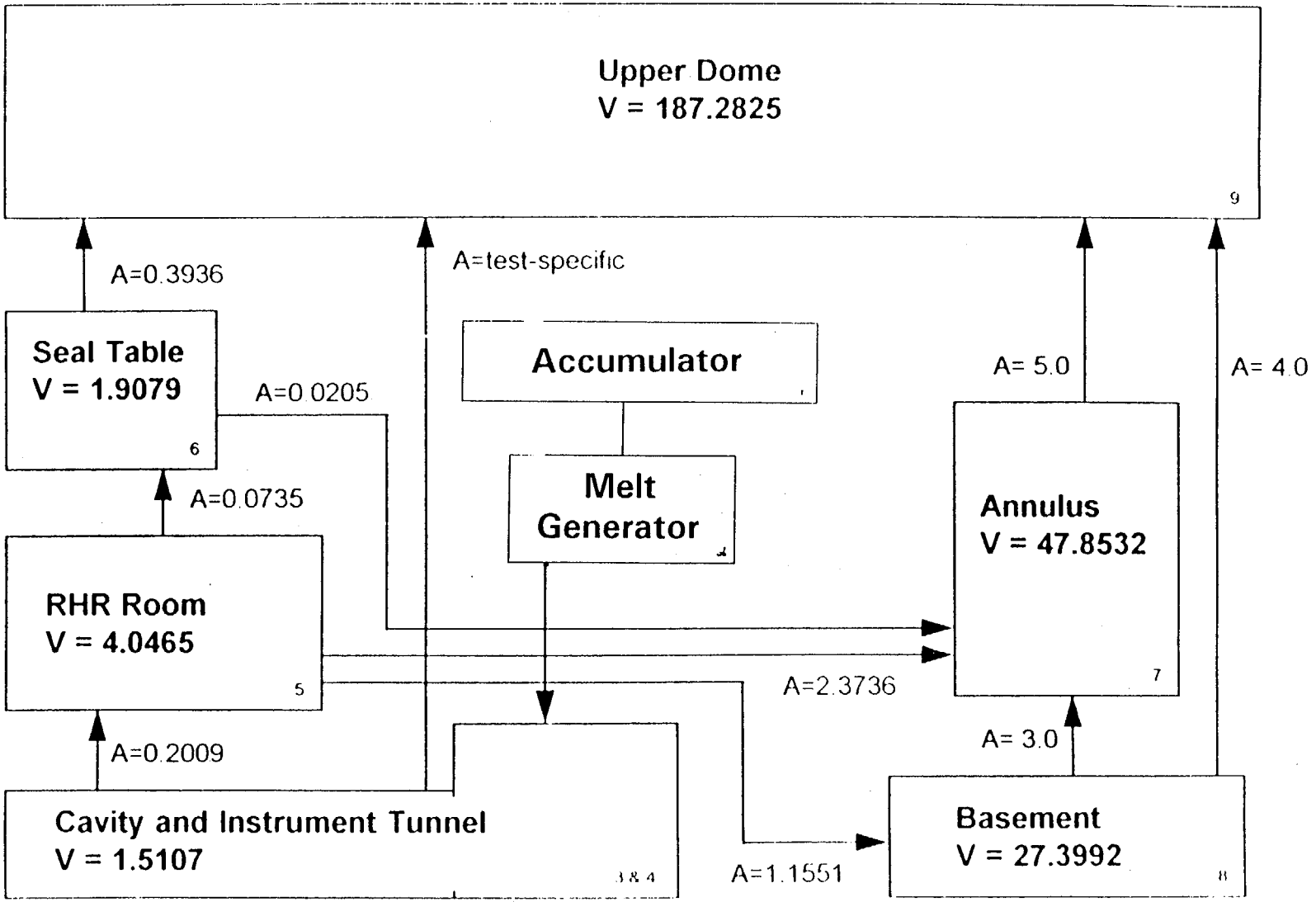

Drawing not to scale

Figure A.5-3. CONTAIN 8-Cell nodalization used to represent the SNL/IET Surry experiments performed in the CTTF.

trapping model was set equal to half the cell height in the annulus cell. Normally, the standard input prescription would call for Lgft to be set equal to the full cell height.

The exit from the cavity (location 37 in Figure A.5-2) is at least partially aligned with the opening from the RHR platform to the seal table room (location 12). Thus momentum-controlled transport of debris into the seal table room is possible whenever the seal table is not in place. In IET-9, the seal table was not modeled in the experiment and this path was therefore open. In IET-10 and IET-11 the seal table was modeled in the experiment, but ablation by molten debris partially opened the entrance to the seal table room.

The entrance to the seal table room, even if fully open, is much smaller than flow paths from the RHR platform to the annulus and to the basement. Hence, CONTAIN would normally calculate very little gas flow or debris transport to the seal table room, since it cannot model the momentum-driven transport of debris through the aligned openings. In an attempt to simulate this effect, a fictitious flow path was defined directly connecting the cavity (Cell 4) to the seal table room (Cell 6); see Figure A.5-3. The area of this flow path was derived by estimating the fraction of the cavity exit opening which is subtended by the seal table room opening when the latter is unobstructed. The same representation was used for all three experiments; that is, this flow path was not reduced in IET-10 and IET-11 in order to take into account the fact that the seal table was not totally removed.

In setting up the 8-cell representation of the Surry IET experiments, a number of simplifications and approximations were made in representing the structures and the flow paths. These representations were not nearly as detailed as those used in the 14-cell Zion IET decks (which had been quite time-consuming to develop).

12-Cell Surry Deck. In order to investigate sensitivity to certain nodalization issues (see Section 6.6.3 of the main report), some analyses were made using a 12-cell representation of the Surry experimental geometry. In this representation, the annulus cell was divided into four quadrants, one of which was located at the RHR room exit, one at the opposite side of the containment, and two quadrants on either side of the RHR room quadrant. The basement cell was divided into two halves, one on the RHR room side and one on the opposite side of the containment. For the most part, the various flow paths and structures of the original annulus and basement cells were simply apportioned among the subdivided versions, without taking into account the various asymmetries that actually exist in the experimental configuration.

The various simplifications and approximations made concerning flow paths and structures in the 8-cell deck remain in the 12-cell deck. The principal purpose of the 12-cell deck was to investigate the implications for hydrogen combustion of CONTAIN's well-mixed assumption when applied to the annulus and basement volumes, since it was suspected that the shape of these volumes might invalidate this assumption. No effort was made to capture the level of detail represented by the Zion 14-cell deck.

A.6 Code Version

The large majority of all calculations reported in this work were performed on a developmental version of CONTAIN 1.2 that included all update sets up through C110z. A few calculations were performed with a version that included update sets through C110ad. These code versions did not include the so-called hybrid flow solver, which is now the default in CONTAIN 1.2. Comparison calculations run on the released version of CONTAIN 1.2 yielded differences $\leq 1\%$ in ΔP provided the decks were set up to reproduce the modeling of natural convection in the older code versions as closely as possible. This necessitated use of the old flow solver in the calculations performed with the released version of CONTAIN 1.2.

Reference

Was95. K. E. Washington, "Direct Containment Heating Models in the CONTAIN Code," SAND94-1073, Sandia National Laboratories, Albuquerque, NM, August 1995.

Appendix B

Contributions of Nonairborne Debris to DCH

As it was originally conceived, the nonairborne debris (NAD) concept was thought of as representing the interactions between blowdown steam and debris films on structures, much as the term "nonairborne debris" implies. It is now considered possible, even likely, that a complex variety of processes may be involved, especially in the Zion IET compartmentalized geometry (see Section 3.2.7 of the main report). However, it is still considered likely that debris films on structures do contribute significantly, and the development in this Appendix is based upon the debris film concept.

In Section B.1, an analytical model for the effects of debris films on structures is constructed and used to illustrate why these effects do merit consideration. In Section B.2, the model is extended to provide an *a priori* estimate of the trapped field diameter, d_t. Results are reasonably consistent with the value chosen on empirical grounds in the main report. This model for d_t is then used to develop the rule for varying the value of d_t as a function of facility scale. Possible implications for how d_t might be varied as a function of other DCH scenario parameters such as driving pressure and vessel failure size are also noted, although only the suggested scaling rule was used in the present work. In Section B.3, the effect of the cooling of debris films due to heat transfer to structures is briefly considered, and Section B.4 concludes with some additional discussion concerning use of the present model and possible improvements to the model.

Except for the scaling rule, the results in the main report do not depend in any way upon the development in this Appendix, which is offered for the purpose of establishing plausibility of the nonairborne debris concept, an order-of-magnitude evaluation of some of the phenomena involved, and some pointers as to how a more mechanistic model might be attempted if such is desired. A number of approximations will be made with less defense than would be appropriate for models that are actually to be included in the CONTAIN code. As for the scaling rule, the need for acknowledging large uncertainties in the treatment of nonairborne debris interactions has already been stressed in the main report, especially in Sections 7.7 and 7.8.

B.1 Plausibility Arguments for the Significance of Nonairborne Debris Interactions

It has traditionally been assumed that DCH is necessarily dominated by the interactions of dispersed, airborne particulate with the containment atmosphere and/or the blowdown steam, and that nonairborne debris could be neglected due to the much lower surface/volume ratio involved. As stated, this argument neglects the fact that the particulate debris may have a very short airborne residence time, while the nonairborne debris may be available for

interaction during most of the blowdown period. In any case, it is not argued that nonairborne debris interactions are effective competitors with the interactions of the airborne debris when the latter is available in significant quantities. Instead, the thesis is only that, once debris dispersal terminates and airborne debris is no longer available, the nonairborne interactions with the continuing flow of blowdown steam may make a significant additional contribution to DCH, a contribution which is neglected if only the airborne interactions are to be considered.

We address the problem using heat and mass transfer correlations similar to those used for interactions between containment structures and the atmosphere in the standard CONTAIN models for these processes (including non-DCH analyses). In a sense, the case for significant contributions from nonairborne debris is only the flip side of the case for significant mitigation due to heat transfer to those structures which are not coated with hot debris (Appendix C).

Depending upon the geometry and flow patterns, a number of correlations are available for the Nusselt number, Nu, for heat transfer [Bir60]. We consider here a subset of these correlations that can be at least approximately represented by the form

$$Nu = \beta Re_L^m Pr^{1/3}, \tag{B.1-1}$$

where β and m are constants, Re_L is the Reynolds number for gas flow across a structure surface of characteristic length L, and Pr is the Prandtl Number. The correlation used in the CONTAIN code for atmosphere-structure heat transfer under forced flow conditions is of this form, with $\beta = 0.037$ and $m = 0.8$ [Was91].

Using the heat/mass transfer analogy, a corresponding relation for the Sherwood Number, Sh, is obtained from which the gas-phase mass transfer coefficient, h, may be written

$$h = Sh\left(\frac{D_g}{L}\right) = \beta Re_L^m Sc^{1/3}\left(\frac{D_g}{L}\right), \tag{B.1-2}$$

where D_g is the binary diffusivity for hydrogen and steam, and Sc is the Schmidt Number. In the present instance, we are interested in steam reacting with hot metallic debris and we have therefore assumed that the dominant constituents of the atmosphere are steam and hydrogen. During a DCH event, this assumption is usually valid for the cavity and the subcompartments, and we do not apply the NAD model in the dome.

The extent of reaction of steam flowing through the cell will be governed by the ratio of the time constant for gas flow to sweep gas out of the cell, τ_{fl}, to the time constant for reaction, τ_h. An approximate measure of the efficiency, ϵ_h, of the steam-hydrogen conversion process is given by

$$\epsilon_h = \frac{\tau_{fl}}{\tau_{fl} + \tau_h}, \qquad \text{(B.1-3)}$$

assuming well-mixed gases in the cell. (A correction for the iron-steam equilibrium is needed when iron is the only remaining metal.) In what follows, we take the ratio τ_{fl}/τ_h to be the figure of merit for evaluating the efficiency of the NAD interactions.

The ratio τ_{fl}/τ_h is estimated as follows. First, we assume that mass transport rate limitations within the film are negligible and that only gas phase mass transport limits the reaction rate, and assume that the film does not run out of metal. The time constant for reaction of steam with the debris-coated surfaces, τ_h, is equal to V/hA_d, where V is the volume of the cell of interest and A_d is the area of the surfaces coated with debris films. Given the blowdown rate in moles per second, $\dot{n}$, the gas velocities and other information needed to evaluate Eq. (B.1-2) may be estimated by applying the ideal gas law to obtain the volumetric flow rate (m^3/s) and dividing by the cell cross section for flow, A_h. The time constant for gas flow through the cell is equal to the cell volume divided by the gas volumetric flow rate. After a little algebra, one may obtain

$$\frac{\tau_{fl}}{\tau_h} = \beta A_d (R\dot{n}L)^{m-1} A_h^{-m} \left(\frac{PD_g}{T}\right)^{1-m} Sc^{1/3-m}. \qquad \text{(B.1-4)}$$

Here, P and T are, respectively, the pressure and temperature of the gas, and R is the universal gas constant.

In CONTAIN, Eq. (B.1-2) with $\beta = 0.037$ and $m = 0.8$ forms the starting point of the model used for calculating condensation upon (or evaporation from) structures in the presence of forced flow, although the actual evaporation/condensation model includes many refinements not needed here. With these values of β and m, Eq. (B.1-4) becomes

$$\frac{\tau_{fl}}{\tau_h} = 0.037 A_d (R\dot{n}L)^{-0.2} A_h^{-0.8} \left(\frac{PD_g}{T}\right)^{0.2} Sc^{-0.467}. \qquad \text{(B.1-5)}$$

Quantitative results to be presented below will be based upon Eq. (B.1-5). Note also that, although we shall refer to Eq. (B.1-5) and similar relationships as representing "film models," they are in reality thin film models, in that various complications (e.g., wave action) that can arise when films are thick will be neglected in our discussion.

Examination of the various parameter dependencies in Eq. (B.1-5) shows that the net variations with pressure, temperature, gas composition and flow rate are weak and large changes in τ_{fl}/τ_h do not occur as the event proceeds. We evaluate Eq. (B.1-5) for conditions typical of the post-dispersal blowdown phase of the SNL/IET Zion experiments, which we take to be $\dot{n}$ = 250 g-moles/s, T = 1000 K, P = 4.5×10^5 Pa, and an H_2:H_2O ratio of 1:3.

We consider the cavity and chute in the SNL/IET Zion experiments and take $A_h = 0.067$ m^2 and L = 0.5 m. We assume that both the cavity and the chute surfaces are coated with debris films, since the experiments typically leave most chute surfaces as well as cavity surfaces coated with debris;* A_d is then equal to 3.7 m^2. Eqs. (B.1-5) and (B.1-3) then give $\epsilon_h \approx 0.30$. For the amounts of blowdown steam that exit the accumulator after debris dispersal terminates (typically ~300 g-moles), this efficiency is sufficient to generate another 60-100 g-moles of hydrogen, in addition to what is generated by the interactions with airborne debris. Applying a similar approach to estimate the heat transferred from the nonairborne debris results in an estimate of about 4 to 7 MJ. The latter is sufficient to account for 15-25% of the ΔP observed in the SNL/IET (Zion) experiments in which hydrogen could not burn, while this heat transfer plus the combustion energy of the additional hydrogen produced could account for 30-45% of the total ΔP observed in experiments in which the hydrogen did burn. (Both estimates neglect atmosphere-structure heat transfer.)

The results summarized here provide good support for the NAD concept. Using relatively standard correlations for heat and mass transfer, the analysis shows that significant nonairborne interactions should be expected.

B.2 Analytical Estimation of d_t and Scaling of the CONTAIN NAD Model

Including modeling for nonairborne debris in the CONTAIN code was originally motivated by the observation that, when hydrogen production was plotted against mass dispersed for the SNL/LFP experiments, the line did not go through the origin; instead, there was a substantial positive intercept, suggesting considerable hydrogen might be generated even if no debris was dispersed from the cavity [All91a]. Subsequent analyses of these and other data [Wil92] strengthened the belief that hydrogen generation and debris-steam heat transfer could not be explained in terms of the interactions of airborne debris alone. Since the potential importance of these nonairborne interactions was not known, and since the detailed physics was not known, only a simple parametric representation was deemed appropriate. Within the CONTAIN architecture, the simplest way of doing this was to allow the trapped field to interact with gas and steam using the same models, based upon spherical particles, that are used for the airborne debris fields, with the efficiency of the interaction being controlled by the user-specified trapped field diameter, d_t.

One difficulty with this approach is that, with the nonairborne field still being treated as if it consisted of spherical particles, it does not scale properly if the actual interactions are with films on structures. In this section, we consider how the user might vary d_t to obtain a zero-order correction for this deficiency. In the process, we also derive an expression which, in principle, permits one to specify the value of d_t in any given cell that would be required in order to match the value of ϵ_h that a model based upon surface films would give.

---

*T. K. Blanchat, private communication to the author.

Let S be the linear scale factor and let quantities with a subscript 0 refer to values at full (NPP) scale, i.e., with S = 1. Then, in a scaled experiment, actual lengths L, areas A, and debris masses m_d will be given by SL_0, S^2A_0, and $S^3m_{d,0}$, respectively. Since the molar gas flow rate, $\dot{n}$, is driven by the steam blowdown rate which scales as the vessel failure orifice area, we also have $\dot{n} = S^2\dot{n}_0$. Inserting these relations into Eq. (B.1-4), we obtain

$$\frac{\tau_{fl}}{\tau_h} = \beta S^{m-1} A_{d,0} (R\dot{n}_0 L_0)^{m-1} A_{h,0}^{-m} \left(\frac{PD_g}{T}\right)^{1-m} Sc^{1/3-m}. \tag{B.2-1}$$

For m = 0.8, Eq. (B.2-1) implies a weak ($S^{-0.2}$) negative dependence upon scale. For m = 1, there would be no dependence upon scale, and several other dependencies implied by Eq. (B.2-1) would vanish also.

The CONTAIN treatment models the nonairborne debris as spherical particles, with the Sherwood number and mass transfer coefficient given by

$$h = Sh\left(\frac{D_g}{d_t}\right) = \left(2.0 + 0.6 Re_d^{1/2} Sc^{1/3}\right)\left(\frac{D_g}{d_t}\right), \tag{B.2-2}$$

with analogous expressions for the Nusselt number and the heat transfer coefficient. The mathematical form of this expression differs from that of the expression given in Eq. (B.1-2) due to the presence of the constant term, 2.0, in the expression for Sh. However, for typical values of d_t (e.g., 0.01 in the standard prescription), the Reynolds number will be large, $> 10^3$, and the 2.0 may be dropped without important error resulting. The analysis then goes through as far as Eq. (B.1-4) as before, with $\beta = 0.6$ and m = 0.5. However, in going to an expression explicitly including the scale factor S as in Eq. (B.1-5), we must remember that CONTAIN calculates the debris surface area from

$$A_d = \frac{6m_d}{\rho_d d_t} = S^3 \frac{6m_{d,0}}{\rho_d d_t}, \tag{B.2-3}$$

where m_d is the mass of nonairborne debris in the cell, and ρ_d is the debris density. The fact that A_d is proportional to m_d and therefore scales as S^3, not S^2, is one source of the scaling mismatch in the CONTAIN NAD model.

The CONTAIN NAD analogue to Eq. (B.2-1) may be obtained by inserting Eq. (B.2-3) and the other scaled parameters into Eq. (B.1-4) together with $\beta = 0.6$ and m = 0.5:

$$\left(\frac{\tau_{fl}}{\tau_h}\right) = 3.6 S \frac{m_{d,0}}{\rho_d d_t^{3/2}} (R\dot{n}_0)^{-0.5} A_{h,0}^{-0.5} Sc^{-0.167} \left(\frac{PD_g}{T}\right)^{0.5}. \tag{B.2-4}$$

We may now estimate d_t by taking the ratio of Eq. (B.2-1) to Eq. (B.1-4), setting the result equal to unity, and solving for d_t. The result is

$$d_t = \left[\frac{3.6 S^{2-m}}{\beta A_{d,0}} \frac{m_{d,0}}{\rho_d} \left(\frac{A_{h,0} P D_g}{R \dot{n}_0 T} \right)^{m-0.5} L_0^{1-m} Sc^{m-0.5} \right]^{2/3} . \qquad \text{(B.2-5)}$$

From this equation, it is apparent that the current CONTAIN representation of nonairborne debris does not give a very good description of how the efficiency of the nonairborne interactions should vary as a function of several parameters in addition to geometric scale. Thus, the interaction should increase in efficiency as the surface area increases, but the model does not take this into account, and Eq. (B.2-5) indicates that d_t should be varied as $A_d^{-2/3}$ in order to compensate for this lack. On the other hand, the debris surface area in the CONTAIN representation increases as m_d increases, while this is not true in a surface film model, and Eq. (B.2-5) shows that d_t should be varied as $m_d^{2/3}$ in order to correct for this difference. These differences are all consequences of the fact that the current CONTAIN model scales debris surface in proportion to debris mass and not in proportion to actual structure surface areas.

There are several other mismatches which arise because the Reynolds Number exponent (m) for spheres, 0.5, is smaller than the values likely to be appropriate for structure surfaces (m = 0.8 in the CONTAIN forced flow correlations). The dependencies involved are relatively weak, but not negligible if the governing parameters vary over a wide range.

Given a particular correlation for heat and mass transfer at the structure interfaces, the constants β and m are known; e.g., β = 0.037 and m = 0.8 for the standard CONTAIN forced flow correlations. Eq. (B.2-5) then includes no unknown empirical constants and it can be applied immediately to estimate the appropriate value of d_t provided the debris mass, gas flow rates, geometric parameters, etc., appearing in Eq. (B.2-5) are known. In practice, Eq. (B.2-5) may be difficult to apply, especially in the present stand-alone analysis, due to large uncertainties in gas flow patterns and debris distributions, among other things.

One situation for which application Eq. (5.2-5) may not be so difficult is the Zion cavity and chute. The geometry is relatively simple, and once debris ejection terminates the remaining debris is present as films coating structure surfaces as assumed by the model. Furthermore, recent separate effects experiments with scaled models of the Zion cavity and chute indicate that simple turbulent flow patterns (as implicitly assumed by the model) exist in the chute, although more complex patterns exist in the cavity*. Scaling up the parameters cited at the close of Section B.1 gives $A_{d,0}$ = 370 m^3, $A_{h,0}$ = 6.7 m^2, L_0 = 5 m, and $\dot{n}_0$ = 25 kmoles/s (1 kmole ≡ 1000 g-moles). In the SNL/IET Zion experiments, debris ejected from the cavity corresponded to 60-80% of the total, implying 30% or 13 kg remained behind on the average; hence, $m_{d,0} = 1.3 \times 10^4$ kg. We assume β = 0.037 and m = 0.8 as in the CONTAIN forced flow correlations. With this input, evaluating Eq. (B.2-5) for S = 0.1

*M. Ishii, private communication to the authors.

gives the result d_t = 0.0097 m, surprisingly close to the value of d_t = 0.01 m developed empirically for the standard prescription.

Application of Eq. (B.2-5) to the Zion IET subcompartments is more complex. Experimentally, most debris was recovered from the subcompartment floor, but there may have been considerable relocation from whatever surfaces the debris initially adhered to upon de-entrainment. If we credit all subcompartment structure surfaces as being coated with debris during the time of interest, a small value of d_t, ~0.005 m, is estimated. However, it is not likely that more than a small fraction of the total subcompartment surfaces will be coated with debris films and, if they were, they would be so thin that they would probably cool too rapidly to be effective in producing hydrogen or heating the atmosphere (Section B.3). Based upon the trapped masses in the various cells of the 14-cell deck, it might be more reasonable to credit only structure surfaces in the first one to three cells of the subcompartments downstream of the chute exit (see Appendix A). This approach leads to estimates of the order of 0.017 m (first three cells) to 0.03 m (first cell only). These values would give reaction rates smaller by factors of 2.2 to 5 in the subcompartment than does the standard prescription value of d_t = 0.01 m (recall that hA_d varies as $d_t^{-3/2}$ in the CONTAIN NAD model). Even larger values of d_t would be implied if only floor surfaces were credited in applying Eq. (B.2-5).

The Surry geometry experiments do not provide a very good test of the model because the contribution of the NAD interactions was small in the CONTAIN calculations, and the distributions of debris remaining in the cavity that were observed after the test did not conform well to the uniform thin films assumed by the model.* In addition, flow fields in the cavity would likely not conform to the uniform distributions assumed by the model (there is no chute analogous to the Zion case). For what it is worth, application of Eq. (B.2-5) to the Surry geometry experiments would yield d_t values in the range 0.007-0.011 m, smaller than the value of 0.0156 m used in the experimental analyses. Use of these smaller values would tend to worsen agreement with the experimental hydrogen data somewhat. The effect would be relatively small, however, and probably less than other analysis uncertainties in the hydrogen production estimates.

Scaling. For scaled facilities, all quantities in Eq. (B.2-5) other than the explicit scale factor are the same, to lowest order. Since the standard prescription was defined on largely empirical grounds, we may write the scaling rule as

$$d_t(S) = d_t(S_e)\left(\frac{S}{S_e}\right)^{\frac{2(2-m)}{3}} = d_t(S_e)\left(\frac{S}{S_e}\right)^{0.8} \text{ for } m = 0.8, \qquad \text{(B.2-6)}$$

where $d_t(S)$ is the appropriate value at scale S and $d_t(S_e)$ is the value found to be appropriate for experiments at scale S_e. For the present standard prescription, $d_t(S_e)$ = 0.01 m and S_e= 0.1. Other scales of interest are S = 0.0255 (ANL/IET), S = 1/5.75 (CTTF), and

*T. K. Blanchat, private communication to the author.

S = 1 (NPP). For these scales, Eq. (B.2-6) with m = 0.8 implies d_t = 0.00335 m, 0.0156 m, and 0.063 m respectively. The values cited for the ANL/IET and CTTF experiments are those used in the main report. For NPP analysis, we would now prefer a slightly more conservative scaling based upon Eq. (B.2-6) with m = 1; see Section B.4.

Dependence upon Blowdown Rate. Another interesting implication of Eq. (B.2-5) is that the appropriate value of d_t in the CONTAIN model is expected to be a function of $\dot{n}_0$ and, hence, the blowdown rate. Although the dependence upon $\dot{n}_0$ is weak, $\dot{n}_0$ itself can vary over wide ranges, both in the course of a single event and when comparing different DCH scenarios. For example, the $\dot{n}_0$ value of 25 kmoles/s that was used here in connection with the SNL/IET Zion experiments is appropriate for the period immediately after the end of debris dispersal from the cavity, but it is less appropriate for the late stages of the blowdown. By the time the blowdown rate has declined to 5 kmoles/s, Eq. (B.2-5) indicates hA_d should decrease by factors of about 0.6 for m = 0.8 and 0.45 for m = 1. The failure of the standard prescription to take this effect into account is one reason why the standard prescription tends to overestimate the contribution of the late stages of the blowdown, relative to the early stages.

Eq. (B.2-5) also indicates that the standard prescription can underestimate NAD contributions at higher blowdown rates. The standard prescription acknowledges no dependence of d_t upon blowdown rate, while Eq. (B.2-5) implies that d_t should vary as $\dot{n}_0^{(2m-1)/3}$. For example, if an accident scenario is possible* with a fully-pressurized primary system and a vessel hole diameter of about 0.7 m, $\dot{n}_0$ would be an order of magnitude higher than in the IET Zion experiments. Eq. (B.2-5) then implies that, relative to the standard prescription, hA_d should be increased by factors of 2 to 3 for m in the range 0.8 to 1, respectively.

B.3 Debris-Structure Heat Transfer

We consider here a brief scoping analysis of debris-structure heat transfer. The intent is only to consider whether the process is potentially important and merits further study.

For heat transfer controlled by thermal diffusion through a bulk material, the time τ_{th} required for the thermal wave to progress though a layer of thickness z is given approximately by

$$\tau_{th} = \frac{\pi z^2}{4\alpha}, \qquad \text{(B.3-1)}$$

where $\alpha \equiv k/\rho c_p$ is the thermal diffusivity, k is the thermal conductivity, ρ is the density, and c_p is the heat capacity. If the film diffusivity is less than that of the substrate, the film

*Some investigators would argue that the example considered here is outside the credible range.

properties are governing and as a first approximation, Eq. (B.3-1) gives the time required for cooling to reach the front surface of a film cooled at the rear.

If the thermal diffusivity of the substrate is lower than that of the film, Eq. (B.3-1) corresponds more closely to the characteristic time required for the thermal wave to penetrate a distance z into the substrate. However, if the product ρc_p for the substrate is comparable to ρc_p for the film, substantial cooling of a film of thickness z requires heating a comparable thickness of substrate. For scoping purposes, we still take Eq. (B.3-1) as a first approximation for the characteristic cooling time of a film of thickness z, except that α is evaluated for the substrate material. (Much more sophisticated analyses are, of course, possible.)

For the cavity and chute areas and debris masses considered in Section B.2, film thicknesses slightly under 1 mm are calculated. Eq. (B.3-1) then gives τ_{th} values of about 0.5-1 s, assuming film properties control with a thermal conductivity of 5 W/m-K, a value appropriate for oxidic constituents such as Al_2O_3. For the subcompartment cases considered in Section B.2, estimated τ_{th} values are 0.03 s for the case of debris spread over all subcompartment surfaces, 1 s for debris spread over the surfaces of the first three cells downstream of the chute, and 7 s for the first cell only downstream of the chute. The 0.03 s result provides another reason for ruling out consideration of debris films spread over all subcompartment structures, even if this scenario were otherwise considered to be credible. However, the τ_{th} values cited for the other subcompartment cases, and for the cavity-and-chute case, are of the same order as the time scale of the event. This result supports the belief that debris-structure heat transfer does not eliminate the NAD interactions but that this heat transfer does need to be taken into account. It provides another reason for believing that the current CONTAIN treatment may overestimate the contribution from the later stages of the blowdown.

Given that the debris thermal properties are controlling, the values of τ_{th} might be reduced by the presence of metallic constituents, since the values estimated above were based upon thermal conductivities appropriate for oxidic constituents. On the other hand, the effective thermal conductivity could be reduced, and/or the film thickness increased, by effects such as gas bubble formation in the debris.

It is likely that debris film properties are actually controlling for τ_{th} only for debris deposited on metallic substrates. Most of the available deposition surfaces in the Zion experiments were concrete, not metal. (More metal surface was available in the Surry experiments.) For normal concrete, handbook values of the thermal conductivity are lower, of the order of 1 W/m-K [Per84]. However, concrete contacted by molten debris will hardly be normal concrete; decomposition processes will certainly affect the thermal properties and gas evolution may produce porosity that results in an increased thermal resistance at the interface. Whatever the effects of decomposition, it seems plausible that τ_{th} values somewhat larger than those cited above can arise for debris films deposited upon concrete, but no detailed analysis of this problem has been attempted. The expectation remains that cooling time scales due to debris-structure heat transfer are not sufficiently rapid to eliminate the

NAD interactions. It is also doubtful that the heat transfer is negligible, unless interface resistances are large.

Scaling. If we assume film thickness scales with the facility, $\tau_{th} \propto S^2$. Since the time scale of the DCH event is expect to be proportional to S, the simple model sketched here indicates that debris-structure heat transfer may be less important at full scale than at experimental scale. This conclusion depends upon the assumption that thermal diffusion within the bulk materials is controlling. If a contact resistance at the debris-structure interface is controlling, the importance of debris-structure heat transfer may be less dependent upon scale.

It is interesting to note that the comparison of the SNL/IET and ANL/IET counterpart experiments presented in Section 6.8 did not show evidence of a large reduction in NAD interactions at the smaller scale. Such a reduction might be expected from Eq. (B.3-1). One interpretation would be that an interface resistance does play a controlling role in the rate of debris-structure heat transfer, at least at the experimental scales. The fact that cavity dispersal fractions showed little scale dependence is also consistent with this interpretation. Though these results are not conclusive, they do suggest that the possibility of a high thermal resistance at the interface is worth considering.

B.4 Discussion

For the Zion cavity and chute, the model represented by Eq. (B.2-5) yields excellent agreement with the empirical standard prescription d_t value of 0.01 m. Although this agreement no doubt includes an element of luck, it is certainly encouraging that agreement is obtained in the one instance that is sufficiently simple that one might hope to obtain a reasonably quantitative test of the underlying concept. Hence it is worth considering whether the model could be extended to obtain a more mechanistic treatment of the nonairborne interactions in CONTAIN.

First, we may note that a consistent application of the model to the Zion IET experiments would yield less NAD contribution than does the present standard prescription, for several reasons:

- The model predicts $d_t \approx 0.01$ m for the Zion cavity and chute only during the early part of the post-dispersal blowdown; later in the blowdown, larger values of d_t is implied.

- It was assumed that 100% of cavity and chute surfaces were coated with debris, which is probably untrue; allowing for incomplete coating of some surfaces would increase the value of d_t implied by the model.

- For reasonable debris film areas, the model predicts significantly larger values of d_t in the subcompartments.

- Debris-structure heat transfer may bring about some additional reductions in the efficiency of the NAD interactions.

These differences with respect to the standard prescription do not argue against the utility of the model, since the standard prescription was developed by assuming that NAD was responsible for all the interactions not accounted for by the airborne debris. In reality, results given in Section 6.5 of the main report indicate that codispersed cavity water may have made a significant contribution also.

In considering possible scale distortions not accounted for in Eq. (B.2-5), those that have been identified appear to be in the direction of increasing the efficiency of the NAD interactions at large scale. These include:

- Reduced importance of debris-structure heat transfer on the time scale of the event. (This reduction may also apply to DCH scenarios involving more rapid blowdown due to a large vessel failure size.)

- Departures from thin-film behavior, which could tend to enhance heat and mass transfer rates due to wave formation.

- Presence of small-scale structure (plumbing, etc.) in NPP that is not modeled in the experiments, which could enhance film surface areas.

Whether these effects are actually important is not known. We consider them sufficiently plausible that we recommend applying Eq. (B.2-6) with $m = 1$ rather than $m = 0.8$ when estimating d_t at plant scale, or when correcting for other deviations from the conditions (such as vessel failure size) of the experiments used to develop the standard prescription. Note that using $m = 1$ actually only corresponds to assuming that the NAD interaction efficiencies are independent of scale and independent of blowdown rate. In view of the many uncertainties, this assumption would seem to provide a reasonable starting point. The more important recommendation, however, is that a wide range of uncertainty in d_t be acknowledged in sensitivity studies.

As for the prospects of improving the current CONTAIN model, further study of some of the uncertainties considered here may be warranted before making a decision. Developing a mechanistic model based upon debris films would require means of coping with a number of uncertainties, including effects such as the following:

- Uncertain debris distributions;

- Complex flow fields in typical containment cavity and subcompartment geometries;

- Debris-structure heat transfer, including the interface resistance question;

- The validity of the assumption that only gas-phase mass transport rates control chemical reaction rates.

- Effects of small-scale structures present in actual NPP containments; and

- Debris relocation from initial deposition surfaces, which may be more likely to occur during the time scale of the event at NPP scale than at experimental scale.

In some cases, it may be possible to argue that these effects are minor, but this has not yet been demonstrated.

At a minimum, it might be desirable to recast the NAD model to a form appropriate for debris films on structures. This reformulation might reduce the need for the user to compensate for the various scaling mismatches considered in Section B.2 by varying the artificial trapped field diameter, d_t. The model would have to remain parametric in key respects, pending improved understanding of the uncertainties enumerated above. Even a decision to reformulate the model to this extent may best await a better understanding as to whether interaction with debris films is the dominant process currently represented by the NAD model, since other processes may also contribute, as was acknowledged in Section 3.2.7 and elsewhere in the main report. Separate effects experiments using low-temperature simulants may provide useful insights on this question. Studies of this type for the Zion geometry are now in progress at Purdue University [Ish93].

References

Bir60. R. B. Bird, W. E. Stewart, and E. N. Lightfoot, Transport Phenomena, John Wiley & Sons, Inc., NY, 1960.

Ish93. M. Ishii et al., "Separate Effects Experiments on Phenomena of Direct Containment Heating - Air-Water Simulation Experiments in Zion Geometry," PU NE-93/1, Purdue University, March 1993.

Per84. R. H. Perry, D. W.Green, and J. O. Maloney, Perry's Chemical Engineering Handbook, McGraw-Hill Book Co., NY, 1984.

Was91. K. E. Washington et al., "Reference Manual for the CONTAIN 1.1 Code for Containment Severe Accident Analysis," NUREG/CR-5715, SAND91-0835, Sandia National Laboratories, July 1991.

Wil92. D. C. Williams, "An Interpretation of the Results of some Recent Direct Containment Heating (DCH) Experiments in the Surtsey Facility," SAND92-0442, Proceedings of the NURETH-5 Conference, Salt Lake City, Utah, September 1992.

Appendix C

Independent Evaluation of Mitigation Effects

In Section 6.7 of the main text, it was shown that mitigation due to the combined effects of atmosphere-structure heat transfer and incomplete or delayed hydrogen combustion due to temporary oxygen starvation in the subcompartments plays an important role in the CONTAIN analyses of the IET experiments. This mitigation is also a key premise of the argument that debris-water interactions and/or interactions of nonairborne debris with noncoherent steam are important in the IET experiments performed in Zion geometry. Without the mitigation, there is much less tendency to underpredict the ΔP results of these experiments in calculations that include only the interactions of airborne debris with coherent steam.

Hence, it seemed important to provide an independent check upon the mitigation calculated by CONTAIN. Since an approximate check can be obtained using simple analytical methods, it is included here.

We start by noting that, to a good approximation, the pressurization, ΔP, of the Surtsey vessel due to transfer of energy ΔU to the atmosphere is given by

$$\frac{\Delta P}{\Delta U} = \frac{R}{VC_v} = 0.00381\ MPa/MJ, \tag{C-1}$$

where R is the universal gas constant, V is the Surtsey free volume (89.8 m^3 in the Zion IET experiments), and C_v is the molar heat capacity at constant volume (~24.3 J/g-mole K). We estimate the reduction in ΔP by estimating the reduction in energy input into the containment, relative to what it would be if there were no atmosphere-structure heat transfer and if all DCH-produced hydrogen could burn. We consider only the experiments in which the Surtsey atmosphere contained sufficient oxygen to support combustion of the DCH-produced hydrogen.

We estimate the atmosphere-structure heat transfer rates, $\dot{Q}$, using correlations that are similar to those employed by the CONTAIN code:

$$\begin{aligned} h_{nc} &= 0.141\frac{k}{L}Gr^{1/3}Pr^{1/3}, \\ h_{ff} &= 0.037\frac{k}{L}Re_L^{0.8}Pr^{1/3}, \\ h_{rad} &= \sigma\epsilon_{g\text{-}s}(T_g^{\,2}+T_s^{\,2})(T_g+T_s), \\ \dot{Q} &= (h_{rad}+\max(h_{nc},h_{ff}))A_s(T_g-T_s). \end{aligned} \tag{C-2}$$

Here h_{nc}, h_{ff}, and h_{rad} are, respectively, the heat transfer coefficients for natural convection, forced flow, and thermal radiation. Gr is the Grashof number, Pr the Prandtl number, Re_L the Reynolds number based upon gas flow velocities across structures with a characteristic

length L, k is the gas thermal conductivity, and ϵ_{g-s} is the effective emissivity for gas-structure thermal radiation. A_s is the area of structure surfaces and T_g and T_s are, respectively, the temperatures of the gas and the structure surfaces.

Conditions in the dome and the subcompartments are very different and Eq. (C-2) must be evaluated separately for the two regions. During the period of debris dispersal, gas entering the subcompartments would consist of almost pure hydrogen at temperatures close to the debris temperature (2500 K) if debris-steam equilibrium were to be achieved; since the chromium reaction energy is sufficient to compensate for the energy needed to heat the hydrogen, the debris would not cool. However, in CONTAIN calculations with the standard particle size distribution, equilibrium is approached but not achieved, and it would be more representative to take the gas temperature to be 2000 K and the composition to be 75% hydrogen, 25% steam. In the subcompartments, gas flow velocities may be calculated assuming a cross section for flow of about 1 m^2 and a flow rate of about 300 g-moles/s (the approximate blowdown rate during debris dispersal), and characteristic lengths of the structures are taken to be 1 m.

Atmosphere emissivities are expected to be high due to the presence of dense aerosol clouds; an emissivity value of 0.8 is assumed here as in the CONTAIN standard DCH input prescription. Structure surface emissivities are also about 0.8. Taken together, these values imply $\epsilon_{g-s} \approx 0.67$. Structure temperatures, T_s, were assumed to be 500 K in the subcompartments. Structure areas in the subcompartments total about 40.6 m^2. Hot debris films may render some small fraction of the subcompartment surfaces ineffective as heat sinks, but no correction is applied for this effect, since we are comparing with the CONTAIN case without NAD interactions modeled. In any event, the correction would be small.

In the dome, maximum experimental temperatures observed are in the range 600-700 K; 600 K is assumed here. Structure surfaces in the dome do not heat significantly during the event, and T_s was therefore taken to be 300 K. Surface areas are about 156 m^2.

Using these values, approximate heat transfer coefficients and heat transfer rates implied by Eq. (C-2) were evaluated on a small spreadsheet program. Results are summarized in Table C-1.

Table C-1
Mitigation by Heat Transfer

Region	A_s (m^2)	h_{nc} W/m^2-K	h_{ff} W/m^2-K	h_{rad} W/m^2-K	T_g-T_s (K)	$\dot{Q}$ MJ/s
Subcomp.	40.6	42	96	404	1500	30.5
Dome	156	24.2	---	15.4	300	1.85

The extreme temperatures assumed here for the subcompartments prevail only for a time period comparable to the time during which debris is being dispersed from the cavity, typically about 0.4 s in the Zion-geometry SNL/IET experiments. Hence, about 12 MJ would be lost from the subcompartments during this period. Eq. (C-1) indicates this energy loss would reduce ΔP by about 0.046 MPa, relative to the adiabatic case.

At the end of the debris dispersal time, much of the hydrogen produced will still remain in the 4.6 m^3 volume of the subcompartments, which contain no oxygen at this time. Assuming the pressure is about 0.3 MPa at this time (which is well before the time of maximum pressure), the subcompartments at 2000 K would contain about 111 g-moles of gas. If we assume the same composition as was assumed above (75% hydrogen), the number of hydrogen moles remaining in the subcompartments at the end of entrainment, $n_{H2,e}$, is about 83 g-moles. Since hydrogen combustion releases 0.2406 MJ/g-mole, failure to burn any of this hydrogen would reduce ΔP by another 0.076 MPa, relative to the adiabatic complete combustion case.

This estimate neglects the fact that, in the SNL/IET Zion experiments, the coherent steam fraction, f_{coh}, was only 0.20-0.40; that is, only 20-40% of the total accumulator steam was discharged at the time debris dispersal was effectively complete. As the blowdown continues, some of the hydrogen present at the end of entrainment will be carried to the dome, where it can burn. If we assume that the subcompartment atmosphere is well mixed during the blowdown, it can be easily shown that the hydrogen remaining in the subcompartments at the end of the blowdown, n_{H2}, is approximately given by

$$n_{H_2} = n_{H_2,e} e^{-V_{blo,e}/V_{sub}},$$
$$V_{blo,e} = \frac{n^0_{H_2O}(1-f_{coh})RT_{blo}}{P_{sub}} \qquad \text{(C-3)}$$

where V_{sub} is the subcompartment volume, $V_{blo,e}$ is the volume of blowdown steam entering the subcompartments after the end of entrainment, P_{sub} is the pressure in the subcompartments (essentially equal to the Surtsey pressure, ~0.4 MPa at this time), T_{blo} is the temperature at which the blowdown steam enters the subcompartments (~450 K, due cooling as a result of expansion). The initial steam inventory in the accumulator, n^0_{H2O}, is about 500 g-moles in the SNL/IET Zion experiments. The SNL/IET-3 and SNL/IET-4 experiments, used in the examples below, had $f_{coh} \approx 0.25$. Using this value, Eq. (C-3) gives $n_{H2} = \sim 39$ g-moles for the amount of hydrogen remaining in the subcompartments at the end of the blowdown.

This hydrogen is unlikely to contribute to DCH pressurization because it can burn only insofar as natural convection between the subcompartments and the dome mixes it with oxygen, a relatively slow process. Furthermore, high steam/hydrogen ratios and reduced temperatures in the subcompartments at these later times may limit hydrogen combustion even as oxygen does become available. In any event, the experimental results show that peak pressures were achieved at or before the time the blowdown ends in the SNL/IET Zion experiments.

It appears, then, that the ~39 g-moles remaining in the subcompartments at the end of blowdown will not contribute, reducing ΔP by about 0.036 MPa. Since the time required for blowdown, ~3 seconds, is long compared with the entrainment time assumed previously, additional heat losses occur which were not previously accounted for. We neglect any additional losses in the subcompartments, because the entering steam is relatively cool; however, the estimated energy losses in the dome are about 5.5 MJ during this period (see Table C-1), reducing ΔP by an additional 0.021 MPa.

Relative to the adiabatic complete combustion case, then, the estimated mitigation is about 0.046 + 0.036 + 0.021 = 0.103 MPa, a very significant amount. This result clearly lends good qualitative support to the general CONTAIN prediction that mitigation was important in these experiments.

In order to obtain a more quantitative comparison, the IET-3 and IET-4 CONTAIN analyses with no nonairborne debris and no debris-water interactions (Cases I3c1410 and I4c1410, respectively) were recalculated with all structure areas set equal to 10^{-20} m^2 in order to eliminate heat transfer, and with the BSR temperature threshold set equal to 300 K in order to assure complete hydrogen reaction. For IET-3, the calculated ΔP in the original calculation was 0.110 MPa while the calculation without mitigation (Case I3c1427) gave 0.183, a difference of 0.073 MPa. For IET-4, ΔP in the original calculation was 0.141 MPa, while the calculation without mitigation (Case I4c1415) yielded ΔP = 0.235 MPa, for a difference of 0.094 MPa.

These results agree reasonably well with the simplified calculation, in view of the many approximations made in the latter. For example, in estimating the heat losses from the subcompartments during the debris dispersal period, the simplified calculation neglects the fact that some of the lost energy can be made up by continued heat transfer from the airborne debris that is still present in parts of the subcompartment volume at this time. The intent of the simplified analysis is only to provide a sanity check on the CONTAIN calculation; it is not to be expected that the simplified approach would be useful for quantitative DCH calculations.

The simplified analysis supports the belief that the mitigation effects are being evaluated reasonable well by the CONTAIN code. It is concluded, therefore, that there is little reason to doubt the implications of the CONTAIN calculations that the mitigation effects are important and must be properly taken into account in DCH analysis.

Appendix D

Tabulation of CONTAIN Results

The purpose of this Appendix is to provide, in one place, a tabulation of all the CONTAIN standard prescription and sensitivity study cases that were performed after the standard input prescription was defined and frozen. Analyses performed prior to definition of the standard prescription are not included. Some of the calculations summarized here are discussed in the main report in connection with the model assessments the calculations were intended to support. Some of the calculations tabulated here were not discussed in the main report, or were alluded to only in general terms. In any event, the purpose of this Appendix is to serve as a data compilation for possible future reference. No discussion or interpretation of the results is given here.

The format of the tables is similar to that used in Section 6 of the main report. Results tabulated include the pressure rise due to DCH (ΔP), the fraction of debris dispersed from the cavity which is transported beyond the subcompartments (f_{dome}), the number of g-moles of hydrogen remaining at the end of the event ($N_{f,H2}$), the number of moles of hydrogen burned ($N_{H2,burn}$), and the number of moles of hydrogen produced ($N_{H2,prod}$). In calculating the last two numbers, all decrease in containment oxygen inventory is interpreted as representing hydrogen which is first produced and then burned, as was done in the main report.

The experiments are grouped as follows:

Table D-1. Open geometry experiments (SNL/WC series and SNL/LFP-8A).

Table D-2. Compartmentalized SNL/LFP experiments (all SNL/LFP other than LFP-8A).

Table D-3. SNL/IET Zion experiments with partial or total inerting.

Table D-4. SNL/IET Zion experiments in which hydrogen could burn

Table D-5. ANL/IET Zion experiments

Tables D-6, D-7, D-8. SNL/IET-9, SNL/IET-10, and SNL/IET-11, respectively.

Within each table, the experiments are grouped in numerical order. For each experiment, the experimental results are given first and followed by the results calculated using the standard input prescription. With a few exceptions, the remaining cases then follow in numerical order by case number, which is the order in which the calculations were performed.

In the course of this work, it was discovered that input errors had been made in some of the runs. (In this context, any unintended deviation from the standard prescription is

considered to be an error.) When the effect of the error was substantial, the affected runs were either discarded or repeated. When the effect was minor, not all the affected runs were either repeated or discarded, especially when it was discovered that the same error had been made in a number of the runs. In all such cases, the magnitude of the effect was assessed by repeating at least one of the affected cases in order to demonstrate that the effect was indeed minor. The known cases where such input errors exist are as follows:

- TOF/KU Trapping Length L_1, SNL/IET Surry Experiments. In almost all the analyses of the SNL/IET Surry geometry experiments performed in CTTF, it was found that, for the cell representing the crane wall annulus (Cell 8), the first trapping length L_1 for the TOF/KU model had been set to a value equal to twice the width of the annulus. The stnadard prescription would call for L_1 to be equal to the annulus width. Case I10c829 was run with this error corrected (Table D-7), with only very minor changes observed.

- 'fromcell' Specified in SNL/IET-9 and SNL/IET-10 Analyses. CONTAIN includes an option in which the user can specify the flow path by which debris enters a cell for use in evaluating the TOF/KU trapping model. In the standard prescription the code is allowed to choose the dominant flow path; however, most of the IET-9 and IET-10 analyses were found to have been run with the flow path for debris entering the dome (Cell 9) specified to be the path from the seal table room (Cell 6). Correcting the error for IET-10 (Case I10c820, Table D-7) made no discernible difference. A very minor change did result for IET-9 (Case I9c820 in Table D-6).

- Incorrect Blowdown for SNL/IET-11. Most of the runs for the IET-11 analysis were set up with the melt generator and accumulator improperly defined, which allowed the blowdown to proceed somewhat too rapidly. Several runs were performed with this error corrected. They appear with the entry "corrected blowdown" in the "Description" column of Table D-8. Correcting the error reduced the calculated ΔP by 0.003 to 0.006 MPa.

- Drop-side diffusivity was set to 10^{-4} m^2/s in many of the SNL/IET Zion analyses, instead of being set to infinity as the standard prescription calls for. Correcting the error made such a trivial difference that it was not apparent in the fourth decimal digit of the output. Since results in this Appendix are only reported to two or three decimal digits, no effort has been made to identify which cases included the error.

Table D-1
Results for Open Containment Geometry Experiments (WC, LFP-8A)

Case	Description	ΔP (MPa)	f_{dome}	Hydrogen Data (moles)		
				$N_{f,H2}$	N_{burn}	N_{prod}
	WC-1 Experimental Results	**0.272**	**0.033**	**145**	---	---
W1c506	Standard input prescription	0.314	0.063	152	1.0	153
W1c505	L_1 = 6V/S (5.1m)	0.277	0.048	145	1.0	146
W1c507	GFT trapping	0.356	0.087	165	1.1	166
W1c508	No trapping	0.439	0.092	272	1.3	273
W1c510	No NAD	0.300	0.063	105	1.1	106
W1c511	Particle mmd = 1.45mm	0.277	0.059	144	1.0	145
W1c512	GFT trapping, particle mmd = 1.45mm	0.323	0.083	152	1.0	154
W1c513	s_d = 5 in Cell 4, s_d = 10 in Cell 5	0.275	0.011	155	1.0	156
W1c514	No trapping, structures, or NAD	0.572	0.112	249	1.4	250
W1c515	s_d = 5 in Cell 4	0.312	0.015	154	1.0	155
	WC-2 Experimental Results	**0.286**	**.052**	**179**	---	---
W2c504	Standard input prescription	0.317	0.064	143	3.8^+	147
W2c505	No NAD	0.302	0.064	102	1.1	103
W2c506	s_d = 5 in Cell 4	0.316	0.0148	144	4.1^+	148
W2c501	15% co-dispersed water	0.306	0.055	208	0.9	209
W2c502	15% co-dispersed water, no NAD	0.288	0.056	159	0.9	160
W2c503	15% co-dispersed water, s_d = 5 in Cell 4	0.305	0.012	209	0.9	210
W2c507	100% co-dispersed water	0.296	0.071	378	0.4	378
W2c508	100% co-dispersed water, no NAD	0.269	0.081	298	0.4	298

$^+$ Autoignition (srtemp) threshold (950K) exceeded

Table D-1 (Continued)
Results for Open Containment Geometry Experiments (WC, LFP-8A)

Case	Description	ΔP (MPa)	f_{dome}	Hydrogen Data (moles)		
				$N_{f,H2}$	N_{burn}	N_{prod}
W2c509	as W2c507, reaction thresh = 900K	0.296	0.071	380	0.4	380
W2c510	as W2c508, reaction thresh = 900K	0.269	0.081	300	0.4	300
	WC-3 Experimental Results	**0.275**	**0.073**	**181**	---	---
W3c501	Standard input prescription	0.296	0.065	152	2.2	154
W3c502	No NAD	0.289	0.068	133	2.2	135
W3c503	s_d = 5 in Cell 4	0.295	0.015	153	~2	155
	LFP-8A Experimental Results	**0.172**	**0.026**	**139**	---	---
L8ac501	Standard input prescription	0.202	0.048	119	0.8	119
L8ac502	No NAD	0.177	0.047	79	0.7	80
L8ac504	s_d = 5 in Cell 4	0.202	0.011	119	0.8	119

Table D-2
Results for LFP Experiments (Compartmentalized Cases)

Case	Description	ΔP (MPa)	f_{dome}	Hydrogen Data (moles)		
				$N_{f,H2}$	N_{burn}	N_{prod}
	LFP-1A Experimental Results	**0.117**	**0.026**	**235**	---	---
L1ac501	Standard input prescription	0.206	0.230	188	1.0	189
L1ac502	No NAD	0.198	0.240	158	1.1	159
L1ac503	NAD in cavity only	0.197	0.227	182	1.0	183
L1ac504	s_d = 5 in Cell 4, s_d = 10 in Cell 5	0.140	0.076	195	0.6	195
L1ac505	L_2 = L_3 in Cell 4 (subcompartment)	0.192	0.208	186	0.9	187
L1ac506	'rhodg = gas'	0.136	0.090	176	0.6	177
L1ac507	'vnost = cnvel'	0.206	0.230	188	1.0	189
L1ac508	s_d = 5 in Cell 4	0.140	0.075	195	0.6	195
	LFP-1B Experimental Results	**0.066**	**0.037**	**128.**	---	---
L1bc501	Standard input prescription	0.072	0.166	118	0.3	119
L1bc502	No NAD	0.058	0.176	58	0.3	59
L1bc503	NAD in cavity only	0.068	0.164	118	0.3	118
L1bc504	s_d = 5 in Cell 4	0.063	0.042	119	0.3	120
	LFP-2A Experimental Results	**0.102**	**0.069**	**151.4**	---	---
L2ac501	Standard input prescription	0.138	0.175	148	0.6	148
L2ac502	No NAD	0.127	0.183	98	0.6	98
L2ac503	NAD in cavity only	0.133	0.172	147	0.6	148
L2ac504	s_d = 5 in Cell 4 (subcompartment)	0.119	0.046	150	0.6	150

Table D-2 (Continued)
Results for LFP Experiments (Compartmentalized Cases)

Case	Description	ΔP (MPa)	f_{dome}	Hydrogen Data (moles)		
				$N_{f,H2}$	N_{burn}	N_{prod}
	LFP-2B Experimental Results	**0.118**	**0.028**	**154**	---	---
L2bc501	Standard input prescription	0.180	0.265	157	2.7	159
L2bc502	No NAD	0.171	0.278	127	2.7	129
L2bc503	NAD in cavity only	0.176	0.262	156	2.7	158
L2bc504	s_d = 5 in Cell 4 (subcompartment)	0.145	0.074	161	2.1	164
	LFP-2C Experimental Results	**0.131**	**0.131**	**184**	---	---
L2cc501	Standard input prescription	0.178	0.257	162	1.0	163
L2cc502	No NAD	0.172	0.276	142	1.0	144
L2cc503	NAD in cavity only	0.175	0.253	162	1.0	163
L2cc504	s_d = 5 in Cell 4 (subcompartment)	0.147	0.072	166	0.8	166

Table D-3
Results for SNL/IET Experiments with Partial or Total Inerting

Case	Description	ΔP (MPa)	f_{dome}	Hydrogen Data (moles)		
				$N_{f,H2}$	N_{burn}	N_{prod}
	SNL/IET-1 Experimental Results	**0.098**	**0.116**	**230**	**3**	**233**
I1c1408	Standard input prescription	0.115	0.107	271	0.5	271
I1c1407	Dome L_1 = 4.15m (6V/S value)	0.111	0.108	271	0.4	271
I1c1409	NAD in Cavity Only	0.093	0.108	216	0.5	216
I1c1410	No NAD	0.076	0.117	130	0.8	131
I1c1411	s_d = 5 in subcompartment	0.104	0.034	294	0.2	294
I1c1412	No NAD, 100% co-dispersed water	0.111	0.227	216	1.6	217
I1c1413	NAD d_t = 0.02m, 100% water	0.134	0.212	270	1.4	271
	SNL/IET-1R Experimental Results	**0.110**	**0.105**	**238**	**11**	**248**
I1rc1407	Standard input presentation	0.101	0.096	248	0.6	247
I1rc1409	NAD in cavity only	0.083	0.096	199	0.5	198
I1rc1410	No NAD	0.063	0.095	100	0.5	99
I1rc1412	s_d = 5 in subcompartment	0.092	0.031	265	0.5	264
I1rc1405	$D_{drop} = 10^{-8}$ m^2/s	0.098	0.098	90	0.6	89
I1rc1406	No NAD, $D_{drop} = 10^{-8}$ m^2/s	0.063	0.096	80	0.5	79
I1rc1413	No NAD, 100% co-dispersed water	0.083	0.122	187	0.2	185
I1rc1414	NAD d_t = 0.02m, 100% water	0.109	0.122	250	0.3	249
	SNL/IET-5 Experimental Results	**0.103**	**0.057**	**468**	**53**	**319**
I5c1412	Standard input prescription	0.212	0.084	140	310	247
I5c1407	Default DFB Conc. Limits	0.085	0.102	430	18	245
I5c1409	Default DFB, NAD in cavity only	0.073	0.102	390	16	203
I5c1410	Default DFB, no NAD	0.054	0.099	281	14	92
I5c1411	Default DFB, s_d = 5 in subcompartment	0.075	0.031	446	12	255
I5c1413	No NAD, 100% co-dispersed water	0.067	0.134	365	7	170
I5c1414	NAD d_t = 0.02m, 100% water	0.089	0.135	431	10	239

Table D-4
SNL/IET (Zion Geometry) Experiments in Which H_2 Could Burn

Case	Description	ΔP (MPa)	f_{dome}	Hydrogen-Data (moles)		
				$N_{f,H2}$	$N_{H2,burn}$	$N_{H2,prod}$
	IET-3 Experimental Results	**0.246**	**0.0875**	**37**	**190**	**227**
I3c1407	Standard input prescription	0.228	0.101	21	232	253
I3c1406	Dome L_1=6 V/S (4.15m)	0.224	0.100	21	230	251
I3c1408	GFT trapping in dome	0.232	0.102	21	234	255
I3c1409	NAD in cavity only	0.186	0.102	19	192	211
I3c1410	No NAD	0.110	0.099	18	84	103
I3c1412	s_d=5 in subcompartment	0.235	0.032	20	241	261
I3c1413	100% debris dispersal	0.218	0.092	16	193	208
I3c1414	NAD in cavity only, 100% dispersal	0.133	0.092	24	102	125
I3c1415	No NAD, 100% dispersal	0.133	0.092	24	102	126
I3c1417	d_t=0.005m	0.285	0.102	23	326	349
I3c1418	NAD in cavity only, d_t=0.005m	0.231	0.103	23	264	287
I3c1419	No structures (adiabatic)	0.401	0.116	5.4	256	261
I3c1420	Particle mmd=0.5mm	0.236	0.120	21	238	259
I3c1422	No NAD, 100% co-dispersed water	0.184	0.141	29	151	180
I3c1423	No NAD, particle d=0.125mm (1 field)	0.175	0.153	26	127	153
I3c1424	No NAD, 100% water, mmd=0.5mm	0.215	0.157	33	182	215
I3c1425	100% water, NAD d_t=0.02m	0.232	0.136	23	224	247
I3c1427	No NAD, no struc, srtemp=300	0.183	0.116	0	104	104
I3c1428	No NAD, d=0.125mm, subcomp. 'trapmul'=1.5	0.149	0.112	23	117	140
I3c1429	'trapmul'=0.667 in subcompartment	0.233	0.143	21	234	255
I3c1430	Default DFB concentrations	0.232	0.102	10	242	253

Table D-4 (Continued)
SNL/IET (Zion Geometry) Experiments in Which H_2 Could Burn

Case	Description	ΔP (MPa)	f_{dome}	Hydrogen-Data (moles)		
				$N_{r,H2}$	$N_{H2,burn}$	$N_{H2,prod}$
I3c1431	No trapping	0.372	0.720	107	317	427
I3c1432	No trapping and no structures	0.716	0.946	8	436	444
I3c1433	$D_d = 10^{-8}$ m²/s	0.154	0.103	10	89	99
I3c1434	As i3c1425 with $D_d = 10^{-8}$ m²/s	0.167	0.157	14	87	101
	SNL/IET-4 Experimental Results	**0.262**	**0.197[a]**	**63**	**240**	**303**
I4c1407	Standard input prescription	0.266	0.071	17	271	288
I4c1408	No airborne debris, NAD d_t = 0.002m	0.358	0	36	435	471
I4c1409	NAD in cavity only	0.209	0.071	25	205	231
I4c1410	No NAD	0.141	0.075	24	115	138
I4c1412	s_d = 5 in subcompartment	0.268	0.024	19	281	300
I4c1413	No NAD, 100% co-dispersed water	0.216	0.125	35	181	216
I4c1414	No NAD, no structures	0.224	0.091	12	128	140
I4c1415	No NAD, no structures, srtemp = 300K	0.235	0.091	0	140	140
14c1416	NAD d_t = 0.02m, 100% water	0.291	0.117	28	250	288
FCI effects damaged subcompartment structures, which allowed increased transport beyond the subcompartment						
	SNL/IET-6 Experimental Results	**0.279**	**0.138**	**154**	**345**	**319**
I6c1407	Standard input prescription	0.248	0.085	165	256	240
I6c1409	NAD in cavity only	0.177	0.086	174	178	172
I6c1410	No NAD	0.127	0.086	191	98	108
I6c1411	s_d = 5 in subcompartment	0.250	0.028	161	272	252
I6c1412	'srtemp' = 600 in dome	0.365	0.085	19	401	239
I6c1413	No structures (adiabatic)	0.554	0.100	3.3	429	252

Table D-4 (Continued)
SNL/IET (Zion Geometry) Experiments in Which H_2 Could Burn

Case	Description	ΔP (MPa)	f_{dome}	Hydrogen-Data (moles)		
				$N_{f,H2}$	$N_{H2,burn}$	$N_{H2,prod}$
I6c1414	No NAD, 100% co-dispersed water	0.225	0.141	195	201	214
I6c1415	No NAD, particle d = 0.125mm (1 field)	0.185	0.133	193	150	162
I6c1416	No NAD, 100% water, mmd = 0.5mm	0.258	0.158	199	231	249
I6c1417	100% water, NAD d_t = 0.0175m	0.306	0.134	165	289	273
I6c1418	100% water, NAD d_t = 0.02m	0.298	0.135	170	274	262
	SNL/IET-7 Experimental Results	**0.271**	**0.074**	**234**	**323**	**274**
I7c1407	Standard input prescription	0.244	0.057	243	296	255
I7c1408	Timestep reduced x 2	0.244	0.057	243	296	256
I7c1409	NAD in cavity only	0.206	0.057	252	248	216
I7c1410	No NAD	0.137	0.059	262	147	126
I7c1412	s_d = 5 in subcompartment	0.255	0.021	240	301	258
I7c1413	'srtemp' = 600 in Dome (cells 13,14)	0.393	0.057	27	506	250
17c1414	No NAD, 100% co-dispersed water	0.212	0.073	273	204	194
I7c1415	NAD d_t = 0.02m, 100% water	0.281	0.070	240	301	257

Table D-5
Results for the Analysis of the ANL/IET-IRR, ANL/IET-3, and ANL/IET-6 Experiments

Case	Description	ΔP (MPa)	f_{dome}	Hydrogen Data (moles)		
				$N_{f,H2}$	$N_{H2,burn}$	$N_{H2,prod}$
	ANL/IET-RR Experimental Results	**0.150**	**0.184**	**4.00**	**~0**	**4.00**
A1C1402	Standard input prescription	0.101	0.079	6.01	0.002	6.01
A1c1403	NAD in cavity only	0.083	0.077	4.92	0.001	4.92
A1c1404	No NAD	0.068	0.078	2.54	0.001	2.54
A1c1405	s_d = 5 in subcompartment	0.099	0.030	6.27	0.001	6.27
	ANL/IET-3 Experimental Results	**0.190**	**0.060**	**1.15**	**3.50**	**4.65**
A3c1402	Standard input prescription	0.229	0.050	0.65	4.75	5.40
A3c1403	NAD in cavity only	0.178	0.050	1.32	3.09	4.41
A3c1404	No NAD	0.124	0.053	0.43	1.97	2.39
A3c1405	s_d = 5 in subcompartment	0.230	0.018	0.59	4.92	5.51
	ANL/IET-6 Experimental Results	**0.250**	**0.138**	**2.95**	**4.22**	**4.89**
A6c1402	Standard input prescription	0.260	0.067	3.16	4.58	5.43
A6c1403	NAD in cavity only	0.197	0.066	3.32	3.33	4.34
A6c1404	No NAD	0.138	0.069	2.62	1.93	2.23
A6c1405	s_d = 5 in subcompartment	0.261	0.022	3.11	4.81	5.60
A6c1406	'srtemp' = 600K	0.321	0.066	0.92	6.78	5.38

Table D-6
Results for Analysis of the SNL/IET-9 Experiment

Case	Description	ΔP (MPa)	f_{dome}	Hydrogen Data (moles)		
				$N_{f,H2}$	$N_{H2,burn}$	$N_{H2,prod}$
	SNL/IET-9 Experimental Results	**0.283**	**0.21**	**413**	**847**	**968**
I9c812	Standard input prescription	0.292	0.121	437	1093	1270
I9c813	s_d = 5 in subcompartment	0.289	0.068	370	1133	1242
I9c814	NAD in cavity only	0.265	0.122	451	977	1167
I9c815	No NAD	0.252	0.131	373	940	1053
I9c818	GFT trapping in dome	0.294	0.119	438	1097	1274
I9c820	Auto 'fromcell' in dome*	0.289	0.124	434	1089	1262
I9c821	'srtemp' = 2000K in dome	0.279	0.122	505	1026	1270
I9c822	As I9c812 with IET-11 atmosphere	0.321	0.123	368	1289	1208
I9c823	As I9c812 w IET-11 atm & 'srtemp' = 759k	0.390	0.122	6	1650	1207
19c824	Default DFB concentrations	0.210	0.169	1010	511	1260
I9c1201	12-cell standard input prescription	0.307	0.123	180	1273	1193
I9c1202	12-cell, 'srtemp' = 2000K in dome	0.297	0.123	238	1214	1192

*Most IET-9 and IET-10 cases were inadvertently run with automatic 'fromcell' specification defeated in the dome and with L_1 in the annulus set to twice the standard value. Effects of both are minor; see introductory discussion in this Appendix.

Table D-7
Results for the Analysis of the SNL/IET-10 Experiment

Case	Description	ΔP (MPa)	f_{dome}	Hydrogen Data (moles)		
				$N_{f,H2}$	$N_{H2,burn}$	$N_{H2,prod}$
	SNL/IET-10 Experimental Results	**0.326**	**0.132**	**186**	**1352**	**1227**
I10c812	Standard input prescription	0.345	0.089	30	1637	1370
I10c813	s_d = 5 in subcompartment	0.342	0.023	27	1668	1398
I10c814	NAD in cavity only	0.319	0.089	39	1535	1277
I10c815	No NAD	0.258	0.107	283	998	983
I10c816	10% bypass to dome	0.354	0.168	31	1624	1357
I10c817	No NAD, 10% bypass to dome	0.273	0.184	284	989	976
I10c818	GFT trapping in dome	0.347	0.086	30	1640	1373
I10c819	No NAD, 10% bypass, GFT trap dome	0.284	0.176	281	1011	995
I10c820	Auto 'fromcell' in dome*	0.345	0.089	30	1637	1370
I10c821	No NAD, 'srtemp' = 780K in dome	0.291	0.106	19	1316	1037
I10c822	No airborne debris, NAD d_p = 0.002m	0.431	0	145	2271	2119
I10c823	100% dispersal from cavity	0.356	0.089	19	1784	1506
I10c824	Particle mmd = 0.5mm	0.361	0.090	34	1790	1527
I10c825	IET-9 containment atmosphere	0.304	0.089	399	1142	1280
I10c827	No Cr in melt	0.306	0.089	19	1411	1133
I10c828	'srtemp' = 2000K in dome	0.314	0.089	241	1384	1328
I10c829	Error in L_1 corrected	0.344	0.083	30	1623	1355
I10c830	No NAD, 100% dispersal from cavity	0.318	0.103	23	1634	1359
I10c831	NAD in cavity only, 100% dispersal	0.322	0.090	20	1671	1394
I10c832	Default DFB concentrations	0.290	0.095	505	1106	1314
I10c1201	12-cell standard input prescription	0.380	0.086	21	1636	1359
I10c1202	12-cell, 'srtemp' = 2000K in dome	0.345	0.086	206	1405	1314

*Most IET-9 and IET-10 cases were inadvertently run with automatic 'fromcell' specification defeated in the dome and with L_1 in the annulus set to twice the standard value. Effects of both are minor; see introductory discussion in this Appendix.

Table D-8
Results for the Analysis of the SNL/IET-11 Eperiment

Case	Description	ΔP (MPa)	f_{dome}	Hydrogen Data (moles)		
				$N_{f,H2}$	$N_{H2,burn}$	$N_{H2,prod}$
	SNL/IET-11 Experimental Results	**0.430**	**0.307**	**137**	**1828**	**1517**
I11c801	Standard input prescription	0.437	0.262	9	1902	1462
I11c802	'srtemp' = 2000K in dome	0.372	0.263	373	1540	1464
I11c803	No NAD	0.336	0.270	364	1245	1161
I11c804	No Insulation	0.354	0.199	374	1356	1280
I11c805	No Insulation and no NAD	0.314	0.207	361	1066	978
I11c806	s_d = 5 in subcompartment	0.433	0.219	8	1926	1485
I11c807	GFT trapping in dome	0.451	0.250	8	1967	1527
I11c808	no structures (adiabatic)	0.693	0.272	4	1942	1497
I11c809	'srtemp' reduced 100K, all cells	0.437	0.261	5	1908	1465
I11c810	No insulation, dome 'srtemp' = 795K	0.425	0.198	10	1718	1279
I11c811	As I11c809 with 'srrate' = $10/V_{cell}^{1/3}$	0.444	0.260	5	1912	1468
I11c812	'srrate' = $10/V_{cell}^{1/3}$	0.448	0.262	8	1903	1463
I11c813	Containment atmosphere as in IET-10	0.387	0.260	28	1809	1543
I11c814	Containment atmosphere as in IET-9	0.333	0.257	503	1258	1500
I11c815	NAD in cavity only	0.348	0.265	373	1431	1355
I11c816	Blowdown corrected	0.434	0.261	5	1896	1453
I11c817	Blowdown corrected, dome 'srtemp' = 2000K	0.366	0.261	375	1528	1454
I11c818	Blowdown corrected, default 'srtemp'	0.433	0.259	3	1900	1454
I11c819	'trapmul' = 10^{-10} (no trapping)	0.567	0.635	13	2772	2336
I11c820	no trapping, no struc, 'srtemp' = 300K except dome	0.918	0.714	5	2774	2330
I11c821	Default DFB concentrations	0.449	0.260	9	1887	1447
I11c1201	12-cell, standard input	0.483	0.259	10	1883	1444

Table D-8 (Continued)
Results for the Analysis of the SNL/IET-11 Eperiment

Case	Description	ΔP (MPa)	f_{dome}	Hydrogen Data (moles)		
				$N_{f,H2}$	$N_{H2,burn}$	$N_{H2,prod}$
I11c1202	'srtemp' = 2000K in dome	0.430	0.260	334	1558	1444
I11c1203	Default 'srtemp'	0.483	0.258	8	1885	1445
I11c1204	Corrected blowdown	0.477	0.255	6	1862	1419
I11c1205	Corrected blowdown, dome 'srtemp' = 2000K	0.424	0.256	323	1544	1418
I11c1206	Corrected blowdown, default 'srtemp'	0.477	0.255	4	1864	1419

All IET-11 cases were run with annulus L_1 set to twice the correct value, and the blowdown was slightly too rapid except in cases marked "Blowdown corrected"; see introductory discussion in this appendix.